ALMA MATER STUDIORUM
UNIVERSITÀ DI BOLOGNA

DOTTORATO DI RICERCA IN

IL FUTURO DELLA TERRA, CAMBIAMENTI CLIMATICI E SFIDE SOCIALI

Ciclo XXXVI

Settore Concorsuale: 04/A4 - GEOFISICA

Settore Scientifico Disciplinare: GEO/10 - GEOFISICA DELLA TERRA SOLIDA

REGIONAL GLACIAL ISOSTATIC ADJUSTMENT MODELING: INTEGRATION OF GEODETIC, GEOPHYSICAL AND GEOLOGICAL DATA

Presentata da: FERNANDO LINSALATA

Coordinatore Dottorato
Prof. SILVANA DI SABATINO

Supervisore
Prof. GIORGIO SPADA

Esame finale anno 2024

I would like to dedicate this thesis to Angela, my parents and my loving dog Margot . . .

Declaration

I declare that this thesis represents my own work except where specific reference is made to the work of others. The contents of this dissertation are original and have not been submitted in whole or in part for consideration for any other degree or qualification in this, or any other university. This dissertation is my own work and contains nothing which is the outcome of work done in collaboration with others, except as specified in the text and Acknowledgements.

Abstract

The Earth is always on the move, constantly. In the last millions of years the Earth's climate has followed a cycle of alternating glacial and interglacial conditions, with a periodicity of the order of 100 kyr. During a glacial period, the lower temperatures cause ice sheets to grow, water is removed from the oceans, and sea levels fall accordingly. Conversely, during interglacial conditions several of these ice sheets have melted, water is returned to the oceans and relative sea-level rises. The most recent cycle began approximately 110 kyr ago and reached the Last Glacial Maximum (LGM) at approximately 20-26 kyr before present (BP). During this period about 5.5 % of the surface water was bound in ice, compared to 1.7 % today. As a result, the average sea-level was about 125-130 m lower than at present and large regions, now covered by shallow seas, were dry land in places forming bridges between previously isolated

islands. As mentioned, the waxing and waning of the major ice sheets during a glacial cycle has a major impact on the global mean (eustatic) sea-level as this movement of water over the surface of the Earth (both as water and as ice) acts as a load upon the lithosphere. Though the ice melted long ago, the land once under and around the ice is still rising and falling in reaction to ice burden. This ongoing movement of land is called Glacial Isostatic Adjustment (GIA) and represents the response of the solid Earth to mass redistribution during a glacial cycle, that is describes the viscoelastic response of the solid Earth to time-dependent changes in ice and ocean loading over the course of a glacial-interglacial cycle. In the first part of this work the impact of the GIA process in the Mediterranean basin will be analyzed, with particular attention to the Venice Lagoon, where the sea-level variations could be catastrophic if we consider the current effect of climate changes. The results indicate that, while GIA represents a relatively small component among those responsible for present-day land movements and relative sea-level variations in the northern Adriatic Sea, its contribution needs to be considered for a correct interpretation of the observed geodetic variations. The second piece of work is on the study of the strength of the lithosphere be-

neath Graham Land region (Antarctic Peninsula) using numerical modeling which simulate lithospheric deformation as a function of geological and geophysical parameters. The results demonstrate that both “jelly sandwich” and the “crème brûlée” model, described in the literature, are valid for the Graham Land lithosphere. Although these two works might seem disconnected, the study of the rheology and strength of the lithosphere play an important role in GIA modeling. Indeed, increasingly advanced knowledge of the crustal and upper mantle rheological structure will lead to better understanding the geological processes but also to better constrain geophysical processes such as that of the GIA Furthermore, the past, present and future variations of the Antarctic ice mass are closely linked to the variations in sea level in the Mediterranean basin, as demonstrated by countless articles previously published in the literature and in the context of present and future climate change induced by anthropogenic emissions of greenhouse gases, it is important to understand correctly how the past climate responded to various forcings in order to correctly capture the potential physical and societal impacts brought by current climate change especially in those areas highly at risk.

(Number of words: 569)

Acknowledgements

First of all, I would like to thank my supervisor, Prof. Giorgio Spada, for his support and thoughtful mentoring throughout my project, for his critical advice in doing research, patience on correcting the write up of thesis and being supportive in this three years of my PhD study. It is really an honor to learn from him professional knowledge. Also, a special thanks to Dr. Daniele Melini from INGV (Istituto Nazionale Geofisica e Vulcanologia) by Rome with whom we have often collaborated during this period. Thanks for your valuable comments and suggestions for the papers, as well as for the funding I received in support of my project. I would also like to thank the very hard-working people of the Geoazur - Université Côte d'Azur, especially Prof. Anthony Mémin for hosting me in his laboratories for three months. Always available and very friendly. I'd like to thank my family who gave me the motivation and support to study the PhD program and last but not least, I'd like to thank Angela, my life partner for always believing in me and for always being by my side. Your love and constant support have helped me so much with finishing this project. I dedicate this doctoral thesis to you.

Contents

1 INTRODUCTION 3

1.1 Glacial Isostatic Adjustment (GIA) 3

1.2 Overview of GIA fingerprints 7

1.3 Sea Level variations 8

1.4 GIA-induced effects on sea level 11

1.5 General scenario with focus on Flandrian transgression 13

1.6 A few words about Milankovitch theory 18

1.7 Mediterranean Region 20

Bibliography 27

2 HOW DOES GIA WORK? 41

2.1 Earth, a deforming body 42

2.1.1 The Earth's Rheology behavior 42

2.1.2 The solid Earth's structure 45

2.1.3 Viscoelasticity and the Maxwell Body 46

2.2 The theory behind GIA 48

2.2.1 Surface load 49

2.2.2 The Sea Level Equation 52

2.3 Numerical modeling of GIA deformation 61

2.3.1 SELEN^4, a program for solving the sea-level equation . 61

2.3.2 Some words about Tegmark grid 64

2.3.3 TABOO, a posT glAcial rebOund simuletOr 65

Bibliography **67**

3 ONGOING SEA-LEVEL RISE AND VERTICAL LAND MOVEMENTS IN THE VENETIAN LAGOON: THE CONTRIBUTION OF GLACIAL ISOSTATIC ADJUSTMENT FROM THE ALPINE ICE SHEET **75**

3.1 Introduction 76

3.2 Sea-level change and vertical land motion in the northern Adriatic 79

3.2.1 Tide gauge and altimetry observations 79

3.2.2 GNSS observations 85

3.3 Glacial Isostatic Adjustment 88

3.3.1 GIA in response to the melting of far field ice sheets . . 95

3.3.2 Regional viscoelastic rebound modeling in the Alps . . . 98

3.4 Results 99

3.4.1 Sea-level change 102

3.4.2 Vertical land motion 106

3.4.3 Absolute sea-level 108

3.5 Discussion 109

3.6 Conclusions 111

Bibliography **115**

4 STRENGTH OF THE LITHOSPHERE DERIVED BY GEOLOGICAL AND GEOPHYSICS DATA: THE GRAHAM LAND (ANTARCTIC PENINSULA) CASE STUDY **129**

4.1 Introduction 132

4.2 Beckground 134

4.2.1 Strain rate 134

4.3 Theory behind the strength of the lithosphere 137

4.3.1 Physical formulation of the strain rate 137

4.3.2 Numerical model of the strength of the lithosphere . . . 139

4.4 Materials and methods 142

4.4.1 GPS data and processing 142

4.4.2 Model parameters 147

4.5 Results 155

4.5.1 Vertical velocity 155

4.5.2 Horizontal velocity 156

4.5.3 Strain rate field 158

4.5.4 The yield strength envelop 161

4.6 Conclusion 164

Bibliography **169**

5 FINAL REMARKS AND FUTURE PERSPECTIVES **189**

A YSE - YIELD STRENGTH ENVELOPE code **193**

B Publications related to this thesis **197**

B.1 Regular Papers 197

B.2 Presentations in National/International Conferences 197

List of Figures **201**

List of Tables **205**

List of acronyms

GIA	Glacial Isostatic Adjustment
kyr	Thousand years
Myr	Millions of years
LGM	Last Glacial Maximum
BP	Before Present
P	Number of the pixels on the grid
R_{res}	Resolution parameter
a	Earth's radius (6371 km)
A^c	Call area
ι	Angular half-amplitude of a disk, in degree
r_{cell}	Value for the radius of the disk
σ	Stress
η	Viscosity
E	Young's modulus
$\dot{\sigma}$	Time derivative of the stress
$\dot{\varepsilon}$	Time derivative of the strain

t	Time
$M(t)$	Mass distributed over the whole Earth's surface
$L(\gamma, t)$	Surface load
γ	(θ, λ)
θ	co-latitude
λ	longitude
$\int_e$	Integration over Earth's surface
dA	Area element
I	Ice thickness
ρ^i	density of ice
ρ^ω	density of water
O	Ocean Function
CF	Continental Function
$B(\gamma, t) = -T$	Sea-level
T	Topography
SLE	Sea Level Eqution
$\mathcal{L}$	Surface load variation
$\mathcal{L}^a$	Change in ice thickness
$\mathcal{L}^b$	Sea-level change
$\mathcal{L}^c$	change in ocean function
r^{ss}	Radii of the (equipotential) sea surface
r^{se}	Radii of the solid Earth
$N(\gamma, t)$	Sea surface variation

$U(\gamma, t)$	Vertical displacement of the Earth's surface
$S(\gamma, t) = N - U$	SLE in its simplest form
S	Elevation variation, measured by the tide gauges
N	Elevation variation of the sea surface
U	Topographic vertical displacement
G	Variation of the geoid radius
Φ	Variation of the total gravity potential of the Earth system
g	Gravity acceleration
c	'c-constant' by Farrell and Clark
$R(\gamma, t)$	Sea-level response function
$SRFs$	Surface response functions
$< \ldots >^o$	Average over the ocean surface
S^{equ}	Spatially invariant term
S^{ofu}	Spatially invariant term
A^o	Area of the oceans
$\Gamma^s(\gamma, t)$	Seal-level Green's function
Υ_l^s	Green's functions rotation response
l and m	Degree and order
$R'^{abc}(\gamma, t)$	Response functions in the sea level
$\dot{\varepsilon}_{\theta\theta}$	Component of strain rate
$\dot{\varepsilon}_{\lambda\lambda}$	Component of strain rate
$\dot{\varepsilon}_{\theta\lambda}$	Component of strain rate
R	Earth's radius

u_θ	Velocity along the latitude
u_λ	Velocity along the longitude
$\dot{\varepsilon}_{\mathrm{z}}$	Vertical strain rate (velocity along the z axis)
σ_{east}	Uncertainty along East component (by MIDAS)
σ_{north}	Uncertainty along North component (by MIDAS)
σ_{up}	Uncertainty along Up component (by MIDAS)
$\dot{\varepsilon}_{\mathrm{max}}$	Maximum principal strain
$\dot{\varepsilon}_{\mathrm{min}}$	Minimum principal strain
$\dot{\varepsilon}^{\mathrm{2inv}}$	Second invariant of the strain rate tensor
$\dot{\chi}$	Maximum shear strain-rate
$\tau_s(\mathrm{z})$	Critical value of the shear stress
τ_s^{fric}	Critical value of friction limit
τ_s^{creep}	Critical value of creep limit
τ_s^{plast}	Critical value of plastic limit
ρ_{litho}	Density of the crust (or mantle)
ρ_{water}	Density of the water
z	Depth
λ'	Pore fluid factor
β	Material constants
ξ_z	Material constants
MPa	Mega Pascal
T	Temperature
q	Surface geothermal heat flow (GHF)

K	Kelvin
$\mathrm{Wm}^{-1}\mathrm{K}^{-1}$	Watts to Kelvin meter
Km^{-2}	Kelvin to square meter
k_{c}	Thermal conductivity of the crust
k_{m}	Thermal conductivity of the mantle
z_{c}	Thickness of the crust
T_{s}	Temperature at the surface
T_{c}	Temperature at the base of the crust
H	Radiogenic heat production rate
$\Sigma = \int_{0}^{\mathrm{z}} \tau_s(\mathrm{z})\mathrm{dz}$	Strength of the lithosphere

Chapter 1

INTRODUCTION

1.1 Glacial Isostatic Adjustment (GIA)

Glacial Isostatic Adjustment (GIA) describes the response of the solid Earth, the gravitational field, and the oceans to the growth and decay of the global ice sheets, that is the response of the solid Earth to mass redistribution during a glacial cycle. In other words, GIA is one of the most important phenomena of low frequency geophysics and by studying it, we are able to infer the main characteristics of the Earth's interior, by solving an inverse problem whose known variables are the observed surface displacements, while the unknowns are the Earth's internal structure and the space-temporal ice melting description. During the early Quaternary period, the glacial cycles lasted on average 41 kyr, but some 1 Myr BP the glacial cycles switched to a periodicity of about 100 kyr, which has been the characteristic time scale during the last 500 kyr [1]. Both periods can be linked to variations in the Earth's orbit around the Sun [2, 3] and the GIA response of the Earth [4], although the origin of the cyclicity is still debated, especially the present 100 kyr period [5, 6].

The most recent cycle began approximately 110 kyr ago and reached the Last Glacial Maximum (LGM) at approximately 20-26 kyr before present (BP) (an example is shown in Figure 1.1) [7, 8]. During this period about 5.5% of the surface water was bound in ice, compared to 1.7% today [9]. As a result, the eustatic sea level was about 120-130 m lower than at present [10] and large regions, now covered by shallow seas, were dry land in places forming bridges between previously isolated islands. During a glacial period the lower temperatures result in the growth of ice sheets, therefore water is removed from the oceans and consequently relative sea-level falls. Conversely, during interglacial conditions several of these ice sheets melt, water returns to the oceans and relative sea-level rises. This movement of water over the Earth's surface (both as water and as ice) acts as a load upon the lithosphere, as the growth of ice sheets concentrates mass on the Earth's surface to the glaciated areas.

From a mechanical point of view the interior of the Earth can be divided into the inner and outer core, the mantle and the lithosphere. Whereas the outermost layer, the lithosphere, is elastic, the solid mantle beneath will (over geological timescales) behave as a fluid. The mean density of the lithosphere is lower than the density of the mantle and left undisturbed for a certain period of time, an equilibrium (isostatic equilibrium) will arise in which the depth to the base of the lithosphere will mainly depend on the weight of the lithosphere itself. A locally greater mass such as an ice sheet caps, corresponds to a greater equilibrium depth. For example, a ship that is launched sinks into the ocean until the weight of the water it displaces is equal to its own weight. As the

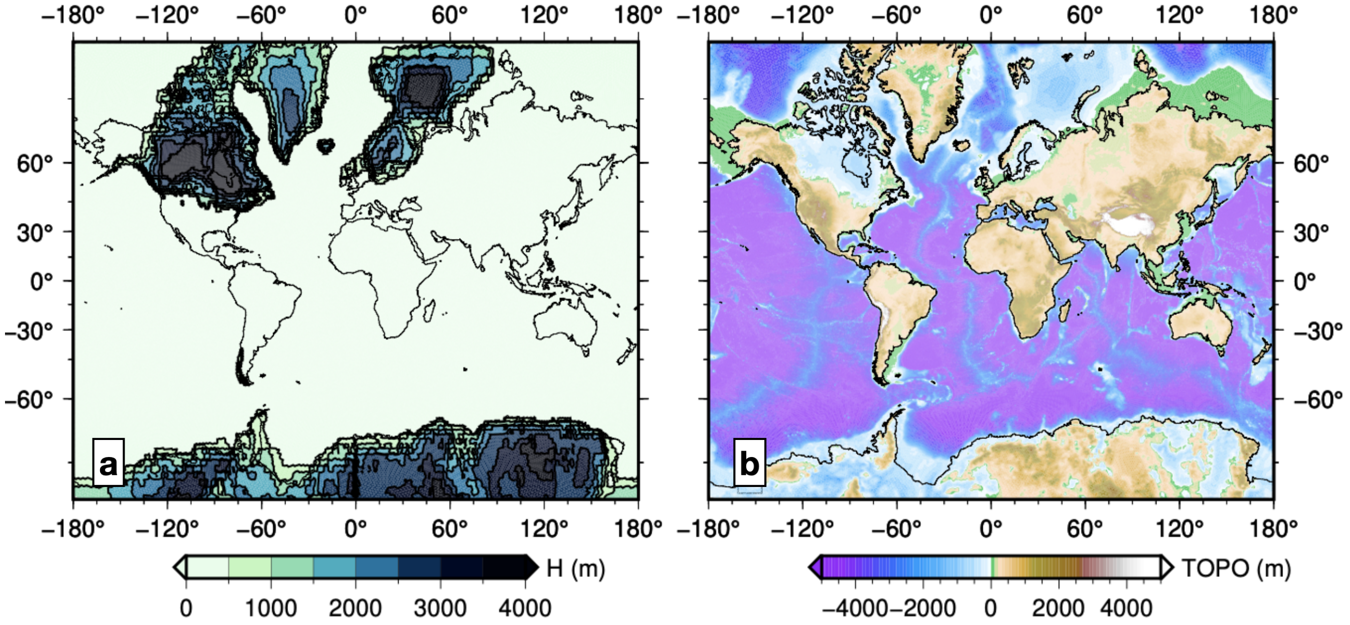

Figure 1.1. Ice thickness and distributions (a) and paleo-topography (b) at LGM according to model ICE-7G NA (VM7).

ship is loaded, it sinks deeper, displacing more water, and so the magnitude of the buoyant force continuously matches the weight of the ship and its cargo. This is known as Archimedes principle stating that, any body completely or partially submerged in a fluid (gas or liquid) at rest is acted upon by an upward, or buoyant, force, the magnitude of which is equal to the weight of the fluid displaced by the body. The volume of displaced fluid is equivalent to the volume of an object fully immersed in a fluid or to that fraction of the volume below the surface for an object partially submerged in a liquid. In the Earth we refer to this as Isostacy or Isostatic equilibrium. During a glacial period, the growth of ice sheets concentrates mass on the Earth's surface to the glaciated areas and acts as a load upon the lithosphere. The weight of the ice depresses the underlying crust, causing mantle rocks below to flow outside the ice margin forming a forebulge just outside the ice sheet (see Figure 1.2). In the meantime, the missing water in the oceans causes the sea level to fall and the pre-deformed sea floor to rise. At the end of the glacial period, during deglaciation, the pressure in the mantle is reduced and material will flow back into the region causing the surface to uplift and mantle rocks below flow back (see Figure 1.2). However uplift of the previously depressed regions will be slow and continue long after the ice has gone. The entire process of subsidence during glacial growth, followed by uplift during and after deglaciation, is referred to as Glacial Isostatic Adjustment and, although deglaciation after the Last Glacial Maximum (LGM) caused a considerable isostatic rebound of orogens world-wide, the current effect of this uplift is still discussion.

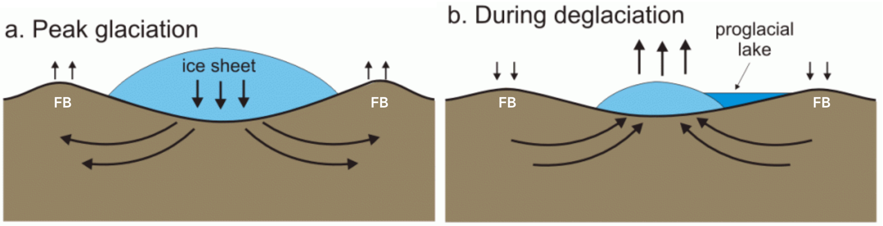

Figure 1.2. Solid Earth subsidence (a) and rebound due to ice unloading (b). From `https://www.antarcticglaciers.org/glaciers-and-climate/sea-level-rise-2/recovering-from-an-ice-age/`

1.2 Overview of GIA fingerprints

Within the GIA framework, it is helpful here to provide a brief overview of the "signals" directly linked to the GIA. In particular they are:

- GIA-signal $\dot{S}$ (Figure1.3a): assuming that GIA from the melting of past ice sheets is the unique cause of contemporary sea-level change, the rates shown in Figure 1.3 would be directly observable as constant secular trends at tide gauges [11, 12].

- GIA-signal $\dot{U}$ (Figure 1.3b): represents the present-day rate of change of the vertical displacement that would be observed, at a given location, by an earthbound GPS receiver [12–16].

- GIA-signal $\dot{N}$ (Figure 1.3c): represents the present-day rate of change of the sea surface height, or absolute sea level that would be observed across the oceans by satellite altimetry assuming that only GIA is contributing to contemporary sea-level change [11, 12, 17].
- GIA-signal $\dot{G}$ (Figure 1.3d): represents the present-day rate of change of the geoid height [12].
- GIA-signal $\dot{L}$ (Figure 1.3e): represents the present-day rate of change of the surface load [12].

1.3 Sea Level variations

Sea level varies constantly, oscillating with well-defined frequencies, as occurs in tidal cycles, or in a more unpredictable way, due to variations in atmospheric pressure and the effect of wave motion. Even if these details are neglected, however, the sea level cannot be considered stable and in the different geological eras, it has undergone lowering and rising of tens and even hundreds of meters, submerging and exposing large portions of the continental shelves. Suess (1888) [18] defined these variations as ‘eustatic’, thinking that they occur equally on all seas, due to their interconnection. In reality it was then discovered that these oscillations are neither equal in intensity nor synchronous in the times of occurrence, although the main variations in sea level are recognizable on all coasts and attributable to the same geological periods. The

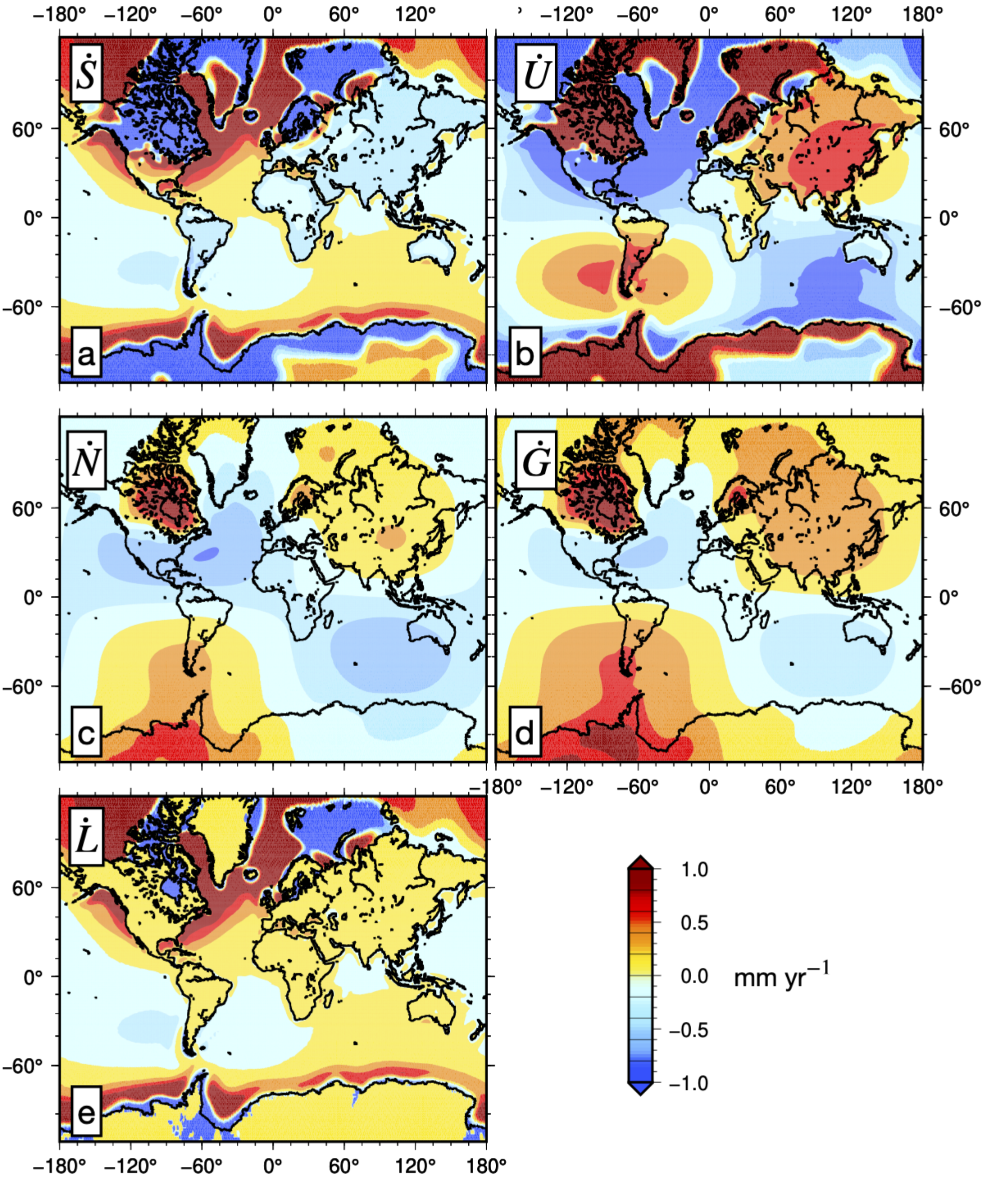

Figure 1.3. GIA fingerprint $\dot{S}$ (a), $\dot{U}$ (b), $\dot{N}$ (c), $\dot{G}$ (d) and $\dot{L}$ (e) obtained by implementing model ICE-7G (VM7) in the SELEN^4 SLE solver.

causes of the variations in sea level that have characterized the most recent periods of the Earth's history are many, but almost all attributable to climatic changes that were particularly intense during the Pleistocene (from 1.6 Myr to 11 kyr ago). In fact, there have been lowering of the sea level in the cold phases and rising in the warm ones, due to the formation or melting of continental ice, and the reduction or increase in the volume of water present in the oceans due to thermal variations. It is known that water undergoes a modest variation in volume as the temperature changes, so much so that a warming of just 1°C of all that present in the oceans would cause their level to rise by only 2 m. During the Pleistocene the average temperature of the oceans varied by no more than 5.1°C therefore, even if the thermal variation had also affected the deeper layers, this phenomenon could be attributed to variations of up to ten metres, a order of magnitude lower than that of the fluctuations that actually occurred. Far more important, in the long term, is the effect determined by the storage of water in continental glaciers during cold periods and by their melting following a subsequent rise in atmospheric temperature. Currently there are about 30 million km^3 of water stored by continental ice [19], while during the last glacial phase there must have been at least twice as much [20]. This is in good agreement with the further rise of about 78 m calculated by [21] for an eventual melting of all the glaciers present on Earth today, a phenomenon not however contemplated by short- and medium-term climate models. The salinity of sea water and atmospheric pressure also affect the volume of the oceans, but both of these parameters have undergone modest variations with the alternation of the glacial periods and their contribution to eustatism is considered irrelevant. Quite different, although difficult to quantify, may be the role of tectonic movements which, by modifying the width of the oceanic basins, can determine positive or negative eustatic variations. Indeed, during the Pleistocene there were phenomena of subsidence on the seabed of the Pacific Ocean which could have interfered with the much more important oscillations due to the climatic variations that occurred precisely in this period. A rise in the sea level can also be caused by the deposition on the seabed of materials produced by the erosion of the emerged lands, a non-negligible phenomenon if one considers that the average rate of denudation of the continental areas is about 4.3 mm s^{-1}, with a production of about 17200 million tons of material per year [22], even if to be distributed over a marine surface almost three times larger than that of the continents. However, not all the volume deposited translates into an eustatic rise, given that the ocean floor undergoes an isostatic lowering due to the pressure exerted by the new materials [23].

1.4 GIA-induced effects on sea level

The GIA-induced sea-level change has certain characteristics. In the glaciated areas, once covered by ice sheets, postglacial sea-level relative to present-day sea level falls during and after deglaciation due to rebounding of Earth's surface which has a larger effect on sea-level than the addition of meltwater.

In the margin of ancient ice sheets, the sea-level change becomes a bit more complicated because the rebound of the ground, the migration and collapse of the forebulge all come into play. The sea level in this area falls initially when the effects of rebound and collapse of gravitational attraction are dominant, followed by an increase when the contribution of the migration of forebulge and the addition of meltwater to ocean becomes dominant [24]. We refer to this as 'near-field'. The near-field consists of sites that were covered by ice sheets at the LGM, and regions within a few hundred kilometres of the former ice margins. As soon as such locations become ice-free they will have relative sea- level fall because the rebound of the solid Earth will be faster than any sea-level rise due to ongoing melting [25, 26].

On the contrary, we refer to the far-field as locations far from the major LGM ice sheets, where relative sea-level change is dominated by the eustatic signal, and GIA-related solid Earth deformation is minimal. The two main processes that contribute to far-field relative sea-level change during periods when there is no change to global ice or water volumes are 'ocean syphoning' and 'continental levering' [24].

In the following image (Figure 1.4), we can see two examples, one referring to $\dot{S}$ (Figure 1.4a) and one referring to $\dot{U}$ (Figure 1.4b) for the entire European area. If we consider only the effect of the remote ice cap (far-field), we observe that, for $\dot{S}$ (Figure 1.4a) it generates a lowering of the sea level with negative values in all the previously frozen areas (in this case Fennoscandia), while $\dot{U}$ (Figure

1.4b) generates a positive vertical movement (uplift). On the contrary, if we refer to the far-field we can observe how the melting of the Fennoscandian ice cap (but also the Laurentide and Antarctica ice caps) has an effect on the entire Mediterranean basin. In particular, it provides for a sea-level rise with peak values especially in the center of the basin. As regards the vertical movement $\dot{U}$ (Figure 1.4b) induced by the melting of remote ice caps, subsidence values are observed in the Mediterranean basin. A detailed explanation and results on the Mediterranean basin and in particular in the Venice Lagoon will be provided in the following chapters.

1.5 General scenario with focus on Flandrian transgression

The Quaternary is the last Period of the Cenozoic Era, in which we are still living. It began about 1.8 Myr BP with the epoch called Pleistocene and continues with the Holocene. In the last 1.8 Myr there have been at least five major glaciations, in particular, Donau, Gunz, Mindel, Riss and Würm, during which the formation of very large quantities of ice stole water from the oceans, causing the lowering of the sea and leaving vast continental areas emerged. During the last Würmian glaciation about 35 million km^3 of ocean water was locked up in ice sheets [29]. Consequently the world ocean level was 125-130 m below the present level. The melting of the ice and the thermal expansion of the water caused the rising of the ocean level and the invasion

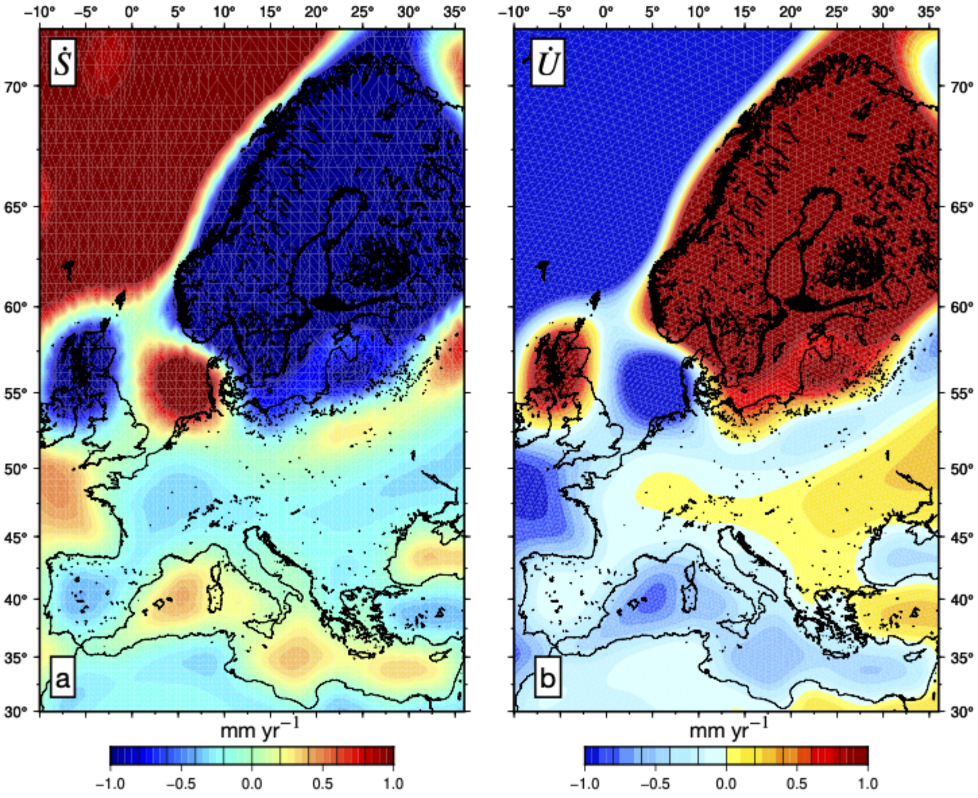

Figure 1.4. Predicted rate of present-day sea-level change $\dot{S}$ (a) and vertical displacement $\dot{U}$ (b) induced by GIA across the Euro-Mediterranean region, according to model ICE-7G NA (VM7) [27, 28]. Numerical results have been obtained using the SELEN^4 SLE solver.

by the sea of large marginal strips of the continents, defined by Jerry Dobson as “aquaterra” [30], has been named Flandrian Transgression. The term was originally coined in Europe, having been first studied in detail on the basis of the coastal deposits of Flanders, while in the United States it has the generic name of the Holocene transgression. In Italy, in reference to the stratigraphy of marine and continental deposits studied for the first time by Blanc et al. (1934) [31] in northern Tuscany, it takes the name of Versilian transgression. Lately this term has been applied to the entire late postglacial transgression.

The Würmian glaciation (Figure 1.5) is the best known in all its aspects, not only because it is the closest to our times, but also because its traces have not been disturbed by other glacial periods. Furthermore, the Würm represents the only well-known glacial event for the Apennine Italy where, an environmental situation very different from that of central and northern Europe occurred: in fact, in the Apennines there were numerous glaciers distributed in a patchy pattern [34]. As mentioned, coinciding with the acme of the last phase of the Würmian glaciation, between 22 *kyr* BP and 18 kyr BP, the sea-level had reached its lowest level: 125-130 m below the current level and large parts of the continental shelf had emerged and been shaped by exogenous agents. Many islands were connected to continents, such as the British Isles to Europe, while New Guinea and Tasmania formed a single continent with Australia; the Bering Strait did not exist and it was possible to walk from Asia to North America, and it is to this fact that we owe the beginning of the human colonization of the American continent about 25 kyr BP years

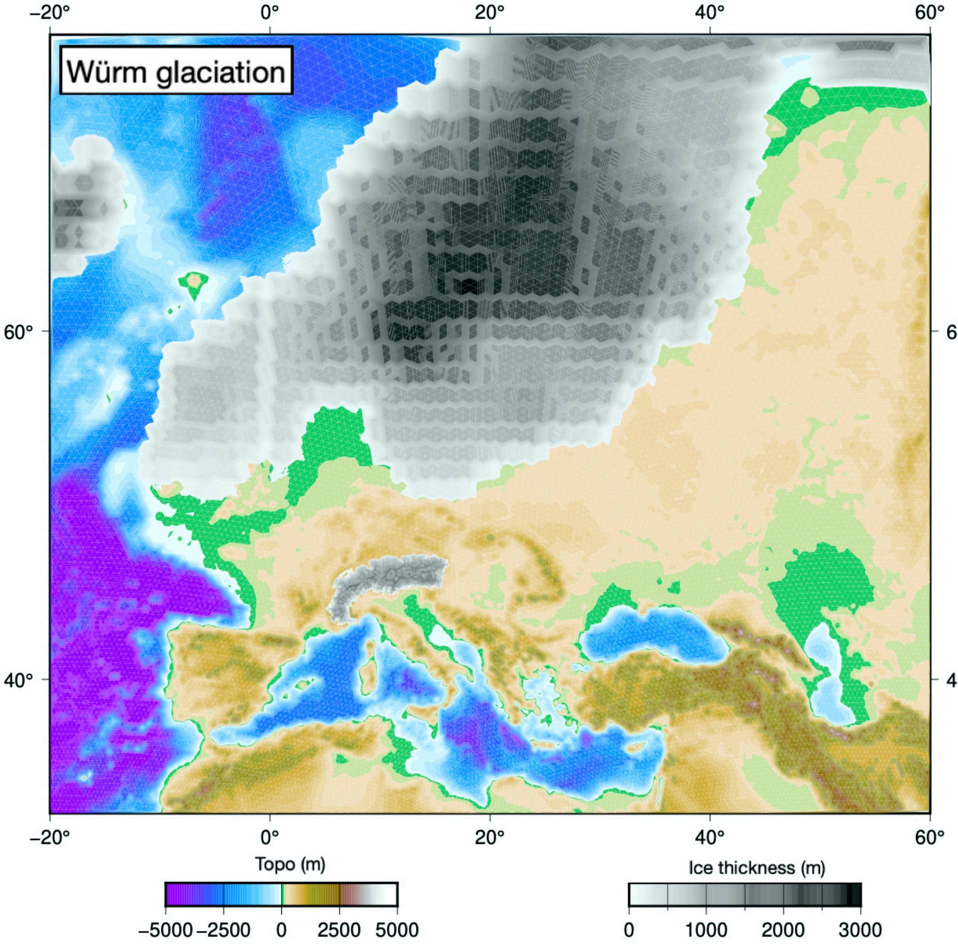

Figure 1.5. General framework of the Mediterranean area during the Würm period resulting from the combination of the ICE-7G models [32] and the Seguinot ice model [33].

ago. The Italian peninsula was wider and incorporated the Island of Elba; the Adriatic Sea was much less extensive, with a shoreline linking today's Ancona and Zara (Dalmatian coast, Croatia); Corsica and Sardinia were united, while Sicily had a large exstention (the Adventure Plateau) which almost reached Tunisia.

Among the first curves plotted to represent sea level rise in the Holocene, those produced by Fairbridge (1961) [35], Shepard (1963b) [36] and Mörner (1969) [37] are of particular interest because they represent the main models on which the scientific community has faced for years: a constant rise (Shepard), a rise with modest fluctuations without the current level being significantly exceeded (Mörner), or a rise interrupted by significant inversions and with a level between 5 kyr BP and 6 kyr BP it had exceeded the current one (Fairbridge) by about 2 m (see Figure 1.6). Although these curves differ significantly from each other, the three authors agree that sea-level rise was particularly rapid in the first period and decidedly slower in the last millennia. Among the reversals and stops, of particular interest are those identified by Curray (1960) [38] in the Gulf of Mexico: here there would be traces of a lowering of the sea-level of about thirty meters (approximately between -30 and -60 m) occurred between 12 kyr BP and 11 kyr BP, therefore synchronous with the cold period (Dryas) during which there was a new expansion of the continental ice sheets, and a stationary phase at -18 m centered on 10 kyr BP, which would have favored the formation of marine erosion platforms subsequently identified at the same altitude in other areas as well.

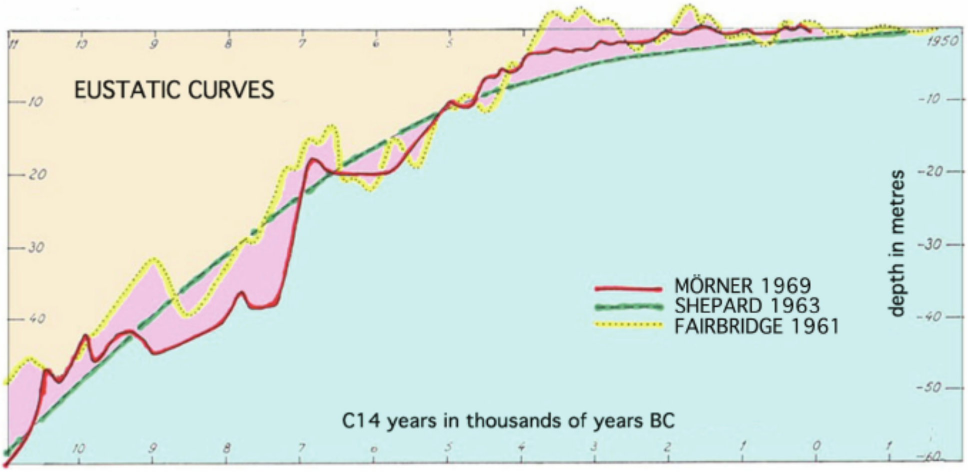

Figure 1.6. The eustatic curves of Fairbridge [35] Shepard [36] and Mörner [37]. The purple field provides the difference between the 3 curves.

1.6 A few words about Milankovitch theory

Among the longest astrophysical and astronomical cycles that might influence climate, only those involving variations in the elements of the Earth's orbit have been found to be significantly related to the long-term climatic data deduced from the geological record [39]. As mentioned, the most important climate modifications that determine sea level variations are connected to the so-called glacial cycles. The Scottish naturalist James Croll [40] was the first to suggest that the climatic fluctuations of the last 2 Myr were the result of the very slow movements that the Earth describes in space and in the rotation around the Sun. The theory was then reworked by Milankovich (1930) [41, 42], a Serbian engineer, mathematician and climatologist who worked at the turn of the First and Second World Wars. Milankovitch, in his "Glacial Theory" hypothesized that it was the variation of solar insolation at the top of the Northern Hemisphere atmosphere that forces the formation and melting of glacial masses [39, 43]. According to Milankovitch's theory, due to the gravitational attraction that the bodies of the solar system exert on our planet, the Earth's orbit is continuously modified by the cycles of the precession of the equinoxes, by the obliquity of the ecliptic and by the eccentricity of the orbit (Figure 1.7) [44]. On the basis of the astronomical laws that describe these variations, and assuming the Earth's atmosphere to be stationary, Milankovitch formulated a mathematical model capable of calculating the variation of solar radiation that has reached the Earth, at different latitudes, in the last 600 kyr BP, thus explaining the alternating in the past of warmer and colder periods. The combination of the three astronomical cycles, affecting the summer insolation of the Boreal Hemisphere, where most of the emerged lands are concentrated, determines the passage from glacial to interglacial phases with periods of about 100 kyr. The Earth is currently experiencing a warm period or interglacial, the Holocene, also known as isotope stage 1 which started about 10.5 kyr BP [39]. This period follows a glacial phase in which, about 22 kyr BP, the sea was more than 125-130 m below present level. The first evidence of the height of glacial and interglacial phases in the sea came from analyzing the relationship between the stable isotopes of oxygen contained in the fossil remains of marine organisms ((δ^{18}O), which describes the relative abundance between the isotopes O^{16} and O^{18}) [45, 46] able to record in its shell the temperature of the waters in the period in which they lived. This is why these climatic phases, roughly corresponding to the Milankovitch cycles, are called isotopic stages, and are indicated with increasing numbers going back in time. Stage 1 corresponds to the Holocene; similarly, the odd numbers indicate the interglacial periods of the past, while the even numbers identify the glacial phases. *Stage 2* (LGM) corresponds to the last glacial period whose coldest peak occurred at 22 kyr BP [44].

1.7 Mediterranean Region

The Mediterranean Basin is a region of special interest in the study of past and present relative sea level evolution. The intense glaciation-deglaciation cycles that dominated climate system variability over the past several hundred thousand years were associated with significant variations of global sea level, not only through the direct impact of these large redistributions of mass between the oceans and the continental cryosphere, but also due to the time-dependent response of the Earth's shape to these varying surface loads (see *e.g.,* [4, 8, 32, 48, 49]).

One may reasonably think of the Mediterranean Basin as providing similarly strategic information concerning post-LGM deglaciation as does the U.S. Atlantic coastal region, in terms of the evolution of the nearby North-western Eurasian ice sheet complex and of the far-field influence of the Laurentide, Greenland and Antarctic ice sheets [32].

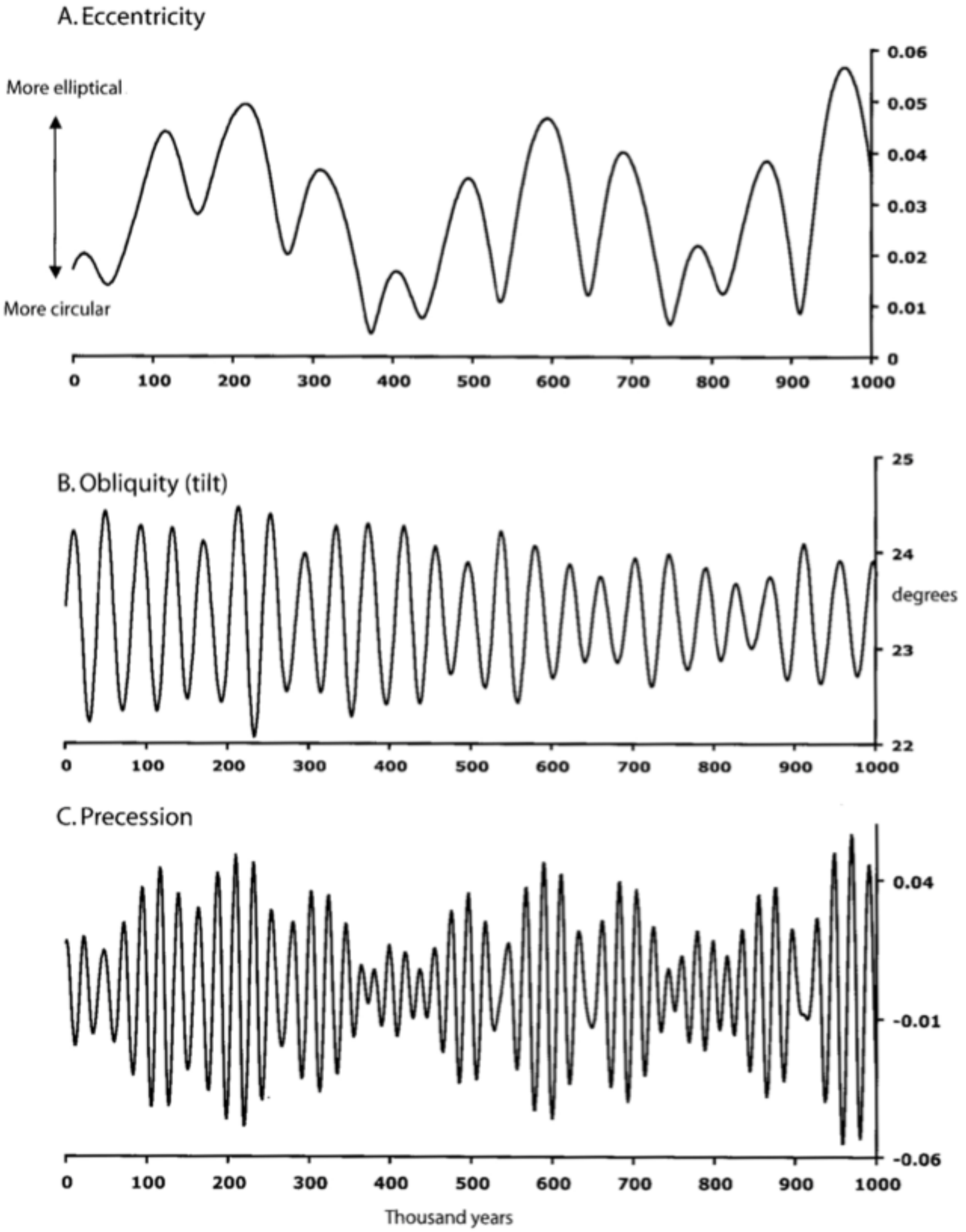

Figure 1.7. Orbital parameter evolution over the last million years, for (A) eccentricity, (B) axial obliquity, and (C) precession (modulated by eccentricity). From Roy (2017) [47].

The microtidal regime and presence of numerous remains of coastal archeological structures have made the intermediate to far-field Mediterranean region a focus for sea-level studies [48, 50, 51]. Regional compilations of Relative Sea Level (RSL) data have been produced for both the eastern [52] and western [53, 54] Mediterranean coast. Significant sea-level data have also been collected as part of coastal investigations with other purposes, for example, studies of Holocene environmental changes in marshes and coastal lagoons in Spain [55, 56], France [57–59], Sardinia and Corsica [57, 60–62], Tunisia [63, 64] as well as along the Adriatic [65, 66] and Tyrrhenian [67, 68] coasts of Italy. Similarly, Correggiari et al. (1996) [69], Lambeck et al., 2004a [48] and other (see *e.g.,* [54, 70]) assessed the postglacial RSL changes along the Italian peninsula and Croatia.

RSL records from tectonically stable sectors of the western Mediterranean document a continuous rise from 49.5 ± 0.8 m at 11.5 ka BP due primarily to glacio and hydro-isostatic factors [71]. In the eastern Mediterranean region, RSL rise slowed significantly in the last 7.5 ka BP, with consequent initiation of deltaic progradations of the largest Mediterranean rivers [72] such as the Nile delta. The Southern Tunisia RSL record is characterized by a well-documented mid-Holocene highstand beginning at 7.5 ka BP [73]. RSL reached a maximum highstand of 1.1 ± 0.2 m at ~ 5.8 ka BP, with RSL falling to present slowly at rate of $\sim 0.19 \pm 0.07$ m/ka from 6.5 ka BP to present. Stocchi and Spada (2007) [74] claim that the observed late–Holocene sharp high–stand in SE Tunisia ($\sim$ 5 kyrs BP) mostly reflects the history of melting of the Antarctic ice sheet, since the two major Northern Hemisphere ice sheets (Laurentide and Fennoscandia) at this time had completely melted and their contributions to relative sea-level have opposite signs and almost cancel. In their article, in fact, they say: : *"The RSL curves expected in this region for the deglaciation model ICE3G are characterized by a developed late–Holocene high–stand, which broadly matches a suite of observations and geological indicators"*. Hypothesis later confirmed also by Mauz et al. (2015) [75], which highlight that the Tunisian highstand is compatible with the melting history of the Antarctic ice sheet.

In this sense, the data from southern Tunisia, collected from the Gulf of Gabes, are of considerable interest for two main reasons: (i) the suggested sensitivity of the predictions of the GIA model in this position to the influence of the Antarctic ice sheet (AIS) off the field [49, 76] and (ii) the suggested existence of a late Holocene tribune in this region of the Mediterranean Sea [49, 71].

Original contributions of this thesis

The original contributions of this thesis are listed below:

1. Up-to-date caused by GIA, high-resolution estimate of sea- level change and vertical deformation at the Mediterranean scale are obtained.
2. It is found that GIA effects are a marginal contribution to geodetic velocity only at sites where the largest subsidence is recorded, while, at

the majority of GNSS sites, GIA may represent a significant contribution to observed rates.

3. At the same time, GIA-driven sea-level change represents a fraction of the observed rates of sea-level ranging from 30% per cent in the Venetian Lagoon to over 50% at Trieste and it significantly mitigates sea-level rise due to present-day climate change.
4. As for the Antarctic Peninsula, data indicates clearly highlights the diffuse state of uplift, in fact, subsidence was recorded only in 5 of the 21 stations analysed.
5. Geodynamics of the Graham Land describe two distinct kinematic patterns, going from being relatively stable with very small (insignificant) deformation to an increasing W-E oriented deformation.
6. The strength of the lithosphere (YSE) can vary drastically, changing from a strong crust and a weak mantle to weak crust and a relatively strong mantle, proving that, both “jelly sandwich” and “crème brûlée” models are valid for the Graham Land region depending on specific thermal and rheological conditions of the area considered.

Organization of this dissertation

Each of the contributions enumerated above are the subject of one chapter in this dissertation. The organization of this document is as follows:

Chapter 1 presents the overview of GIA phenomena that represent the scope of this thesis. It includes the fingerprints related to the GIA, the sea level variation and GIA-induced effects on sea level, the general scenario with focus on Flandrian transgression, and a few words about the Mediterranean region.

Chapter 2 builds on the "working" of the GIA theory: the Earth structure and rheology, the viscoelasticity and the Maxewll body. Then are spent some words about the code uses to compute Earth's movements due to GIA and subsequently approaches the GIA from a theoretical point of view: the surface load and the sea level equations.

Chapter 3 focuses on the modeling and analysis of GIA phenomena in the northern Adriatic region, taking into account the contribution of the Alpine ice sheet during the Last Glacial Maximum through an analysis of both GNSS signals and tidal gauges.

Chapter 4 presents a method, already used in the literature, to calculate the strength of the lithosphere through the analysis of geological and geophysical data such as geothermal heat flux, heat production, strain rate and so on.

Bibliography

[1] EPICA community members, “Eight glacial cycles from an Antarctic ice core”, *Nature*, vol. 429, no. 6992, pp. 623–628, 2004.

[2] André Berger, “Long-term variations of daily insolation and Quaternary climatic changes”, *Journal of Atmospheric Sciences*, vol. 35, no. 12, pp. 2362–2367, 1978.

[3] André Berger and Marie-France Loutre, “Insolation values for the climate of the last 10 million years”, *Quaternary Science Reviews*, vol. 10, no. 4, pp. 297–317, 1991.

[4] Richard W Peltier, “Postglacial variations in the level of the sea: Implications for climate dynamics and solid-earth geophysics”, *Reviews of Geophysics*, vol. 36, no. 4, pp. 603–689, 1998.

[5] André Berger and Marie-France Loutre, “Modeling the 100-kyr glacial–interglacial cycles”, *Global and Planetary Change*, vol. 72, no. 4, pp. 275–281, 2010.

[6] Andrey Ganopolski and Reinhard Calov, "The role of orbital forcing, carbon dioxide and regolith in 100 kyr glacial cycles", *Climate of the Past*, vol. 7, no. 4, pp. 1415–1425, 2011.

[7] Richard W Peltier and Richard G Fairbanks, "Global glacial ice volume and Last Glacial Maximum duration from an extended Barbados sea level record", *Quaternary Science Reviews*, vol. 25, no. 23-24, pp. 3322–3337, 2006.

[8] Richard W Peltier, Donald Argus, and Revel Drummond, "Space geodesy constrains ice age terminal deglaciation: The global ICE-6G_C (VM5a) model", *Journal of Geophysical Research: Solid Earth*, vol. 120, no. 1, pp. 450–487, 2015.

[9] Holger Steffen and Patrick Wu, "Glacial isostatic adjustment in fennoscandia—a review of data and modeling", *Journal of geodynamics*, vol. 52, no. 3-4, pp. 169–204, 2011.

[10] Richard G Fairbanks, "A 17,000-year glacio-eustatic sea level record: influence of glacial melting rates on the younger dryas event and deep-ocean circulation", *Nature*, vol. 342, no. 6250, pp. 637–642, 1989.

[11] Giorgio Spada, "Glacial isostatic adjustment and contemporary sea level rise: An overview", *Surveys in Geophysics*, vol. 38, no. 1, pp. 153–185, 2017.

[12] Giorgio Spada and Daniele Melini, "On some properties of the glacial

isostatic adjustment fingerprints", *Water*, vol. 11, no. 9, pp. 1844, 2019.

[13] Guy Wöppelmann, Martin B Miguez, Marie-Noëlle Bouin, and Zuheir Altamimi, "Geocentric sea-level trend estimates from gps analyses at relevant tide gauges world-wide", *Global and Planetary Change*, vol. 57, no. 3-4, pp. 396–406, 2007.

[14] Guy Wöppelmann and Marta Marcos, "Vertical land motion as a key to understanding sea level change and variability", *Reviews of Geophysics*, vol. 54, no. 1, pp. 64–92, 2016.

[15] Julia Pfeffer and Pascal Allemand, "The key role of vertical land motions in coastal sea level variations: A global synthesis of multisatellite altimetry, tide gauge data and gps measurements", *Earth and planetary science letters*, vol. 439, pp. 39–47, 2016.

[16] Julia Pfeffer, Giorgio Spada, Anthony Mémin, Jean-Paul Boy, and Pascal Allemand, "Decoding the origins of vertical land motions observed today at coasts", *Geophysical Journal International*, vol. 210, no. 1, pp. 148–165, 2017.

[17] Anny Cazenave and William Llovel, "Contemporary sea level rise", *Annual review of marine science*, vol. 2, pp. 145–173, 2010.

[18] Eduard Suess, *Das antlitz der erde*, vol. 2, F. Tempsky, 1909.

[19] Mark B Dyurgerov and Mark F Meier, "Mass balance of mountain and subpolar glaciers: a new global assessment for 1961–1990", *Arctic and*

Alpine Research, vol. 29, no. 4, pp. 379–391, 1997.

[20] Paolo A Pirazzoli, “Sea-level changes: the last 20 000 years”, *Oceanographic Literature Review*, vol. 8, no. 44, pp. 785, 1997.

[21] Timothy Moses, George N Kiladis, HF Diaz, and RG Barry, “Characteristics and frequency of reversals in mean sea level pressure in the north atlantic sector and their relationship to long-term temperature trends”, *Journal of Climatology*, vol. 7, no. 1, pp. 13–30, 1987.

[22] Andrew R Gilchrist and MA Summerfield, “Denudation, isostasy and landscape evolution”, *Earth Surface Processes and Landforms*, vol. 16, no. 6, pp. 555–562, 1991.

[23] Enzo Pranzini, “La forma delle coste”, *Geomorfologia costiera impatto antropico e difesa dei litorali*, p. 245, 2004.

[24] Jerry X Mitrovica and Glenn A Milne, “On the origin of late holocene sea-level highstands within equatorial ocean basins”, *Quaternary Science Reviews*, vol. 21, no. 20-22, pp. 2179–2190, 2002.

[25] Pippa Whitehouse, “Glacial isostatic adjustment and sea-level change”, *State of the art report, Svensk Kärnbränslehantering AB, Swedish Nuclear Fuel and Waste Management Co., Stockholm*, p. 105, 2009.

[26] Pingping Huang, “Modelling glacial isostatic adjustment with composite rheology”, *HKU Theses Online (HKUTO)*, 2018.

[27] Keven Roy and Richard W Peltier, “Glacial isostatic adjustment, relative

sea level history and mantle viscosity: reconciling relative sea level model predictions for the US East coast with geological constraints", *Geophysical Journal International*, vol. 201, no. 2, pp. 1156–1181, 2015.

[28] Keven Roy and Richard W Peltier, "Space-geodetic and water level gauge constraints on continental uplift and tilting over North America: regional convergence of the ICE-6G_C (VM5a/VM6) models", *Geophysical Journal International*, vol. 210, no. 2, pp. 1115–1142, 2017.

[29] Pavel A. Kaplin, "Flandrian transgression", *Beaches and Coastal Geology*, pp. 428–429, 1982.

[30] Jerome E Dobson, "Aquaterra incognita: Lost land beneath the sea", *Geographical Review*, vol. 104, no. 2, pp. 123–138, 2014.

[31] Mark Le Blanc and Gregory Wehner, "Beitrag zur kenntnis der manganoxyde", *Zeitschrift für Physikalische Chemie*, vol. 168, no. 1, pp. 59–78, 1934.

[32] Keven Roy and Richard W Peltier, "Relative sea level in the Western Mediterranean basin: A regional test of the ICE-7G_NA (VM7) model and a constraint on late Holocene Antarctic deglaciation", *Quaternary Science Reviews*, vol. 183, pp. 76–87, 2018.

[33] Julien Seguinot, Susan Ivy-Ochs, Guillaume Jouvet, Matthias Huss, Martin Funk, and Frank Preusser, "Modelling last glacial cycle ice dynamics in the Alps", *The Cryosphere*, vol. 12, no. 10, pp. 3265–3285, 2018.

[34] Carlo Baroni, Giulia Guidobaldi, Maria Cristina Salvatore, Marcus Christl, and Susan Ivy-Ochs, “Last glacial maximum glaciers in the northern apennines reflect primarily the influence of southerly storm-tracks in the western mediterranean”, *Quaternary Science Reviews*, vol. 197, pp. 352–367, 2018.

[35] Rhodes W Fairbridge, “Eustatic changes in sea level”, *Physics and Chemistry of the Earth*, vol. 4, pp. 99–185, 1961.

[36] Francis P Shepard, “Thirty-five thousand years of sea-level”, *Essays in marine geology in honor of KO Emery*, pp. 1–10, 1963.

[37] Nils Axel Mörner, *The Late Quaternary history of the Kattegatt Sea and the Swedish West Coast: deglaciation, shorelevel displacement, chronology, isostasy and eustasy*, Ph.D. thesis, Sveriges geologiska undersökning, 1969.

[38] Joseph R Curray, “Sediments and history of holocene transgression, continental shelf, northwest gulf of mexico”, *Sedimentology*, pp. 221–266, 1960.

[39] André Berger, “Milankovitch theory and climate”, *Reviews of geophysics*, vol. 26, no. 4, pp. 624–657, 1988.

[40] James Croll, “Climate and time”, *Nature*, vol. 12, no. 304, pp. 329–329, 1875.

[41] Milutin Milankovitch, “Mathematische klimalehre und astronomische

theorie der klimaschwankungen", *Handbuch der Klimatologie 1*, 1930.

[42] Konigl M Milankovitch, "Kanon der erdbestrahlung und seine anwendung auf das eiszeitenproblem", *Royal Serbian Academy Special Publication*, vol. 133, pp. 1–633, 1941.

[43] Hai Cheng, Hanying Li, Lijuan Sha, Ashish Sinha, Zhengguo Shi, Qiuzhen Yin, Zhengyao Lu, Debo Zhao, Yanjun Cai, Yongyun Hu, et al., "Milankovitch theory and monsoon", *The Innovation*, vol. 3, no. 6, 2022.

[44] Sergio Silenzi, "Le variazioni del livello del mare mediterraneo negli ultimi 3000 anni", 2012.

[45] Nicholas J Shackleton, "Attainment of isotopic equilibrium between ocean water and the benthonic foraminifera genus uvigerina: isotopic changes in the ocean during the last glacial", *Les Methodes Quantitatives D'etude Des Variations Du Climax Au Cours Du Pleistocene*, vol. 219, pp. 203–209, 1974.

[46] Thomas B Kellogg, Jean Claude Duplessy, and Nicholas J Shackleton, "Planktonic foraminiferal and oxygen isotopic stratigraphy and paleoclimatology of norwegian sea deep-sea cores", *Boreas*, vol. 7, no. 1, pp. 61–73, 1978.

[47] Keven Roy, *High-quality constraints on the glacial isostatic adjustment process over North America: The ICE-7G_NA (VM7) model*, Ph.D. thesis, University of Toronto (Canada), 2017.

[48] Kurt Lambeck, Fabrizio Antonioli, Anthony Purcell, and Sergio Silenzi, "Sea-level change along the italian coast for the past 10,000 yr", *Quaternary Science Reviews*, vol. 23, no. 14-15, pp. 1567–1598, 2004.

[49] Paolo Stocchi and Giorgio Spada, "Influence of glacial isostatic adjustment upon current sea level variations in the Mediterranean", *Tectonophysics*, vol. 474, no. 1-2, pp. 56–68, 2009.

[50] Paolo A Pirazzoli, "Sea level variations in the northwest mediterranean during roman times", *Science*, vol. 194, no. 4264, pp. 519–521, 1976.

[51] Nicholas Coit Flemming, *Archaeological evidence for eustatic change of sea level and earth movements in the Western Mediterranean during the last 2000 years*, vol. 109, Geological Society of America, 1969.

[52] Christophe Morhange, Paolo A Pirazzoli, Nick Marriner, Lucien F Montaggioni, and Tanios Nammour, "Late holocene relative sea-level changes in lebanon, eastern mediterranean", *Marine Geology*, vol. 230, no. 1-2, pp. 99–114, 2006.

[53] Kurt Lambeck and Edouard Bard, "Sea-level change along the french mediterranean coast for the past 30 000 years", *Earth and Planetary Science Letters*, vol. 175, no. 3-4, pp. 203–222, 2000.

[54] Fabrizio Antonioli, Luigi Ferranti, Alessandro Fontana, Alessandro Amorosi, Aldino Bondesan, Carla Braitenberg, Andrea Dutton, Giorgio Fontolan, Stefano Furlani, et al., "Holocene relative sea-level changes and

vertical movements along the italian and istrian coastlines", *Quaternary International*, vol. 206, no. 1-2, pp. 102–133, 2009.

[55] Michéle Dupré et al., "Quaternary evolution of the pego coastal lagoon (southern valencia, spain)", *Palaeogeography, Palaeoclimatology, Palaeoecology*, vol. 68, no. 2-4, pp. 291–299, 1988.

[56] Javier Marco-Barba, Jonathan A Holmes, Francesc Mesquita-Joanes, and Maria Rosa Miracle, "The influence of climate and sea-level change on the holocene evolution of a mediterranean coastal lagoon: evidence from ostracod palaeoecology and geochemistry", *Geobios*, vol. 46, no. 5, pp. 409–421, 2013.

[57] Jacques Laborel and Francoise Laborel-Deguen, "Biological indicators of relative sea-level variations and of co-seismic displacements in the mediterranean region", *Journal of coastal research*, pp. 395–415, 1994.

[58] Olivier Raynal et al., "Holocene evolution of a languedocian lagoonal environment controlled by inherited coastal morphology (northern gulf of lions, france)", *Bulletin de la Société Géologique de France*, vol. 181, no. 2, pp. 211–224, 2010.

[59] Pierre Sabatier, Laurent Dezileau, Mickaël Barbier, Olivier Raynal, Johanna Lofi, Louis Briqueu, Michel Condomines, Frédéric Bouchette, Raphaël Certain, Ulrich Van Grafenstein, et al., "Late-holocene evolution of a coastal lagoon in the gulf of lions (south of france)", *Bulletin de la Société géologique de France*, vol. 181, no. 1, pp. 27–36, 2010.

[60] Fabrizio Antonioli, Marco Anzidei, Kurt Lambeck, Rita Auriemma, Dario Gaddi, Stefano Furlani, Paola Orrù, Emanuela Solinas, Andrej Gaspari, Snježana Karinja, et al., "Sea-level change during the holocene in sardinia and in the northeastern adriatic (central mediterranean sea) from archaeological and geomorphological data", *Quaternary Science Reviews*, vol. 26, no. 19-21, pp. 2463–2486, 2007.

[61] Federico Di Rita and Rita Teresa Melis, "The cultural landscape near the ancient city of tharros (central west sardinia): vegetation changes and human impact", *Journal of Archaeological Science*, vol. 40, no. 12, pp. 4271–4282, 2013.

[62] Emanuele P Orru, Giuseppe Mastronuzzi, Giacomo Deiana, Cosimo Pignatelli, Arcangelo Piscitelli, Emanuela Solinas, PG Spanu, and Raimondo Zucca, "Sea level changes and geoarchaeology between the bay of Capo Malfatano and Piscinnì Bay (SW Sardinia) in the last 4 kys.", *Quaternary International*, vol. 336, pp. 180–189, 2014.

[63] Rached Lakhdar, Mohamed Soussi, Mohamed Hédi Ben Ismail, and Ali M'Rabet, "A Mediterranean Holocene restricted coastal lagoon under arid climate: case of the sedimentary record of Sabkha Boujmel (SE Tunisia)", *Palaeogeography, Palaeoclimatology, Palaeoecology*, vol. 241, no. 2, pp. 177–191, 2006.

[64] Chahira Zaîbi, Pierre Carbonel, Fekri Kamoun, Chafai Azri, Amira Kharroubi, Néjib Kallel, Younès Jedoui, Mabrouk Montacer, and Michel

Fontugne, “Évolution du trait de côte à l’holocène supérieur dans la sebkha el-guettiate de skhira (golfe de gabès, tunisie) à travers sa faune d’ostracodes et de foraminifères”, *Geobios*, vol. 44, no. 1, pp. 101–115, 2011.

[65] Charles E McClennen and Rupert A Housley, “Late-holocene channel meander migration and mudflat accumulation rates, lagoon of venice, italy”, *Journal of Coastal Research*, vol. 22, no. 4, pp. 930–945, 2006.

[66] Massimo Caldara and Oronzo Simone, “Coastal changes in the eastern tavoliere plain (apulia, italy) during the late holocene: Natural or anthropic?”, *Quaternary Science Reviews*, vol. 24, no. 18-19, pp. 2137–2145, 2005.

[67] Federico Di Rita, Alessandra Celant, and Donatella Magri, “Holocene environmental instability in the wetland north of the tiber delta (rome, italy): sea-lake-man interactions”, *Journal of Paleolimnology*, vol. 44, pp. 51–67, 2010.

[68] Marco Sacchi, F Molisso, A Pacifico, Marco Vigliotti, Carlo Sabbarese, and Daniela Ruberti, “Late-holocene to recent evolution of lake patria, south italy: An example of a coastal lagoon within a mediterranean delta system”, *Global and Planetary Change*, vol. 117, pp. 9–27, 2014.

[69] Annamaria Correggiari, ME Field, and F Trincardi, “Late quaternary transgressive large dunes on the sediment-starved adriatic shelf”, *Geological Society, London, Special Publications*, vol. 117, no. 1, pp. 155–169,

1996.

[70] Kurt Lambeck, Fabrizio Antonioli, Marco Anzidei, et al., "Sea level change along the italian coast during the holocene and projections for the future", *Quaternary International*, vol. 232, no. 1-2, pp. 250–257, 2011.

[71] Matteo Vacchi, Nick Marriner, Christophe Morhange, Giorgio Spada, Alessandro Fontana, and Alessio Rovere, "Multiproxy assessment of holocene relative sea-level changes in the western mediterranean: Sea-level variability and improvements in the definition of the isostatic signal", *Earth-Science Reviews*, vol. 155, pp. 172–197, 2016.

[72] Edward J Anthony, Nick Marriner, and Christophe Morhange, "Human influence and the changing geomorphology of mediterranean deltas and coasts over the last 6000 years: From progradation to destruction phase?", *Earth-Science Reviews*, vol. 139, pp. 336–361, 2014.

[73] Christophe Morhange and Paolo Antonio Pirazzoli, "Mid-holocene emergence of southern tunisian coasts", *Marine Geology*, vol. 220, no. 1-4, pp. 205–213, 2005.

[74] Paolo Stocchi and Giorgio Spada, "Glacio and hydro-isostasy in the mediterranean sea: Clark's zones and role of remote ice sheets", *Annals of Geophysics*, 2007.

[75] Barbara Mauz, Gabriella Ruggieri, and Giorgio Spada, "Terminal antarc-

tic melting inferred from a far-field coastal site”, *Quaternary Science Reviews*, vol. 116, pp. 122–132, 2015.

[76] Paolo Stocchi, Florence Colleoni, and Giorgio Spada, “Bounds on the time–history and holocene mass budget of antarctica from sea–level records in se tunisia”, *Pure and Applied Geophysics*, vol. 166, pp. 1319–1341, 2009.

Chapter 2

HOW DOES GIA WORK?

This chapter is organised into several sections. Here I introduce the theoretical framework of this Chapter.

In Section 2.1.2, I define the structure of the Earth and in Section 2.1.1 I introduce the Earth's rheology; the entire geodynamic spectrum is also presented. Section 2.1.3 deals with the basic theory of viscoelasticity and the simplest viscoelastic model like a Maxwell body. In Section 2.3.1 I briefly describe SELEN[4], the code used to create most of the figures in this thesis, while in Section 2.3.2 I mention the Tegmark grid and its importance in the ice discretization. Finally, in Section 2.3.3, I spend a few words on the TABOO code.

2.1 Earth, a deforming body

2.1.1 The Earth's Rheology behavior

Rheology, from the Greek verb '$\rho\epsilon\omega$' meaning to flow, is the study of the stream of matter, mainly in the liquid state, but also how solids respond to elastic deformation as a result of an applied force. At one extreme we have the elastic deformations of solid materials, which follow Hooke's law, at the other the Newtonian flow of liquids and gases. Between the two there are the phenomena of flow of substances which show intermediate properties between those of fluids and those of solids. The term rheology was first coined by Eugene Bingham (1878-1945) and gives us the physical basis for understanding geodynamic processes.

In modeling a particular geophysical phenomenon, the choice of the rheology used depends both on the quality of the geophysical data, which the calculations of the model are required to match and our knowledge of the rheological behavior of the medium at hand. Over the last few decades a considerable amount of knowledge has been gained about mantle rheology in terms of the values of rheological parameters and deformation mechanisms [1]. For instance, what is most important, as far as mantle convection is concerned, is clearly the strong temperature dependence of the viscosity which the laboratory-derived values of the activation energy and volume seem to suggest.

In Figure 2.1 (from [1]) I sketch the entire geodynamic spectrum spanning the whole range of phenomenological time scales in which rheology plays a fundamental role, distinguished on the basis of their characteristic time scale. In the left part of the graph we think of the Earth as an-elastic solid because it is characterized by all those fast processes from a geodynamic point of view, such as seismology (1 sec) and post-seismic deformations, i.e. aseismic movements that occur on a regional/global scale following large earthquakes (10^4-10^8s). On the contrary, on the right side of the graph we can think of the Earth as a viscous fluid because it is characterized by all those slow processes from a geodynamic point of view. The first of the slow processes is called Post Glacial Rebound (PGR) which represents only one of the aspects of GIA [2] and is particularly manifest in the regions that were covered by thick ice sheets at the LGM, an aseismic process that occurs on a time scale of a few thousand years. Then there is the slowest process of all, connected to mantle convection (time scale of million years). In the central part of the graph we find a transition period, called Maxwell time, which separates slow processes from fast processes: a geodynamic process has a duration of Maxwell time when its characteristic duration is around 10^3 years [3]. On the basis of these assumptions, on ”intermediate” time scales, we can define the Earth as a Maxwell body, i.e. a viscoelastic body with properties of elasticity and viscosity at the same time. The simplest way to attempt to mathematically describe this behavior is to model the material as a mechanical ”continuum”, in which the dual nature, elastic and viscous, is taken into account. The quantitative relationships that link the state of stress and the kinematics of deformation are called constitutive equations.

However, the appropriate constitutive relation which is to be employed in analyzing transient geodynamic phenomena, such as GIA, has often been the matter of controversy in geophysics [1]. On the one hand, the advocates of non-linear rheology [4] use as supporting arguments the laboratory data of single-crystal olivine whose power law index is about three [5, 6]. On the other side there is mounting evidence that at the stress levels in post glacial rebound the creep mechanism may in fact be linear for polycrystalline aggregates [7]. There are also recent theoretical studies indicating that the power law index changes gradually with stress [1, 8].

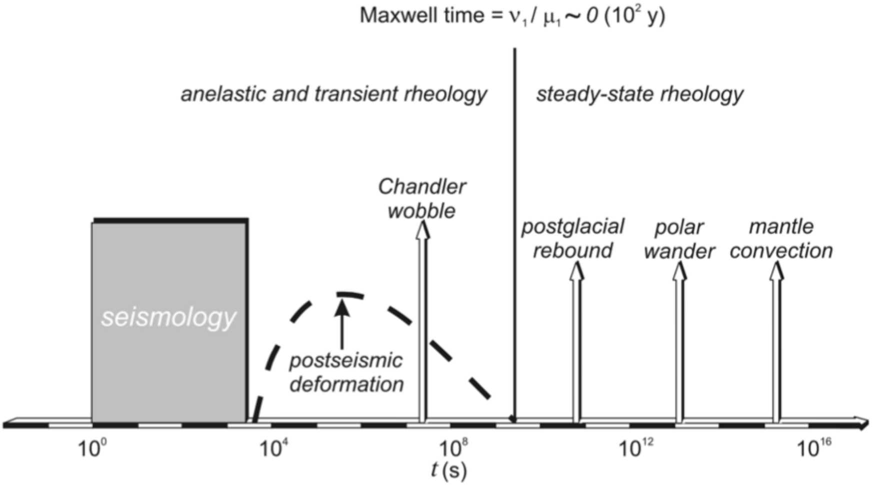

Figure 2.1. The geodynamic spectrum time scale (from [1])

2.1.2 The solid Earth's structure

From a geophysical point of view, the solid Earth is a multi-layered, oblate spheroid. Its outer layer is the crust, which has an average thickness of 35 km beneath the continents and ∼7-8 km beneath the oceans. The crust forms the upper part of the lithosphere, which is typically 100 km thick, and is the section of the Earth that participates in plate tectonics. Beneath the lithosphere lies the mantle, which extends down to ∼2900 km [9].

However, GIA modeling, consists of two parts, an Earth model and an ice reconstruction, where the latter is imposed as a boundary condition on the former. Various methods to set up the Earth model exists while the ice reconstruction is usually either based on observational data of the GIA process or from thermo-mechanical modeling.

Assuming the VM7 rheological profile [10], the model of the Earth used in this thesis work, and in all related documents, can be briefly described as follows:

- a 75 km thick elastic lithosphere;
- a three-layer upper mantle;
- a transition zone
- a three-layer lower mantle
- an inviscid fluid core

the depth of each single layer and the respective viscosity are shown in Figure 2.2.

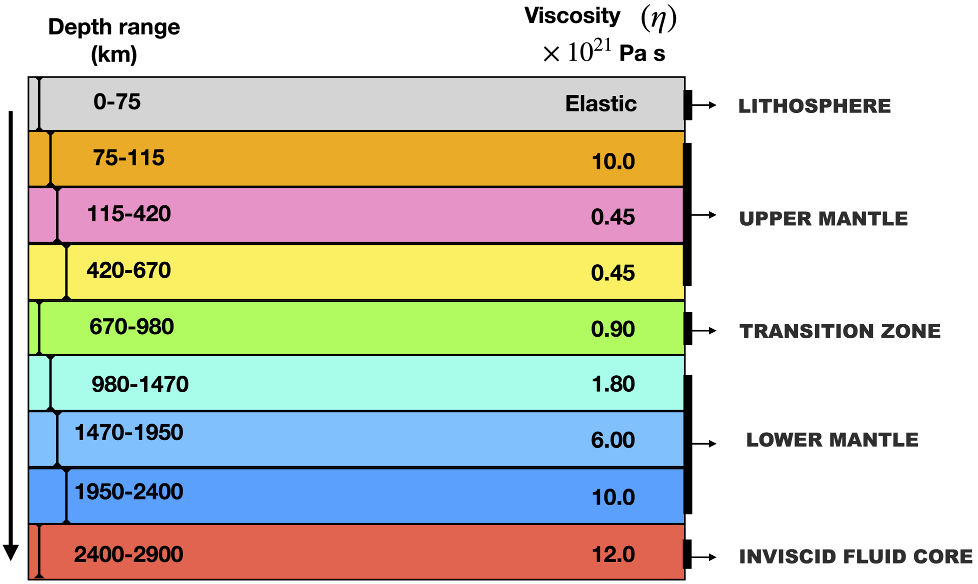

Figure 2.2. Radial viscosity structure of VM7 viscosity profile down to the core–mantle boundary.

2.1.3 Viscoelasticity and the Maxwell Body

A constitutive model describes the response of a material to external forces. An elastic body subjected to a force will deform instantaneously, and upon removal of the force immediately return to its initial shape. This is the typical behavior we find in a solid and is expressed by Hooke's law (relation between stress and strain). Conversely a fluid, in response to an applied force, will continuously deform and upon removal of the force, remain in its deformed shape, mathematically expressing a relationship between stress and strain rate. Many materials, including the Earth's mantle, display both elastic and viscous properties and are therefore referred to as viscoelastic materials. The simplest viscoelastic model which can describe the Earth as an elastic body, for short time scales, and as a viscous fluid, for long time scales, is the Maxwell mode, often conceptualized as a spring (the elastic component) connected in series with a dashpot (the viscous component), as show in Figure 2.3, where E represent the elastic behavior and η represent the viscous behavior. Other constitutive models, for example, include the Kelvin-Voigt model (parallel connected spring and dashpot), the standard linear solid (spring parallel to a Maxwell model), the Burgers body (Maxwell and Voigt model in series) and the generalized Maxwell model, known as the Maxwell-Wiechert model (several Maxwell models and possibly a Voigt model in parallel).

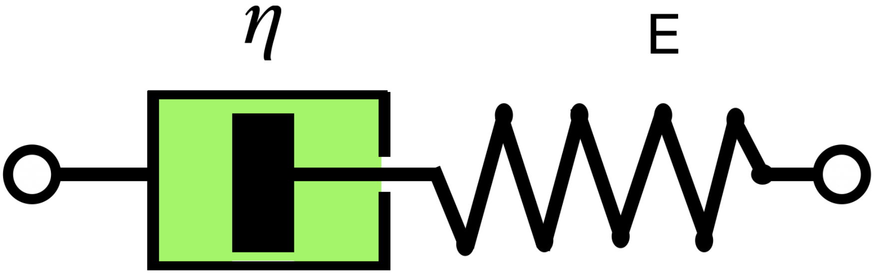

Figure 2.3. Mechanical analog of Maxwell rheology. A spring connected in series with a dashpot.

In other words, when a material is subject under a constant stress, the strain has two components. First, an elastic component occurs instantaneously, corresponding to the spring, and relaxes immediately upon release of the stress. The second is a viscous component that grows with time as long as the stress is applied. The constitutive relation is expressed as:

$$\sigma + \frac{\eta}{E}\dot{\sigma} = \eta\dot{\varepsilon} \tag{2.1}$$

where σ denote the stress, η is the viscosity, E is the elastic modulus (Young's modulus), $\dot{\sigma}$ and $\dot{\varepsilon}$ are time derivative of stress and strain respectively.

As mentioned, the Earth is usually assumed to be a Maxwell body, and this is also the assumption used in this thesis and in all related papers.

2.2 The theory behind GIA

Numerical predictions of sea-level variations due to GIA are non-trivial, in fact, sea-level changes influence the gravitational field of the planet, since they act, in addition to the ice mass, as a surface load [11]. However, these variations are also governed by the gravitational field, since the sea-level surface (or geoid) is constrained to remain an equipotential.

The basic idea of the "sea-level equation" (SLE) back to Woodward (1888) [12] that published his pioneering work on the form and position of mean sea level. Subsequently, first Platzman (1971) [13] and then Farrell and Clark (1976) [14] describe for the first time the integral equation governing the redistribution of ocean mass on a non-rotating planet, known as the SLE. Since then, a series of papers addressing the problem of SLE have been published (*e.g.,* [15–18]).

This section, following the fundamental papers by Spada and Stocchi (2007) [19] and Spada and Melini (2019) [20], is dedicated to the concept of surface loads and the study of SLE.

2.2.1 Surface load

If we consider the system composed of ice and ocean water at a given time t, its mass can be expressed as:

$$M(t) = \int_e L dA \tag{2.2}$$

where $M(t)$ is the mass distributed over the whole Earth's surface in the form of ice or water, $L(\gamma, t)$ is the surface load with γ stands for (θ, λ) (θ is co-latitude, λ longitude), $\int_e$ represents the integration of the whole Earth's surface and dA is the area element:

$$dA = a^2 \sin\theta d\theta d\lambda. \tag{2.3}$$

From Eq. 2.2, L can be expressed as the sum of two contributions, representing respectively (i) the load exerted by continental ice and (ii) the load of water on the ocean floor:

$$L(\gamma, t) = \rho^i IC + \rho^w BO \tag{2.4}$$

where I is the ice thickness, ρ^i and ρ^w are the density of ice and water respectively, O is the Ocean Function (OF), C = 1 - 0 is the Continental Function (CF) and $B(\gamma, t) = -T$ is sea level, with T representing the rocks topography [21]. Note that due to horizontal coastal migration and the transition between drift ice and continental ice, OF and CF are, in general, time dependent.

Consequently, using Eq. 2.4 in Eq. 2.2, the mass change $M(t) = M$ - M_0 of the system composed of ice and water is:

$$M(t) = \rho^i \int_e (IC - I_0C_0)dA + \rho^\omega \int_e (BO - B_0O_0)dA \tag{2.5}$$

where the subscript 0 denotes reference quantities and the first term on the right-hand side represents the mass change of continental ice.

Since mass must be conserved, we have:

$$M = \int_e \mathcal{L} dA = 0, \tag{2.6}$$

where

$$\mathcal{L}(\gamma, t) \equiv L - L_0, \tag{2.7}$$

represents the surface load variation that is defined as the difference between the actual surface load and its value in a previous reference state. $\mathcal{L}(\gamma, t)$ is given by the sum of three contributions:

$$\mathcal{L}(\gamma, t) = \mathcal{L}^a + \mathcal{L}^b + \mathcal{L}^c, \tag{2.8}$$

where the first term, $\mathcal{L}^a$, is associated with the change in ice thickness, the second term, $\mathcal{L}^b$, results from sea level change and the third, $\mathcal{L}^c$, is associated with the change in ocean function. For further details, the reader is referred to [20] and its supplement material.

2.2.2 The Sea Level Equation

To a first order approximation, the sea level at any point in time coincides with a gravitational equipotential surface. Redistribution of the Earth's mass, changing the gravitational potential, will therefore lead to local deviations in sea level compared to the eustatic level. The change in the sea level during a glacial period will in itself result in an isostatic adjustment process of the Earth due to the changing surface load [9].

The Sea Level Equation (SLE), first introduced by Farrell and Clark (1976) [14], has evolved through a series of papers since the 1970s [14, 22–25] to include the effect of shoreline migration, floating of marine grounded ice, Earth rotation, 3D Earth structure and ice lakes.

The SLE is used to describe the sea level variation produced by glacio-isostatic processes: a reference state of the system, composed of oceans, ice and solid Earth, is compared to a subsequent arbitrary state (i.e. a state in which the terrestrial topography will have a certain shape, the thickness of the ice will have a certain trend, etc. . .). In this evolving condition it is possible to measure the sea level in a certain point (using tide gauges): we will therefore say that the sea-level, in a certain point, is the difference between two quantities.

Above, sea-level has been defined as B = -Tr, where Tr is the topography. Indicating with $r^{ss}(\gamma, t)$ and $r^{se}(\gamma, t)$ the radii of the (equipotential) sea surface and of the solid Earth in a geocentric reference frame with origin in the whole-Earth center of mass *(CM)*, respectively, sea level can be expressed as:

$$S(\gamma, t) = r^{ss} - r^{se}, \tag{2.9}$$

and, introducing the sea surface variation, or absolute sea-level change

$$N(\gamma, t) = r^{ss} - r_0^{ss}, \tag{2.10}$$

and the vertical displacement of the Earth's surface

$$U(\gamma, t) = r^{ss} - r_0^{ss}, \tag{2.11}$$

we get:

$$S(\gamma, t) = N - U. \tag{2.12}$$

Equation 2.12 represents the most basic form of the SLE. We note that, being defined as a double difference, relative sea-level change $S(\gamma, t)$ is not dependent upon the choice of the origin of the reference frame, i.e., it is an absolute quantity, while $N(\gamma, t)$ and $U(\gamma, t)$, however, depend on the choice of the origin. Thus, sea-level variation is nothing more than the study of the mutual relationship between the geoid and the topography. S is the relative sea-level variation, measured by the tide gauges (linked to the solid Earth), N is the elevation variation of the sea surface measured with respect to the center of the Earth and U is the vertical displacement of the bedrock (see Figure 2.4).

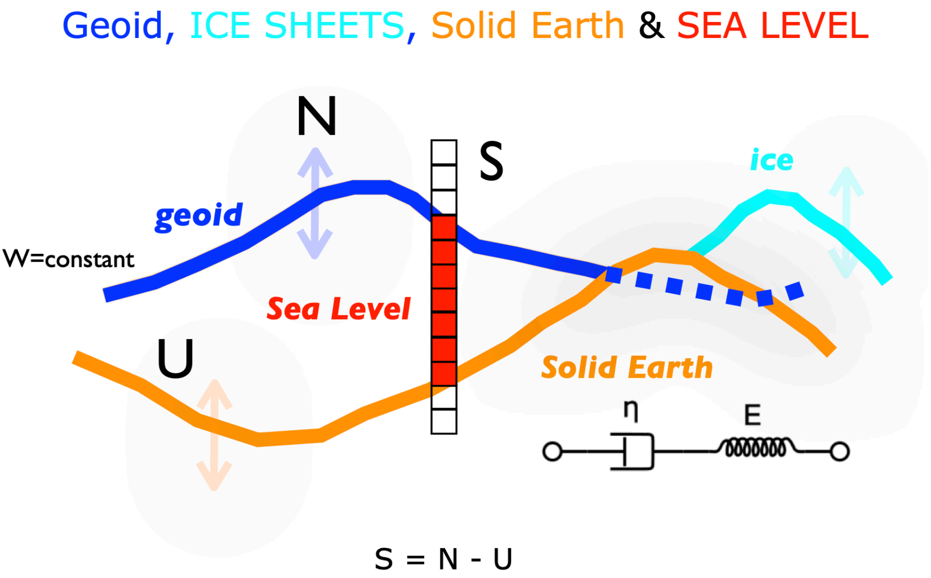

Figure 2.4. Sketches of the three Earth's components that are interacting in the SLE: the solid Earth, the oceans and the ice sheets. Bottom right, Maxwell's model.

The sea surface variation $N(\gamma, t)$ is closely associated to the variation of the geoid height. Farrell and Clark (1976) [14] have shown that the sea surface height variation is:

$$N(\gamma, t) = G + c, \tag{2.13}$$

where

$$G = \frac{\Phi}{g} \tag{2.14}$$

is the variation of the geoid radius relative to the reference state, with Φ that represents the variation of the total gravity potential of the Earth system, g represents the reference surface gravity acceleration evaluated on the Earth's surface and c is notorious within the GIA community as the 'c-constant' by Farrell and Clark [14]. So, the SLE of Eq. 2.12 becomes:

$$S(\gamma, t) = R + c, \tag{2.15}$$

with

$$R(\gamma, t) = G - U, \tag{2.16}$$

can be called a ‘sea-level response function’.

Assuming that the responses to surface loading and changes in centrifugal potential can be combined in a linear fashion, the SLE in Eq. 2.15 can be re-written as:

$$S(\gamma, t) = R^{sur} + c + R^{rot}, \tag{2.17}$$

where:

$$R^{sur}(\gamma, t) = G^{sur} - U^{sur}, \tag{2.18}$$

and

$$R^{rot}(\gamma, t) = G^{rot} - U^{rot}. \tag{2.19}$$

are the surface and the rotation sea-level response functions ($SRFs$), while

$$G(\gamma, t) = G^{sur} + G^{rot}, \tag{2.20}$$

and

$$U(\gamma,t) = U^{sur} + U^{rot}, \tag{2.21}$$

are the "geoid $SRFs$" and the "vertical displacement $SRFs$", respectively. The first, associated with height variations of the geoid, the second associated to vertical displacements of the Earth's surface.

From the mass conservation constraint given by Eq. 2.6, the constant c is easy to determine. Therefore, Eq. 2.17 becomes:

$$S(\gamma,t) = S^{ave} + (R^{sur} - < R^{sur} >^o) + (R^{rot} - < R^{rot} >^o), \tag{2.22}$$

where $< \ldots >^o$ denotes the average over the ocean surface (time dependent), defined by $O = 1$, and

$$S^{ave}(t) = S^{equ} + S^{ofu}, \tag{2.23}$$

where S^{equ} and S^{ofu} are two spatially invariant terms. The first, S^{equ}, represents the "equivalent sea level" and is

$$S^{equ}(t) \equiv -\frac{\mu}{\rho^{w} A^{o}}, \tag{2.24}$$

with μ is the ice mass change and A^o is the area of the oceans, while the second term, S^{ofu} is given by

$$S^{ofu}(t) \equiv \frac{1}{A^{o}} \int_{e} T_0 \mathcal{O} dA, \tag{2.25}$$

and depends exclusively on the variations of the OF, due to the coastline horizontal migration or the transitions from continental ice to floating ice (or vice versa). As a consequence of this, from Eq. 2.22 we see that, the regional fingerprints of GIA, on relative sea-level is determined by the functions R^{sur} and R^{rot}. Following [25], the $SRFs$ in Eq. 2.22 is obtained from a 3-D space-time convolution

$$R^{sur}(\gamma, t) = \Gamma^{s} \otimes \mathcal{L} \tag{2.26}$$

where $\Gamma^s(\gamma, t)$ is the surface Green's function at seal-level. Therefore, using the surface load decomposition given by Eq. 2.8 in to Eq. 2.26 leads to

$$R^{sur} = R^{a} + R^{b} + R^{c} \tag{2.27}$$

In contrast to R^{sur}, the harmonic coefficients of the rotational response $R^{rot}(\gamma, t)$ are obtained directly from a 1-D time convolution

$$R^{rot}_{lm}(t) = \Upsilon^{s}_{l} * \Lambda_{lm}, \tag{2.28}$$

where Υ^{s}_{l} is the rotation response Green's functions, is the expansion of the coefficients of degree l and order m of the variation of the centrifugal potential Λ_{lm} associated with the variation of the portion of the axis of rotation of the Earth [25]. $\Lambda(\gamma, t)$ is substantially a spherical harmonic function of degree l = 2 and order $m = \pm 1$. Therefore, Eq 2.22 can be rewritten as:

$$S(\gamma, t) = S^{ave} + R^{'a} + R^{'b} + R^{'c} + R^{'rot}, \tag{2.29}$$

where the response functions are:

$$R^{'abc}(\gamma, t) = \; R^{abc} - < R^{abc} >^{o}, \tag{2.30}$$

and

$$R^{'rot}(\gamma, t) = \; R^{rot} - < R^{rot} >^{o} \; . \tag{2.31}$$

We note that $R^{'b}$ depends on OS through the variation of the surface load $\mathcal{L}^{b}$. Following [17], in view of the numerical solution of the SLE, is therefore convenient to transform Eq. 2.29 so that $Z = OS$ becomes the unknown instead of S. This is done by projecting Eq. 2.29 on OF, i.e. multiplying both sides of the SLE by O, obtaining the final form of the SLE:

$$Z(\gamma, t) = Z^{ave} + K^{a} + K^{b}(Z) + K^{c} + K^{rot}(Z), \tag{2.32}$$

where

$$Z(\gamma, t) = OS \tag{2.33}$$

with O is the OF and S is the sea-level change.

The dependence of K^b e K^{rot} on Z in Eq. 2.32 shows the implicit nature of SLE, which is a three-dimensional nonlinear integral equation. The spatial discretisation on the surface of the sphere is carried through the properties of the equal-area, icosahedron-shaped, spherical pixelization introduced by [26] and briefly described in Section. 2.3.2 above.

The material presented in this section extends the analysis first presented by [27] and [19]. For a complete mathematical formulation, the reader is referred to [20] and its supplement material.

2.3 Numerical modeling of GIA deformation

2.3.1 SELEN[4], a program for solving the sea-level equation

From the "satellite-altimetry-era" (1992-today), which allowed us to measure the sea level from space, GIA modeling and its applications have seen a considerable development [2], stimulated by the recognized important role that GIA has in our understanding of current sea-level rise. However, 1-D models represent an important contribution in the development of GIA theories, in fact, a number of GIA models characterized by different Earth's rheological profiles and the different history of the Late Pleistocene ice sheets have been proposed, constrained by sea-level proxies dating from the LGM (21 Kyr BP), providing increasingly accurate estimates of global mean secular sea-level rise [2]. The development and progress towards this goal required a number of significant breakthroughs so much so that concepts associated with GIA have begun to be incorporated into parallel fields of research [28]. Despite the GIA phenomenon now being tightly integrated into the science of global change [29], few efforts have been devoted so far to the development of open-source codes for the solution of the SLE, although several post-glacial rebound simulators and Love Number calculators have been made available to the community (e.g. [30–35]). For what concern Love numbers, first introduced by A.E.H Love (1911) [36], provide a complete description of the response of a planetary body to external, surface or internal perturbations and are a key ingredient of several geophysical applications [37]. In fact, they are essential to the solution of the Sea Level Equation [14] and are exploited in current numerical implementations of the GIA problem, either on millennial (see *e.g.,* [20]) or on decadal time scale (see *e.g.,* [33]). For a review of the development of GIA modeling, the reader is referred to [2, 9, 28].

In this thesis work, the sea-level simulator SELEN[4] has been used, first presented to the GIA modeling community by [19], who numerically implemented the SLE theory reviewed in [27]. SELEN uses the Love number calculator TABOO (see [30, 38, 39]) as a subroutine and tie to the Generic Mapping Tools (*GMT* [40]) for the construction of the present-day ocean function. Furthermore, in SELEN, the numerical integration of the SLE over the sphere takes advantage of the icosahedron-based pixelization proposed by Tegmark

(1996) and described briefly in Sec 2.3.2 below. Similarly, all the versions are based upon the pseudo-spectral method of [41–43] for the solution of the SLE.

The Earth models accessible by SELEN[4] are all characterized by the spherically symmetrical structure. In the literature, these models are often referred to as 'GIA 1-D models' (Figure 2.5), since the density, elastic and rheological parameters depend only on the radius r.

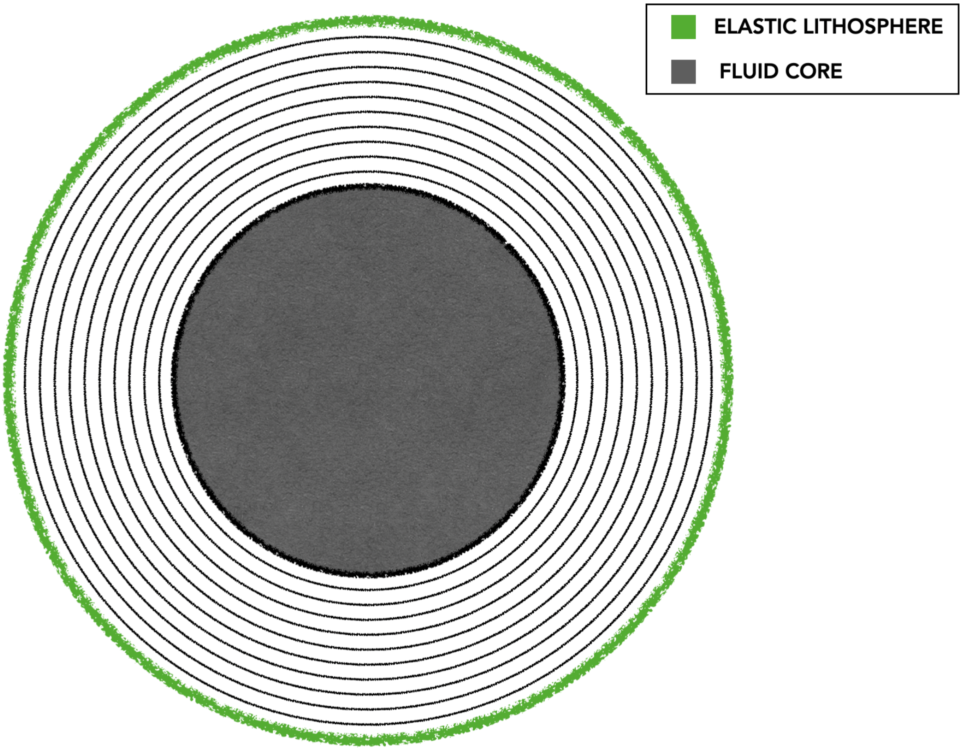

Figure 2.5. 1-D GIA model (spherically symmetrical). The elastic lithosphere is in green. The mantle is composed of Maxwell viscoelastic layers with arbitrary thickness, rheological parameters, stiffness and density. The uniform fluid nucleus is in grey.

2.3.2 Some words about Tegmark grid

As discussed in Spada et al. (2019a) [20] and Spada et al. (2019b) [44], in SELEN the spatial discretization of the SLE is accomplished on the equal-area, icosahedron-shaped pixelization of the sphere first introduced by Tegmark (1996) [26] and employed in astrophysics to study the Cosmic Microwave Background [45]. The grid is particularly convenient for the manipulation of harmonic functions, for the computation of power spectra, and for the numerical evaluation of surface integrals (quadrature) on the sphere. Here, I briefly explain how it works.

The Tegmark grid is characterised by a resolution parameter R_{res} that determines the density of the pixels on the surface of the unit sphere, and consequently the size of the grid cells. For a given value of R_{res}, the number of pixels on the grid is:

$$P = 40R_{res}(R_{res} - 1) + 12 \tag{2.34}$$

where each pixel is the center of slightly distorted, hexagonal equal-area grid cells. For a given pixelization, the cell area is

$$A^c = \frac{4\pi a^2}{P} \tag{2.35}$$

where $a = 6371$ km is Earth's radius. Thus, the angular half-amplitude of a disk on the sphere having an area A^c, is

$$\delta = \frac{180^\circ}{\pi} \cos^{-1}\left(1 - \frac{2}{P}\right) \tag{2.36}$$

where δ is expressed in degrees. For a sufficiently large number of pixels, the cell can be assimilated to a disk on a plane. An approssimate value for the radius of the disk is

$$r_{cell} \approx \frac{2a}{\sqrt{P}} \tag{2.37}$$

an expression which is useful to obtain a quick estimate of the grid spacing.

2.3.3 TABOO, a posT glAcial rebOund simuletOr

To model the Earth's viscoelastic response to ice load changes, in the Alpine regions, from LGM to present, has been used the open source TABOO software [38, 39] to compute the vertical displacements $\dot{U}$. Due to its relatively small size, in fact, no Alpine component is included in the most recent global GIA models such as ICE-7G_NA [10, 46], therefore, to do this, the ice chronology proposed by Seguinot (2019) [47] that was used which was converted into axisymmetric disk-shaped elements suitable for use with TABOO. However, TABOO is not a sea level equation solver.

The modelling procedure is based on the Green's functions formalism introduced by [48] and extended by [22], where vertical displacement and geoid change Green's functions represent the response of the solid Earth to a unit load applied on its surface. The model used here is caracterized by a non-rotating, incompressible, self-gravitating and spherically symmetric Earth model and uses axial-symmetric disks to describe surface loads [30, 38, 39].

This process will be detailed in the following Chapter 3, where I will focus on the Mediterranean basin and in particular on the Venetian Lagoon, a region where a large number of past observations of relative sea level have been collected.

Bibliography

[1] Roberto Sabadini, Bert Vermeersen, and Gabriele Cambiotti, *Global dynamics of the Earth*, Springer, 2016.

[2] Giorgio Spada, "Glacial isostatic adjustment and contemporary sea level rise: An overview", *Surveys in Geophysics*, vol. 38, no. 1, pp. 153–185, 2017.

[3] Giorgio Ranalli, *Rheology of the Earth*, Springer Science & Business Media, 1995.

[4] H Jay Melosh, "Cratering mechanics-observational, experimental, and theoretical", *Annual Review of Earth and Planetary Sciences*, vol. 8, no. 1, pp. 65–93, 1980.

[5] Christopher Goetze, "The mechanisms of creep in olivine", *Philosophical Transactions of the Royal Society of London. Series A, Mathematical and Physical Sciences*, vol. 288, no. 1350, pp. 99–119, 1978.

[6] B William Durham and Christopher Goetze, "Plastic flow of oriented

single crystals of olivine: 1. mechanical data", *Journal of geophysical Research*, vol. 82, no. 36, pp. 5737–5753, 1977.

[7] Christian Relandeau, "High temperature creep of forsterite polycrystalline aggregates", *Geophysical Research Letters*, vol. 8, no. 7, pp. 733–736, 1981.

[8] W Geoffrey Greenwood, H Jones, and T Sritharan, "On the transition between dislocation and diffusion creep", *Philosophical Magazine A*, vol. 41, no. 6, pp. 871–882, 1980.

[9] Pippa Whitehouse, "Glacial isostatic adjustment and sea-level change", *State of the art report, Svensk Kärnbränslehantering AB, Swedish Nuclear Fuel and Waste Management Co., Stockholm*, p. 105, 2009.

[10] Keven Roy and Richard W Peltier, "Space-geodetic and water level gauge constraints on continental uplift and tilting over North America: regional convergence of the ICE-6G_C (VM5a/VM6) models", *Geophysical Journal International*, vol. 210, no. 2, pp. 1115–1142, 2017.

[11] Glenn A Milne and Jerry X Mitrovica, "Postglacial sea-level change on a rotating earth: first results from a gravitationally self-consistent sea-level equation", *Geophysical Journal International*, vol. 126, no. 3, pp. F13–F20, 1996.

[12] Robert S Woodward, "On the form and position of the sea level", Tech. Rep., Washington: Government Printing Office, 1888.

[13] George W Platzman, “Ocean tides and related waves”, *Mathematical problems in the geophysical sciences*, vol. 14, no. Part 2, pp. 239–291, 1971.

[14] E William Farrell and James A Clark, “On postglacial sea level”, *Geophysical Journal International*, vol. 46, no. 3, pp. 647–667, 1976.

[15] Richard W Peltier, William E Farrell, and James A Clark, “Glacial isostasy and relative sea level: a global finite element model”, *Tectonophysics*, vol. 50, no. 2-3, pp. 81–110, 1978.

[16] Patrick Wu and Richard W Peltier, “Glacial isostatic adjustment and the free air gravity anomaly as a constraint on deep mantle viscosity”, *Geophysical Journal International*, vol. 74, no. 2, pp. 377–449, 1983.

[17] X Jerry Mitrovica and Richard W Peltier, “On postglacial geoid subsidence over the equatorial oceans”, *Journal of Geophysical Research: Solid Earth*, vol. 96, no. B12, pp. 20053–20071, 1991.

[18] Giorgio Spada, Paolo Stocchi, et al., “Solving the sea level equation, part i, theory”, 2005.

[19] Giorgio Spada and Paolo Stocchi, “Selen: A fortran 90 program for solving the “sea-level equation””, *Computers & Geosciences*, vol. 33, no. 4, pp. 538–562, 2007.

[20] Giorgio Spada and Daniele Melini, “Selen 4 (selen version 4.0): a fortran program for solving the gravitationally and topographically self-consistent

sea-level equation in glacial isostatic adjustment modeling", *Geoscientific Model Development*, vol. 12, no. 12, pp. 5055–5075, 2019.

[21] Roblyn A Kendall, X Jerry Mitrovica, and A Glenn Milne, "On post-glacial sea level–II. Numerical formulation and comparative results on spherically symmetric models", *Geophysical Journal International*, vol. 161, no. 3, pp. 679–706, 2005.

[22] Richard W Peltier, "The impulse response of a maxwell earth", *Reviews of Geophysics*, vol. 12, no. 4, pp. 649–669, 1974.

[23] Dazhong Han and John Wahr, "Post-glacial rebound analysis for a rotating earth", *Slow Deformation and Transmission of Stress in the Earth*, vol. 49, pp. 1–6, 1989.

[24] Richard W Peltier, "Ice age paleotopography", *Science*, vol. 265, no. 5169, pp. 195–201, 1994.

[25] A Glenn Milne and Jerry X Mitrovica, "Postglacial sea-level change on a rotating earth", *Geophysical Journal International*, vol. 133, no. 1, pp. 1–19, 1998.

[26] Max Tegmark, "An icosahedron-based method for pixelizing the celestial sphere", *The Astrophysical Journal*, vol. 470, no. 2, pp. L81, 1996.

[27] Giorgio Spada and Paolo Stocchi, *The sea level equation, theory and numerical examples*, Aracne Editrice, Roma, 2006.

[28] L Pippa Whitehouse, "Glacial isostatic adjustment modelling: histori-

cal perspectives, recent advances, and future directions", *Earth surface dynamics*, vol. 6, no. 2, pp. 401–429, 2018.

[29] John A Church, Peter U Clark, Anny Cazenave, Jonathan M Gregory, Svetlana Jevrejeva, Anders Levermann, Mark A Merrifield, Glenn A Milne, R Steven Nerem, Patrick D Nunn, et al., "Sea level change", Tech. Rep., PM Cambridge University Press, 2013.

[30] Giorgio Spada, Andrea Antonioli, Lapo Boschi, Lapo Boschi, Valter Brandi, Spina Cianetti, Gabrielle Galvani, Carlo Giunchi, Bruna Perniola, Nicola Piana Agostinetti, et al., "Modeling earth's post-glacial rebound", 2004.

[31] Giorgio Spada, "Alma, a fortran program for computing the viscoelastic love numbers of a spherically symmetric planet", *Computers & Geosciences*, vol. 34, no. 6, pp. 667–687, 2008.

[32] Giorgio Spada, Valentina Roberta Barletta, Volker Klemann, REM Riva, Zdenek Martinec, Paolo Gasperini, Björn Lund, Detlef Wolf, LLA Vermeersen, and MA King, "A benchmark study for glacial isostatic adjustment codes", *Geophysical Journal International*, vol. 185, no. 1, pp. 106–132, 2011.

[33] Daniele Melini, Pascal Gegout, Matt King, Ben Marzeion, Giorgio Spada, et al., "On the rebound: Modeling earth's ever-changing shape", *Eos*, vol. 96, 2015.

[34] Michael Bevis, Daniele Melini, and Giorgio Spada, “On computing the geoelastic response to a disk load”, *Geophysical Journal International*, vol. 205, no. 3, pp. 1804–1812, 2016.

[35] B Samuel Kachuck and M Lawrence Cathles, “Benchmarked computation of time-domain viscoelastic love numbers for adiabatic mantles”, *Geophysical Journal International*, vol. 218, no. 3, pp. 2136–2149, 2019.

[36] Augustus Edward Hough Love, *Some Problems of Geodynamics: Being an Essay to which the Adams Prize in the University of Cambridge was Adjudged in 1911*, University Press, 1911.

[37] Daniele Melini, Christelle Saliby, and Giorgio Spada, “On computing viscoelastic love numbers for general planetary models: the alma3 code”, *Geophysical Journal International*, vol. 231, no. 3, pp. 1502–1517, 2022.

[38] Giorgio Spada, “The theory behind TABOO”, vol. XXX, 2003.

[39] Giorgio Spada, “TABOO-User guide”, 2003.

[40] Paul Wessel and Walter HF Smith, “New, improved version of generic mapping tools released”, *Eos, Transactions American Geophysical Union*, vol. 79, no. 47, pp. 579–579, 1998.

[41] X Jerry Mitrovica, JL Davis, and II Shapiro, “A spectral formalism for computing three-dimensional deformations due to surface loads: 1. theory”, *Journal of Geophysical Research: Solid Earth*, vol. 99, no. B4, pp. 7057–7073, 1994.

[42] X Jerry Mitrovica, John Wahr, Isamu Matsuyama, and Archie Paulson, “The rotational stability of an ice-age earth”, *Geophysical Journal International*, vol. 161, no. 2, pp. 491–506, 2005.

[43] X Jerry Mitrovica and John Wahr, “Ice age earth rotation”, *Annual Review of Earth and Planetary Sciences*, vol. 39, pp. 577–616, 2011.

[44] Giorgio Spada and Daniele Melini, “Supplement of SELEN 4 (SELEN version 4.0): a Fortran program for solving the gravitationally and topographically self-consistent sea-level equation in glacial isostatic adjustment modeling”, *Supplement of Geoscientific Model Development*, vol. 12, no. 12, 2019.

[45] Max Tegmark, Angelica de Oliveira-Costa, and Andrew JS Hamilton, “High resolution foreground cleaned cmb map from wmap”, *Physical Review D*, vol. 68, no. 12, pp. 123523, 2003.

[46] Keven Roy and Richard W Peltier, “Glacial isostatic adjustment, relative sea level history and mantle viscosity: reconciling relative sea level model predictions for the us east coast with geological constraints”, *Geophysical Journal International*, vol. 201, no. 2, pp. 1156–1181, 2015.

[47] Julien Seguinot, Susan Ivy-Ochs, Guillaume Jouvet, Matthias Huss, Martin Funk, and Frank Preusser, “Modelling last glacial cycle ice dynamics in the Alps”, *The Cryosphere*, vol. 12, no. 10, pp. 3265–3285, 2018.

[48] E William Farrell, “Deformation of the Earth by surface loads”, *Reviews*

of Geophysics, vol. 10, no. 3, pp. 761–797, 1972.

Chapter 3

ONGOING SEA-LEVEL RISE AND VERTICAL LAND MOVEMENTS IN THE VENETIAN LAGOON: THE CONTRIBUTION OF GLACIAL ISOSTATIC ADJUSTMENT FROM THE ALPINE ICE SHEET

Although the GIA contribution in northern Adriatic Sea has been the subject of various investigations so far, significant uncertainties still exist, especially related to the extent and chronology of the Würm Alpine ice sheet and to the rheological profile of the mantle. Here, taking advantage of the recent publication of updated deglaciation chronologies for the far field late-Pleistocene ice sheets and for the near-field alpine ice complex, are produced up-to-date estimates of the present-day rates of GIA-induced relative sea-level variations and vertical displacements in the Venetian Lagoon and in the northern Adriatic Sea, which are compared with GNSS and tide-gauge observations.

In this chapter I resume my publication on Geophysical Journal International, Volume 233, Issue 3, June 2023, Pages 2039–2052. See Appendix B for details.

3.1 Introduction

The Venetian Lagoon is a shallow coastal inlet located along the Adriatic Sea in northeastern Italy (see Figure 3.1), which originated nearly 6000 years BP at the apex of the Flandrian Transgression [1–3]. Since then, sea levels have undergone minor oscillations. In this area, the sea-level variations result from a range of simultaneous, interrelated processes of geodynamical, geological, and meteorological nature, as recently discussed by [4]. Among these, a potentially important contribution is given by GIA, the process arising from the interactions between the cryosphere, the solid Earth and the oceans in response to the melting of ice loads, has been introduced in Section 1.1. While sea-level signals caused by tectonic forces may exhibit a complex spatial and temporal variability (*e.g.* [5, 6]), those associated with GIA are characterized by smooth, long-wavelength patterns [7, 8]. However, [9] have shown that the regional variability of GIA in the Mediterranean is significant in spite of the relatively small extent of the basin, demanding the adoption of high resolution models.

Although the GIA contribution in northern Adriatic Sea has been discussed several times, significant uncertainties still exist, especially related with the extent and chronology of the Würm Alpine ice-sheet (from 26 to 9 Kyr BP) that, due to its proximity to the Venetian Lagoon and to the coasts of the northern Adriatic, is still affecting the isostatic equilibrium in these particular areas. This was first pointed out by [10], who studied the post-glacial rebound process occurring in the Swiss Alps and the surrounding regions using a simplified disk model (see discussion in [11]). Following the work of [10], [12] estimated the effects of melting of the Alpine ice sheet, including relative sea-level and geodetic signals. They focused on the GIA effects in the Po plain and along the coasts of the Adriatic Sea, extending results by [5] who only considered isostatic effects associated with the remote ice sheets, thus neglecting the possible role of the Würm Alpine glacier.

GIA in the northern Adriatic Sea has been the subject of various investigations, sometimes leading to contrasting results. For example, according to the GIA model based upon the K33_j1b_WS9_6 ice sheet history of [13], sea-level in Venice raised by about ~ 2.2 m over the past $5,000$ years, with present-day rates of relative sea-level change of ~ 0.4 mm/yr. Conversely, the ICE-7G_NA (VM7) GIA model by [14] predicts a substantially stable sea-level over the same period, pointing to a negative contribution of GIA to present-day sea-level change. In addition to the different rheological layering assumed in the two GIA models, these discrepancies are to be attributed to differences in the ice sheet chronologies, reflecting our still incomplete understanding of the spatial and temporal evolution of continental ice sheets during last millennia. Besides those global aspects, on the Northern Adriatic scale a major difference exists between those two GIA models. Indeed, ICE-7G_NA does not include glacial loads over the Alps, while models from the Kurt Lambeck group of the Australian National University (ANU) [13] contain an Alpine component, albeit it does not provide a detailed and up-to-date description of the evolution of regional ice loads; these differences are the most likely cause of inconsistent estimates of GIA in the Northern Adriatic between the various available so far models.

The availability of updated global GIA models like ICE-7G_NA (VM7) by [15, 16], which is expected to provide more precise assessments of the ongoing effects of GIA across the Mediterranean Sea [14], and the recent reconstructions of the Würm ice sheet over the whole last glacial cycle [17], whose implications upon vertical land movements across the Po plain and the surrounding regions have not yet been investigated, motivates a re-evaluation of GIA in the Venetian Lagoon using state-of-the-art numerical models recently developed [18], which allow a more comprehensive simulation of GIA processes and are able to attain high spatial resolutions. The latter aspect is of particular importance, in view of the narrow geographical extent of the northern Adriatic sea.

This Chapter is organized as follows. In Section 3.2 we review previously published results on sea-level change and vertical land motion in the Northern Adriatic, and we present our estimates of vertical velocities based on publicly available geodetic time series. In Section 3.3 we describe our approach to GIA modeling, including the effects of both remote and near-field ice sheets. Our numerical results are presented in Section 3.4, before discussing their geophysical interpretation in Section 3.5. Finally, my concluding remarks are outlined in Section 3.6.

3.2 Sea-level change and vertical land motion in the northern Adriatic

3.2.1 Tide gauge and altimetry observations

The Venetian Lagoon covers about 550 km^2 along $\sim$ 50 km of low-lying coast within the easternmost boundary of the Po Plain. It is connected to the northern Adriatic Sea through three tidal inlets, namely Lido, Malamocco and Chioggia (Figure 3.1), and is characterized by a marked vulnerability to coastal flooding due to extreme water heights [19]. The monitoring of sea-level changes in Venice relies on both *in situ* observations recorded by tide gauges and remote sensing data provided by satellite altimetry. Since tide

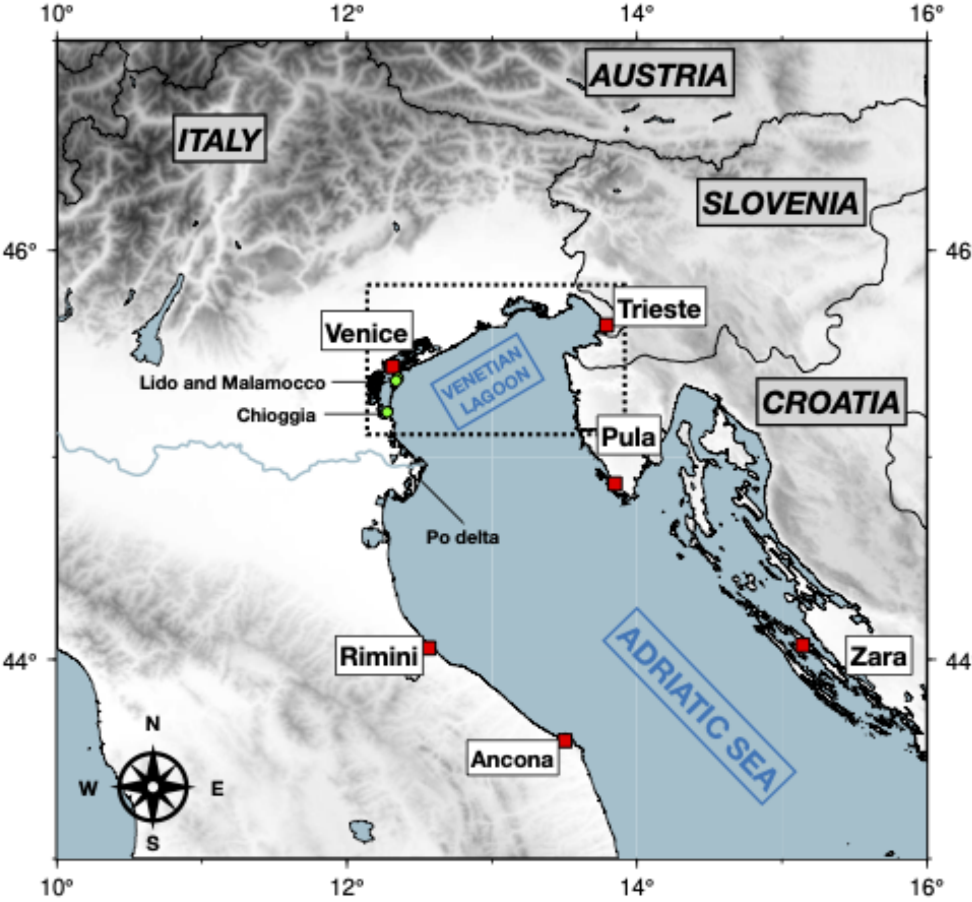

Figure 3.1. Overview of the study area. The dashed box corresponds to the region shown in Figure 3.2a. From [3].

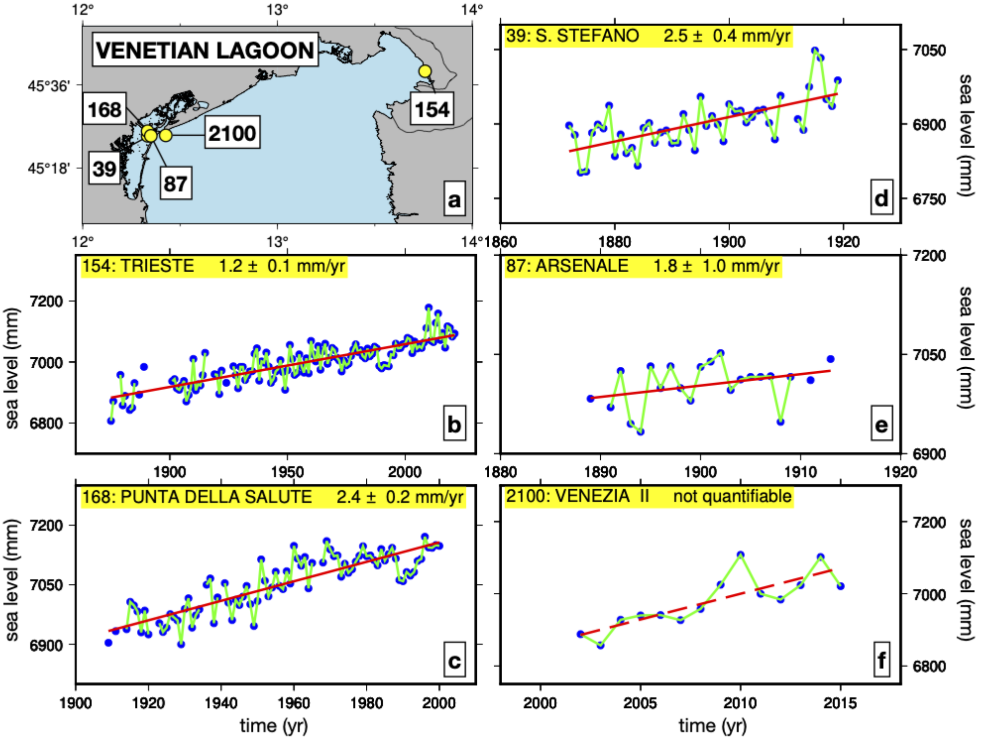

Figure 3.2. Location of PSMSL tide gauges in the Venetian Lagoon (a) and annual RLR time series for Trieste (c, ID: 154), Venezia Punta Della Salute (d, ID: 168), Venezia Santo Stefano (e, ID: 39), Venezia II (f, ID: 2100) and Venezia Arsenale (g, ID: 87). The red line in panels (b)-(e) is obtained with a linear regression of the tide gauge time series; the corresponding rate of sea-level change is reported in the panel headers. Note that the time ranges are different for frames (c)-(g). Data have been obtained from the PSMSL web page (`https://www.psmsl.org`. From [3].

gauges record sea-level relative to the solid Earth, they are expected to be affected significantly by vertical land movements and in particular by GIA (see *e.g.,* [4]).

Various estimates for the trend of secular sea-level rise in the Venetian Lagoon have been proposed in the literature. For an in-depth review, the reader is referred to [4]. Studies based on instrumental records have generally provided rates between 0.4 and 1.4 mm/yr [20–24]. The wide range of estimated rates depends, in part, on the relative duration of the tide gauge records used in these studies but it is also a consequence of anthropogenic factors, mainly the withdrawal of groundwater, which has varied in intensity through time [4, 25].

In this thesis work, I rely upon the tide gauge data made publicly available by the Permanent Service for Mean Sea Level (PSMSL, `http://www.pol.ac.uk/psmsl`). Those of Trieste and Venice (Venezia Punta Della Salute) are by far the longest spanning records [26, 27] in the northern Adriatic Sea (see Figure 3.2). For a summary of the record lengths and data availability from other sites, the reader is referred to [28]. The Revised Local Reference (RLR) records across the Adriatic Sea share similar temporal patterns, with inter-annual and inter-decadal components showing the same general trends and amplitudes [28]. The overall picture shows that the sea-level behaviour in the Adriatic Sea on these time scales is, to a large extent, uniform [29]. The longest-spanning station of Venice (Venezia Punta Della Salute) shows a trend of (2.4 ± 0.2) mm/yr, twice the trend of Trieste of (1.2 ± 0.1) mm/yr

[3, 27]. Two other tide gauge stations are available in Venice, both operating since early 20th century: Venezia Santo Stefano, with a trend of (2.5 ± 0.4) mm/yr [30], and Venezia Arsenale, with a trend of (1.8 ± 1.0) mm/yr [26]. Data from these stations are shown in Figure 3.2. Venezia Santo Stefano is characterized by a rate consistent with the value at Venezia Punta Della Salute, but note that the two records cover time windows that do not overlap. Although the rate of sea-level change at Venezia Arsenale is affected by a very large uncertainty, it is found to be in general agreement with rates from other tide gauges in the Venetian Lagoon. Conversely, the sea-level trend at Trieste is considerably smaller than rates in the Venetian Lagoon; this difference is likely to be the result of high rates of subsidence in the Venice area due to groundwater extraction activities. It is worth noting that the standard error for records longer than 50 years is less than 0.3 mm/yr while the two records exceeding 80 years (namely, Venezia Punta Della Salute and Trieste), have errors < 0.2 mm/yr, and for shorter records spanning about 25 years the error is > 0.6 mm/yr [26].

Furthermore, in Venice we have the chance of comparing the rates from tide gauge records with independent sea-level observations. For instance, on the basis of “photographic” evidence from the Venetian painters, [31] estimated that in the period 1727-2000 the average rate of sea-level rise in the lagoon has been (2.3 ± 0.4) mm/yr, consistent with the trends obtained with the longest tide gauge records available. I remark also that a long-term record of relative sea-level change is provided by tidal notches found in the northern

Adriatic [3]. The notches, whose age is only poorly determined, are currently located at depths ranging between 0.5 and 0.6 m below current sea-level. If they can be considered as relatively recent, as suggested by similar structures found in Roman jetties [32], then they may be consistent with a long term sea-level rise of ≥ 0.3 mm/yr.

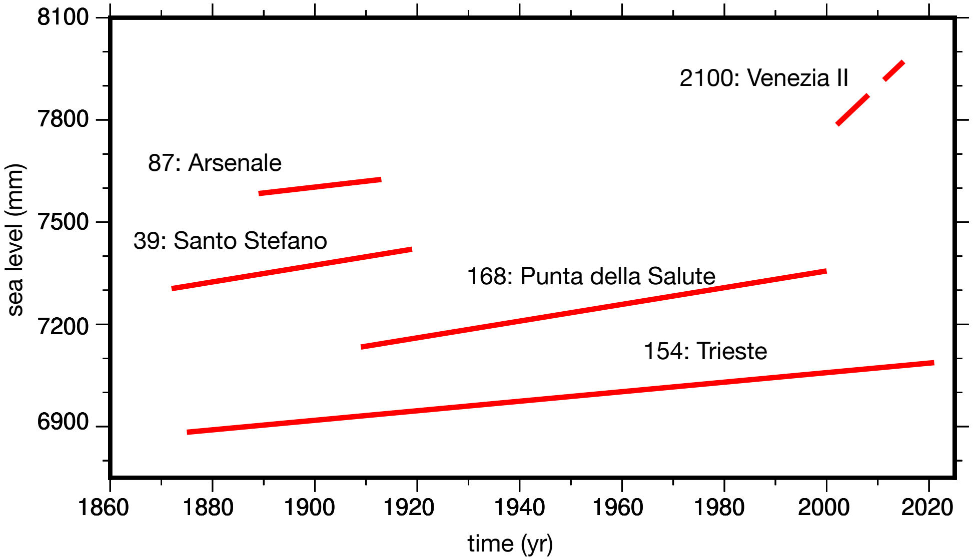

Figure 3.3. Comparison between sea-level change trends obtained from tide gauge records shown in Figure 3.2. From [3].

In contrast with the *in situ* observations from tide gauges, satellite altimetry observations are only available since the mid 70s. Their accuracy in estimating sea-surface height has increased considerably in the early 90s with the launch of the TOPEX/Poseidon satellite mission, and later with the Jason missions. An overall global-mean rate of absolute sea-level rise of ≈ 3 mm/yr during the "altimetry era" (*i.e.,* since year 1992) is reported by several studies (see, *e.g.*, [33, 34]). The quantity and quality of altimetry data for the northern Adriatic Sea and in the Venetian Lagoon has been recently thoroughly reviewed by [4], who estimated a trend of absolute sea-level rise of (5.9 ± 1.4) mm/yr over the period 1993-2008, at a point in the Adriatic Sea that lies $\sim$ 80 km away from Venice. In contrast, [35] obtained trends of (4.18 ± 0.92) mm/yr and of (3.40 ± 0.99) mm/yr during time periods 1993-2014 and 1993-2013, respectively, at a point that lies close to the Venetian tide gauges. In their reanalysis over the time period 1993-2015, [36] obtained a trend of (4.03±1.27) mm/yr after the removal of the seasonal component (see, *e.g.*, [37]). The above rates of absolute sea-level rise obtained for Venice and for the northern Adriatic clearly exceed the global average of $\approx$ 3 mm/yr observed by altimetry [33]. However, according to global studies, they also exceed (by one order of magnitude) the contribution that we expect from GIA, which according to state-of-the-art models is close to 0.3 mm/yr when averaged over the oceans (see, *e.g.*, [38, 39]). Local predictions, specific for this study, shall be provided in the following using updated GIA models.

3.2.2 GNSS observations

Vertical land movement (VLM) constitutes a very important contribution to the variability of sea-level in the Venetian Lagoon [3, 4, 40]. VLM results from the combination of different components due to tectonics, sediment loading and compaction, GIA and anthropogenic activities [25, 41]. In the Venice area, all these components induce non-negligible displacements although their magnitude and relative importance have changed over time. The net result is a coastal subsidence that exacerbates the effects of climate-driven sea-level rise [4].

In this thesis work I have analyzed 45 GNSS time series for the Venetian Lagoon and the surrounding areas, distributed from the Nevada Geodetic Laboratory (NGL) at the University of Nevada, Reno. Details on the data set are available on the NGL webpage (`http://geodesy.unr.edu/index.php`). Following [42], [43] and [44], we considered only time series whose length is at least 2.5 years. Indeed, according to Blewitt and Lavallée (2002) [45], this is the minimum acceptable length to ensure that estimated trends are not significantly affected by biases due to seasonal components in the displacement time series. To estimate vertical velocities from the GNSS time series was used the MIDAS (Median Interannual Difference Adjusted for Skewness) median-trend algorithm introduced by [46]. We also use the equipment changes tabulated by NGL from station “site logs” (i.e., antenna/radome changes and receiver make changes). The MIDAS trend estimator can handle common problems such as step discontinuities, outliers, seasonality, skewness, and heteroscedasticity, and it represents a variant of the Theil-Sen non-parametric median trend estimator [47, 48]. The MIDAS-estimated velocity is essentially the median of the distribution of 1 year slopes, making it insensitive to the effects of steps in the time series if are sufficiently infrequent. The uncertainties obtained through the MIDAS algorithm have a realistic meaning and usually do not require further scaling (see *e.g.,* [49–53]. Thus, time series length must be greater than one year such that at least one full cycle of periodic seasonal behavior, if it exists, is captured, and any transient signals can be distinguished from secular behavior. The differencing of pairs separated by a year minimizes effects with annual periodicity, but not other transient signals with different periodicity as suggested by [54].

Figure 3.4 shows the location of the 45 GNSS sites considered in this work, the vertical velocity v that I obtained at each site and the associated uncertainty σ_v. Numerical values of $(v \pm \sigma_v)$ for each GNSS site are listed in Tables 3.1 and 3.2. The length of the individual time-series are shown in Figure 3.5 while the MIDAS processing are shown in Figures 3.6, 3.7, and 3.8 respectively.

We note that among those considered in Figure 3.4a, I obtain a positive vertical velocity (*i.e.*, an uplift) at only 7 stations out of 45: TREV (0.71 ± 0.87 mm/yr), VOLT (0.97 ± 0.76 mm/yr), BASS (0.15 ± 1.36 mm/yr), MT06 (0.29 ± 1.04 mm/yr), MT10 (0.68 ± 0.87 mm/yr), MGRD (0.53 ± 0.57 mm/yr), and VITT (0.23 ± 0.77 mm/yr). The map in Figure 3.4a clearly highlights the diffuse state of subsidence in the Venice region and in the surroundings. Subsidence rates reach the maximum value of (-5.75 ± 2.54) mm/yr at MST1, in the Mestre Metropolitan City of Venice. Large subsidence rates are also found at TGPO $(-5.26 \pm 0.65$ mm/yr) and at PTO1 $(-5.15 \pm 0.76$ mm/yr), in the Po Delta. The weighted average of vertical velocities over all the considered stations is (-1.35 ± 0.10) mm/yr.

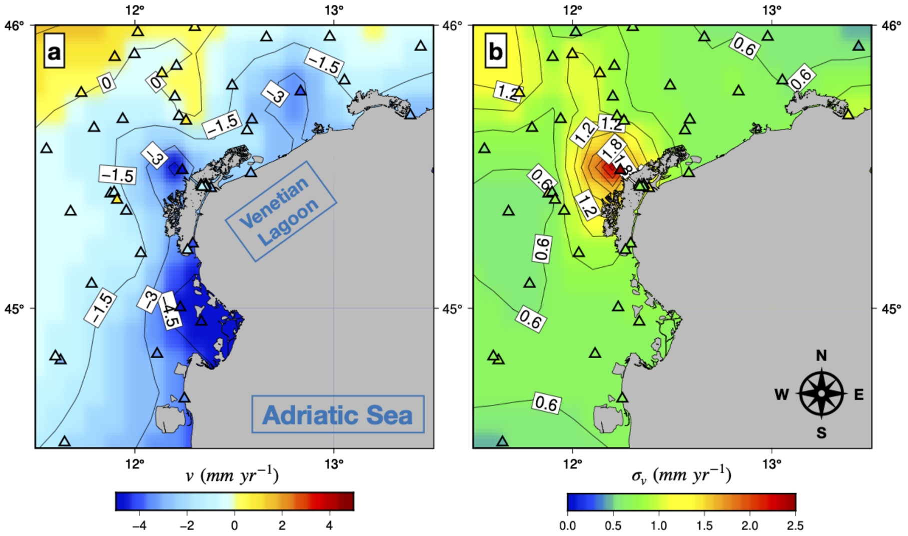

Figure 3.4. Estimated vertical velocities (v, a) and associated uncertainties (σ_v, b) at the 45 GNSS sites considered in this work. An interpolated field for v and σ_v is also shown. Note that the color scale in (a) is saturated at ±5 mm/yr. The interpolation has been obtained with program `surface`, which is part of the GMT (Generic Mapping Tools) package by [55], employing a tension factor of 0.5.

3.3 Glacial Isostatic Adjustment

In what follows, I discuss our new model estimates of GIA in the Northern Adriatic. We considered separately two contributions: *i)* the effect of global-scale GIA in response to the melting of late-Pleistocene ice sheets, which are

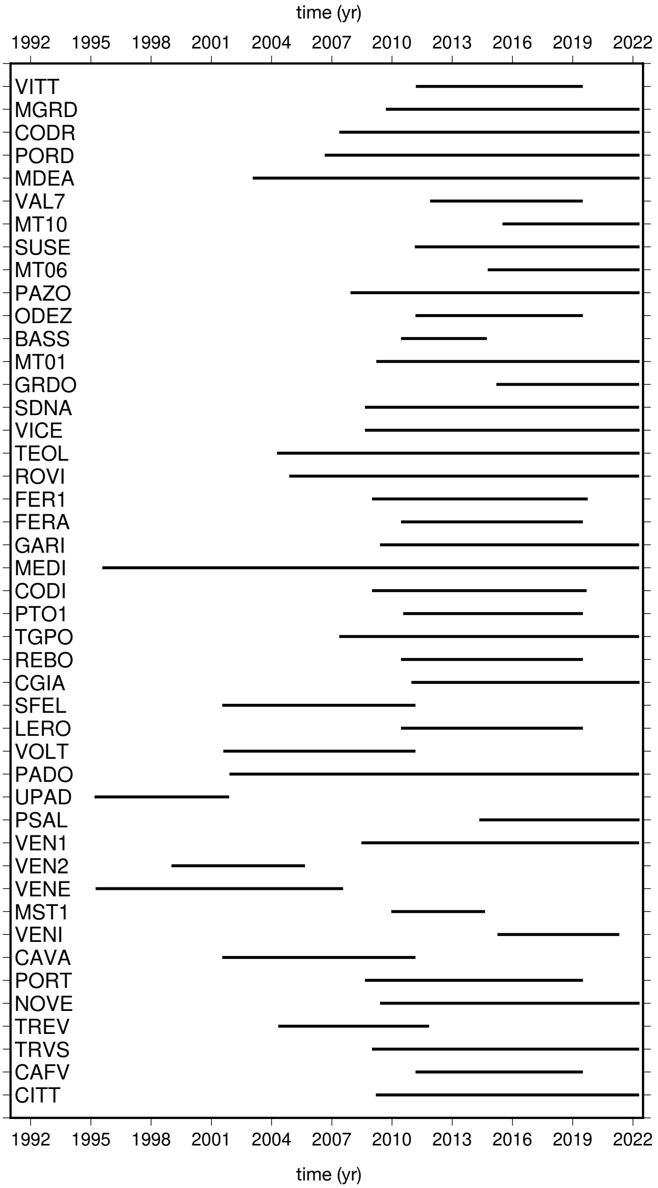

Figure 3.5. Time windows covered by the 45 GPS time series of vertical displacement considered in this work.

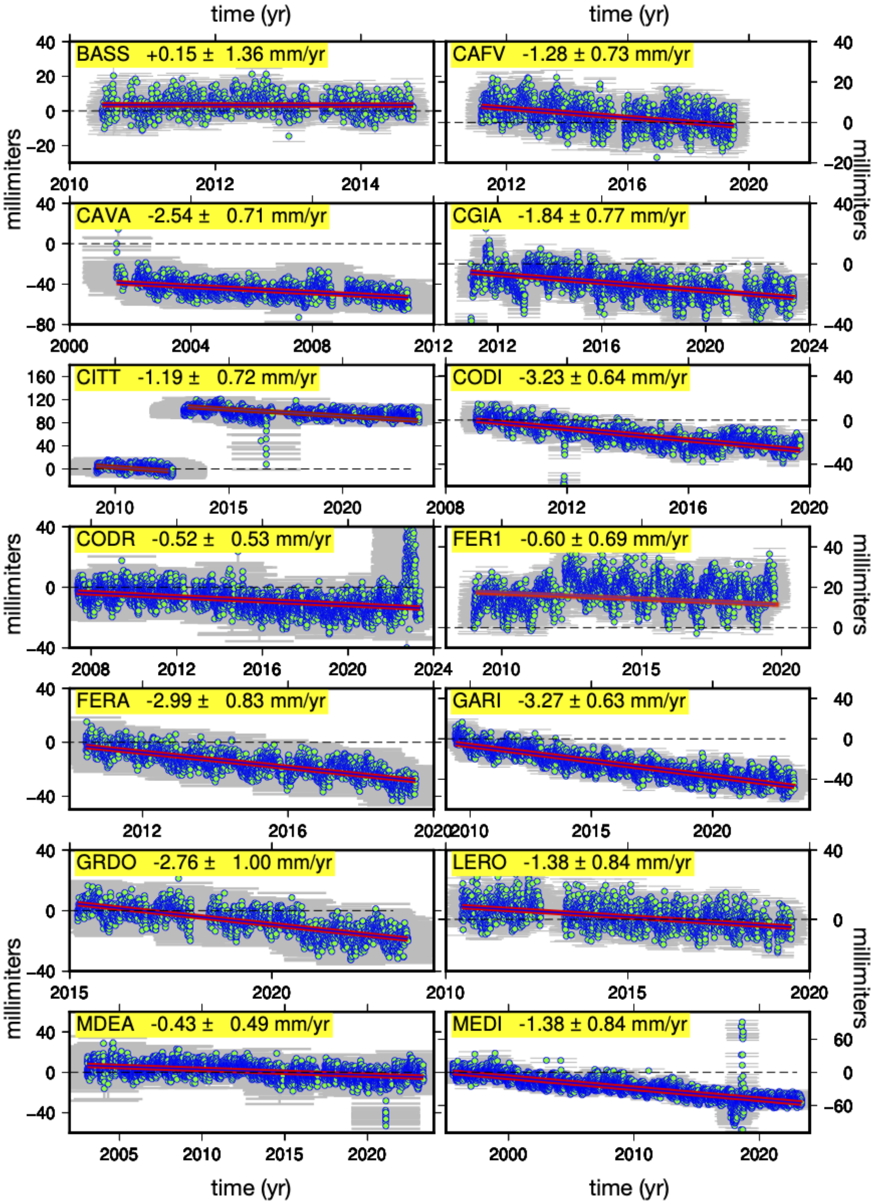

Figure 3.6. GNSS daily time series (up-component). The red line represents the GPS velocity computed by MIDAS [46], and the green solid circles represent the offset daily coordinate time series. Note that both horizontal and vertical axes vary.

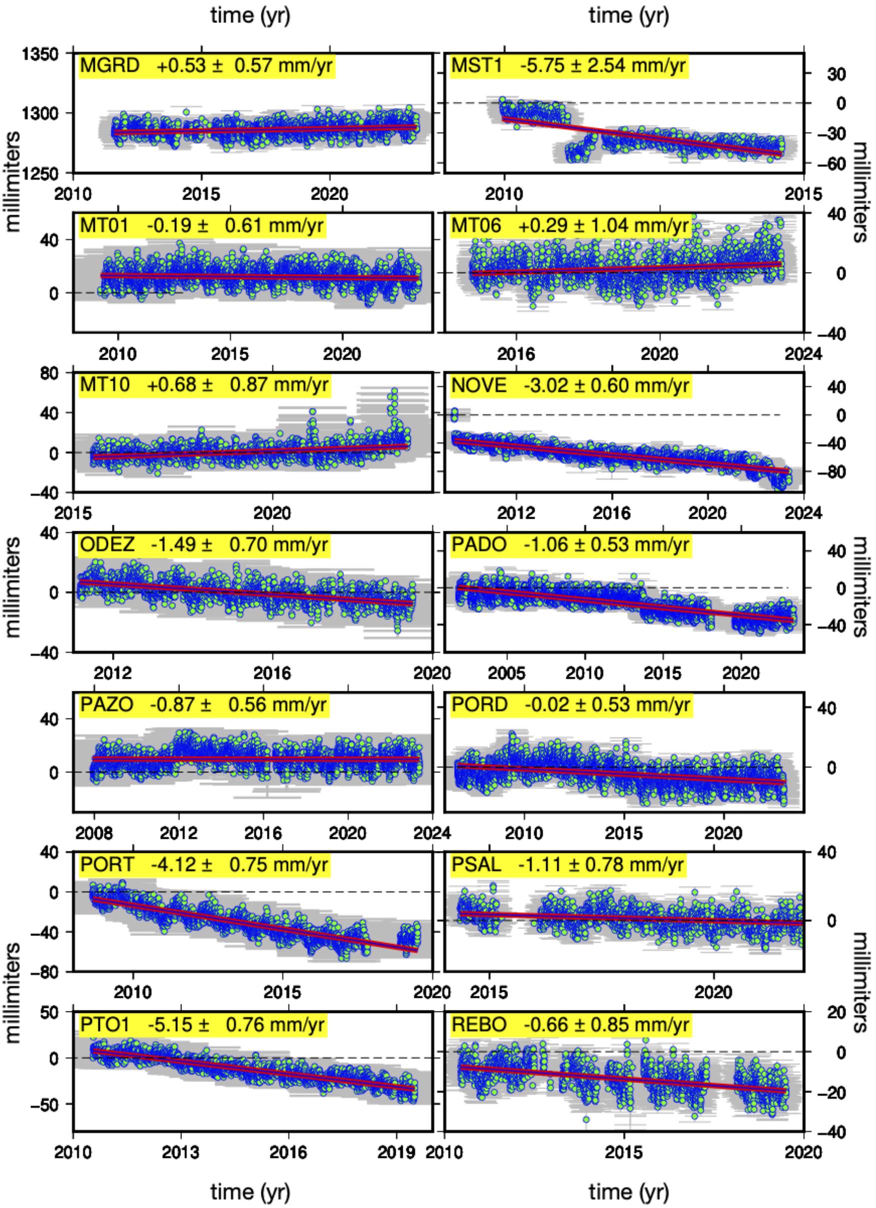

Figure 3.7. GNSS daily time series, namely the up-component. The red line represents the GPS velocity computed by MIDAS [46], and the green solid circles represent the offset daily coordinate time series. Note that both horizontal and vertical axes vary.

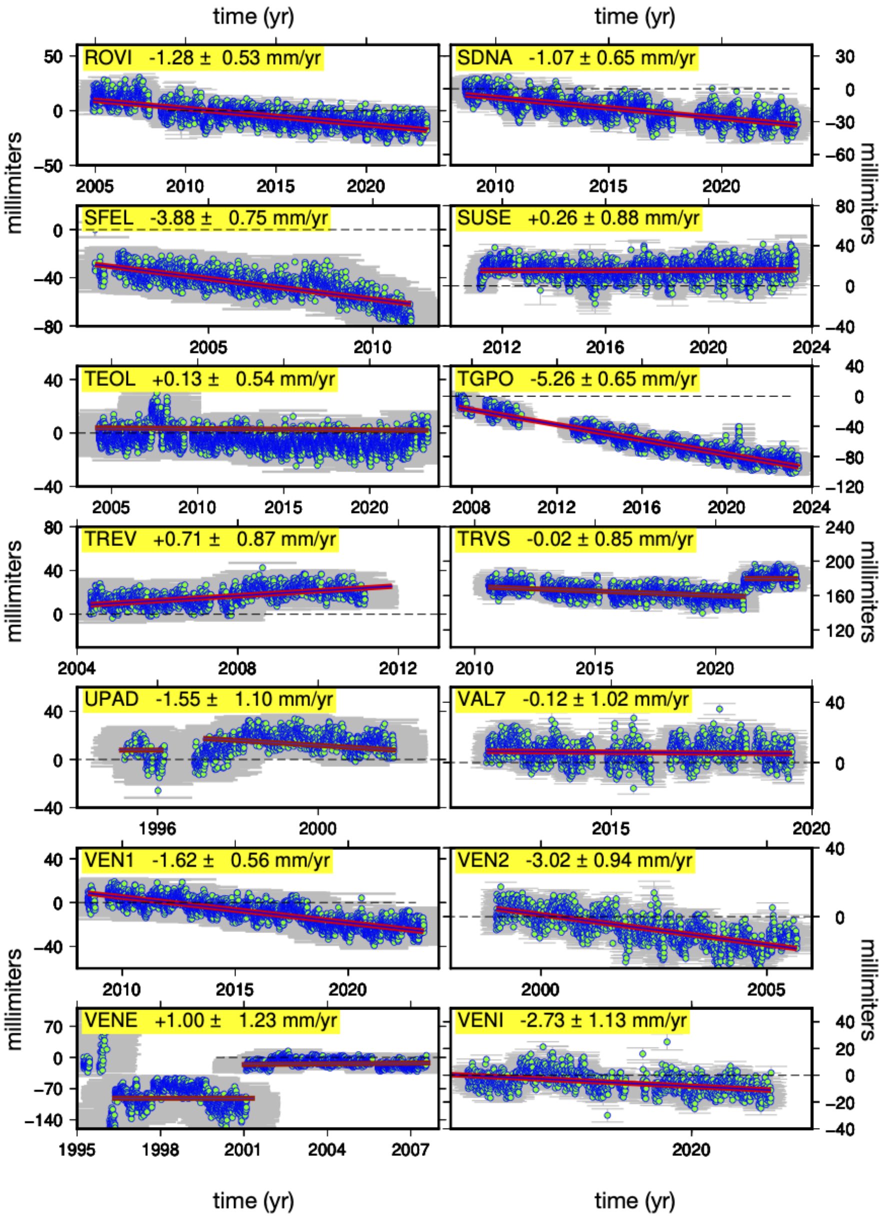

Figure 3.8. GNSS daily time series (up-component). The red line represents the GPS velocity computed by MIDAS [46], and the green solid circles represent the offset daily coordinate time series. Note that both horizontal and vertical axes vary.

ID	**lon** (deg)	**lat** (deg)	**GIA** (mm/yr)	**MIDAS** (mm/yr)
BASS	11.73	45.76	+0.44	$+0.15 \pm 1.36$
CAFV	11.93	45.67	+0.43	-1.28 ± 0.73
CAVA	12.58	45.47	+0.37	-2.54 ± 0.71
CGIA	12.26	45.20	+0.33	-1.84 ± 0.77
CITT	11.79	45.63	+0.43	-1.19 ± 0.72
CODI	12.11	44.83	+0.26	-3.23 ± 0.65
CODR	12.97	45.95	+0.41	-0.52 ± 0.53
FER1	11.60	44.82	+0.26	-0.60 ± 0.69
FERA	11.62	44.81	+0.26	-2.99 ± 0.83
GARI	12.24	44.67	+0.22	-3.27 ± 0.63
GRDO	13.38	45.68	+0.35	-2.76 ± 1.00
LERO	11.95	45.34	+0.37	-1.38 ± 0.84
MDEA	13.43	45.92	+0.38	-0.43 ± 0.49
MEDI	11.64	44.52	+0.19	-1.79 ± 0.49
MGRD	12.01	45.97	+0.46	$+0.53 \pm 0.57$
MST1	12.23	45.49	+0.38	-5.75 ± 2.54
MT01	12.20	45.74	+0.42	-0.19 ± 0.61
MT06	12.13	45.83	+0.44	$+0.29 \pm 1.04$
MT10	11.89	45.88	+0.45	$+0.68 \pm 0.87$
NOVE	12.58	45.66	+0.39	-3.02 ± 0.60
ODEZ	12.48	45.78	+0.41	-1.49 ± 0.70
PADO	11.89	45.41	+0.38	-1.06 ± 0.53

Table 3.1. Vertical velocities estimated with the MIDAS algorithm at the 45 GNSS sites considered in this study and corresponding modeled vertical velocities according to the combined effect of the ICE-7G_NA (VM7) and iALP models.

ID	**lon**	**lat**	**GIA**	**MIDAS**
	(deg)	(deg)	(mm/yr)	(mm/yr)
PAZO	13.05	45.80	+0.38	-0.87 ± 0.56
PORD	12.66	45.95	+0.42	-0.02 ± 0.53
PORT	12.83	45.76	+0.40	-4.12 ± 0.75
PSAL	12.33	45.43	+0.37	-1.11 ± 0.78
PTO1	12.33	44.95	+0.28	-5.15 ± 0.76
REBO	12.03	45.19	+0.34	-0.66 ± 0.85
ROVI	11.78	45.08	+0.32	-1.28 ± 0.53
SDNA	12.56	45.63	+0.38	-1.07 ± 0.65
SFEL	12.29	45.23	+0.34	-3.88 ± 0.75
SUSE	12.20	45.85	+0.44	-0.26 ± 0.88
TEOL	11.67	45.34	+0.37	-0.13 ± 0.54
TGPO	12.22	45.00	+0.29	-5.26 ± 0.65
TREV	12.25	45.66	+0.41	$+0.71 \pm 0.87$
TRVS	12.22	45.68	+0.42	-0.02 ± 0.85
UPAD	11.87	45.40	+0.38	-1.55 ± 1.10
VAL7	11.99	45.89	+0.45	-0.12 ± 1.02
VEN1	12.35	45.43	+0.37	-1.62 ± 0.56
VEN2	12.35	45.43	+0.37	-3.02 ± 0.94
VENE	12.33	45.43	+0.37	-1.00 ± 1.23
VENI	12.38	45.42	+0.36	-2.73 ± 1.13
VICE	11.55	45.56	+0.42	-0.47 ± 0.59
VITT	12.30	45.99	+0.45	$+0.23 \pm 0.77$
VOLT	11.91	45.38	+0.38	$+0.97 \pm 0.76$

Table 3.2. Vertical velocities estimated with the MIDAS algorithm at the 45 GNSS sites considered in this study and corresponding modeled vertical velocities according to the combined effect of the ICE-7G_NA (VM7) and iALP models.

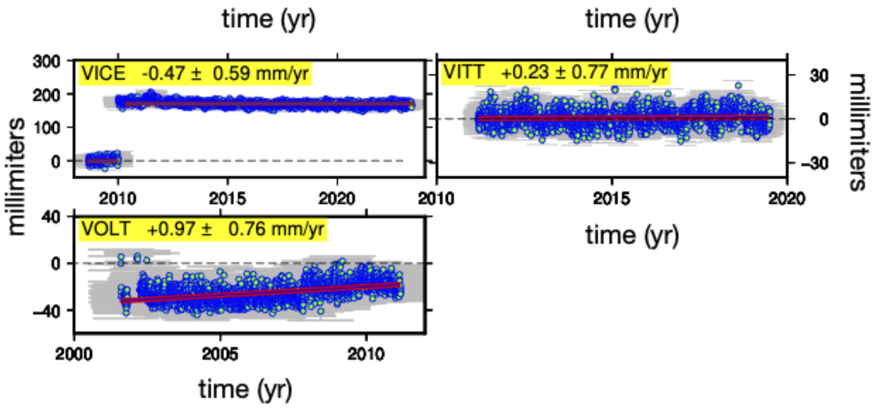

Figure 3.9. GNSS daily time series (up-component). The red line represents the GPS velocity computed by MIDAS [46], and the green solid circles represent the offset daily coordinate time series. Please note that both horizontal and vertical axes are different.

located in the far field of the study region, and *ii)* the contribution stemming from the melting of the Alpine ice sheets during the last glacial cycle.

3.3.1 GIA in response to the melting of far field ice sheets

To model the effects of GIA in the NE Adriatic sea following the melting of far-field ice sheets, I obtained a numerical solution of the Sea Level Equation (SLE), the integral equation describing the interactions between the solid Earth, the oceans and the cryosphere in response to the evolution of surface ice loads and described in the previous Chapter 2. Originally formulated by [56], the SLE accounts for deformational, gravitational and rotational effects induced by spatio-temporal variations of the ice and the meltwater loads [38, 57].

In its simplest form, the SLE reads $S(\theta, \lambda, t) = N - U$, where S is the sea-level variation relative to the solid Earth, N is the sea-surface variation (absolute sea-level change) and U is the vertical displacement of the bedrock.

The three fields, S, U and N, depend upon the location on the Earth surface (colatitude θ and longitude λ) and on time t. As discussed by [18], N and U also implicitly depend upon S, making the SLE an integral equation that can be only solved through numerical iterative methods. Non-linear effects in the SLE arise because of the migration of the shorelines in response to GIA, and because of the transition between grounded and marine-based ice that occurred during deglaciation. As a consequence of the SLE, the rate of sea-level change $\dot{S}$, the vertical velocity $\dot{U}$ and the rate of change of absolute sea-level $\dot{N}$ are related by $\dot{S} = \dot{N} - \dot{U}$, regardless the particular combination of rheology and ice model employed, the Earth's rotation effects are take into account [58].

In this thesis work, we employ the ICE-7G_NA (VM7) GIA model, the latest iteration of the ICE-X suite of global models developed by WR Peltier and collaborators [15, 16]. The model describes the spatio-temporal evolution of ice sheets starting from 26 kyrs BP, assuming a spherically symmetric Earth with Maxwell viscoelastic rheology. We implemented the ICE-7G_NA model into the SELEN[4] open-source SLE solver [18, 59] by converting the geographical grids available on the home page of WR Peltier into a set of disc-shaped, axisymmetric elements, arranged according to the equal-area icosahedron grid by [60], and assigning a piece-wise constant time history to each element. The SELEN[4] solver has been configured to perform three external iterations in which the evolution of paleo-topography is progressively refined and three internal iterations in which the SLE is numerically solved for a given paleo-topography configuration; for further details about the SLE solution scheme, the reader is referred to [18] and its supplementary material. All the computations are carried out up to harmonic degree $l_{max} = 128$, which by the Jeans' rule corresponds to a minimum wavelength of about 312 km on the surface of the Earth, and employing a resolution parameter R = 100 that corresponds to a global icosahedral grid with a pixel size of about 40 km (for details, see [18] and it's supplement). This choice of resolution parameters provides an adequate representation of the spatial variability in the far field of late Pleistocene ice sheets, while ensuring a reasonable trade-off between model resolution and computational costs. Present-day topography has been assigned to the icosahederal grid by averaging the bedrock version of the one arc-minute resolution ETOPO1 global relief [61] over the cell area associated to each pixel. We assume the VM7 rheological profile by [16], which includes a 75 km thick elastic lithosphere, a three-layer upper mantle, a transition zone, a three-layer lower mantle and an inviscid fluid core; the structure of layers and their viscosity values are those listed in Figure 2.2. The rotational feedback on sea-level is taken into account following the revised theory of [62] and [63].

3.3.2 Regional viscoelastic rebound modeling in the Alps

In previous studies about the role of GIA in the Mediterranean region (see *e.g.,* [12]), the time evolution of the Alpine ice sheet has been modeled [64] coarsely, based upon the seminal works of [10] and [65]. Since due its relatively small size no Alpine component is included into the most recent global GIA models as ICE-7G_NA, here we rely upon the high-resolution reconstruction of the Alpine ice sheet during the past glacial cycle proposed by [17], which will be referred to as iALP model in the following. This model, based on numerical simulations forced by the GRIP palaeo-temperature records in the alpine region from the Greenland Ice Core Project [66], provides the ice thickness distribution during the last 120 kyrs BP on a grid with a horizontal spacing of 2 km; a few snapshots of the iALP ice chronology are shown in Figure 3.10.

The ice chronology proposed by [17], given on a regular cartesian grid, has been converted into disc-shaped axisymmetric elements suitable for use with the TABOO open source post-glacial rebound simulator [67] and briefly introduced in the Section 2.3.3, by assigning to each disc element an ice height time history obtained as the average over all the grid nodes falling within the disc area. For consistency, the rheological model follows the VM7 viscosity profile by [16] (see Section 2.1.2), the same adopted to simulate the effects of the far-field ice sheets, described in Section 3.3.1. The size of the discs is 0.5°, sufficient to capture the main features of model iALP. Furthermore, it has been verified that a higher resolution would essentially provide the same results, due to the strong low-pass filter effect that is exerted by the elastic lithosphere and to the fact that possible artifacts due to the discretization of the load would only affect predicted observables at distances from the load comparable to the size of the disc [3].

I remark that while the effect of global GIA is obtained by means of a gravitationally and topographically self-consistent solution of the SLE, the regional effects due to the melting of the Würm Alpine ice sheet have been modeled adopting a simplified approach in which the geoid term is neglected and the approximation $\dot{S} \simeq -\dot{U}$ is assumed. As discussed by [68], [11] and [3] this approximation is valid in the vicinity to the previously glaciated regions, and allows for a simplified evaluation of sea-level change in response to the melting of small ice sheets.

3.4 Results

In this section, I discuss the numerical results obtained by means of the GIA models described in Section 3.3, focusing on the present-day effects on the rates of relative sea-level change ($\dot{S}$), of vertical land motion ($\dot{U}$) and of absolute sea-level change ($\dot{N}$). These fields are sometimes referred to as GIA fingerprints [38, 69] (see Section 1.2, and their spatial variability reflects the global effects of deformation, gravitational attraction, and rotation within the system composed by the solid Earth, the oceans, and the ice sheets [3, 7, 18, 39, 70].

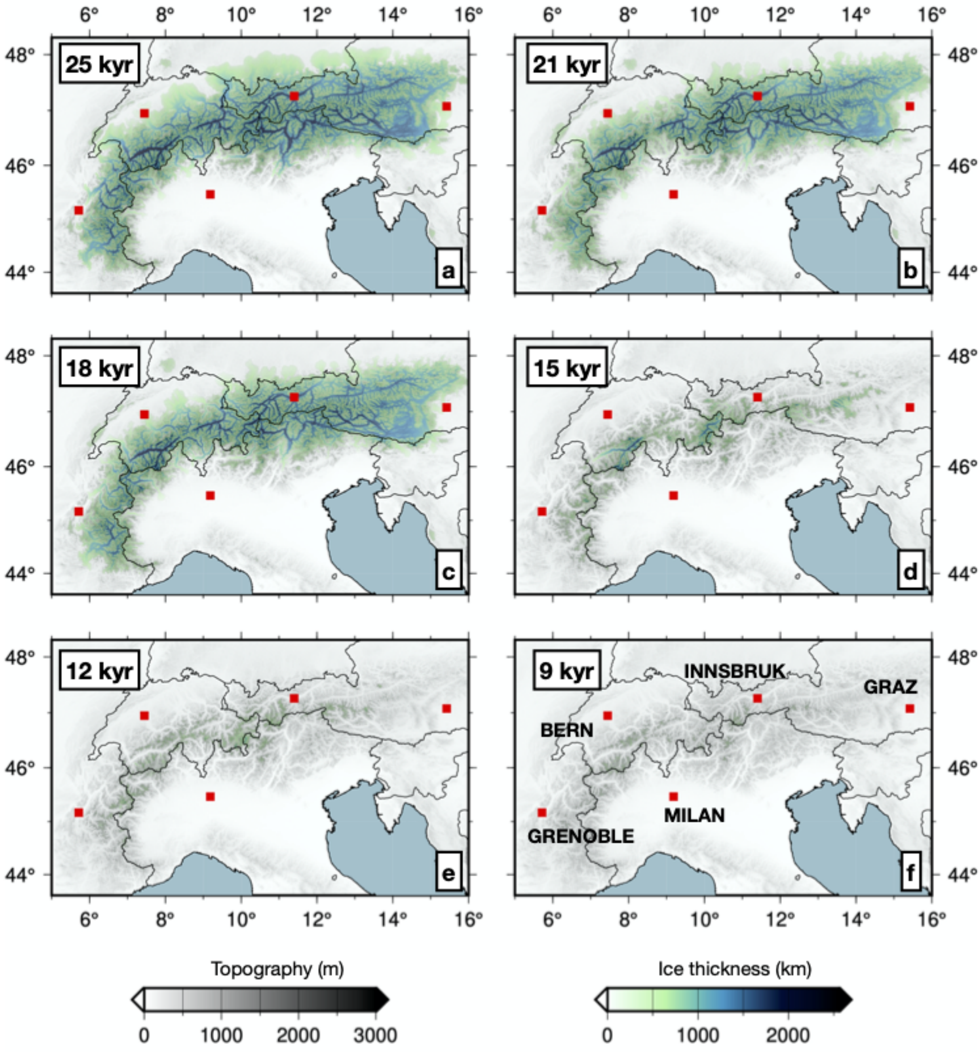

Figure 3.10. Ice thickness and extents of the Alpine ice sheet by [17], at 26 (a), 21 (b), 18 (c), 15 (d), 12 (e) and 9 kyr BP (f). Red squares indicate the location of major cities [3].

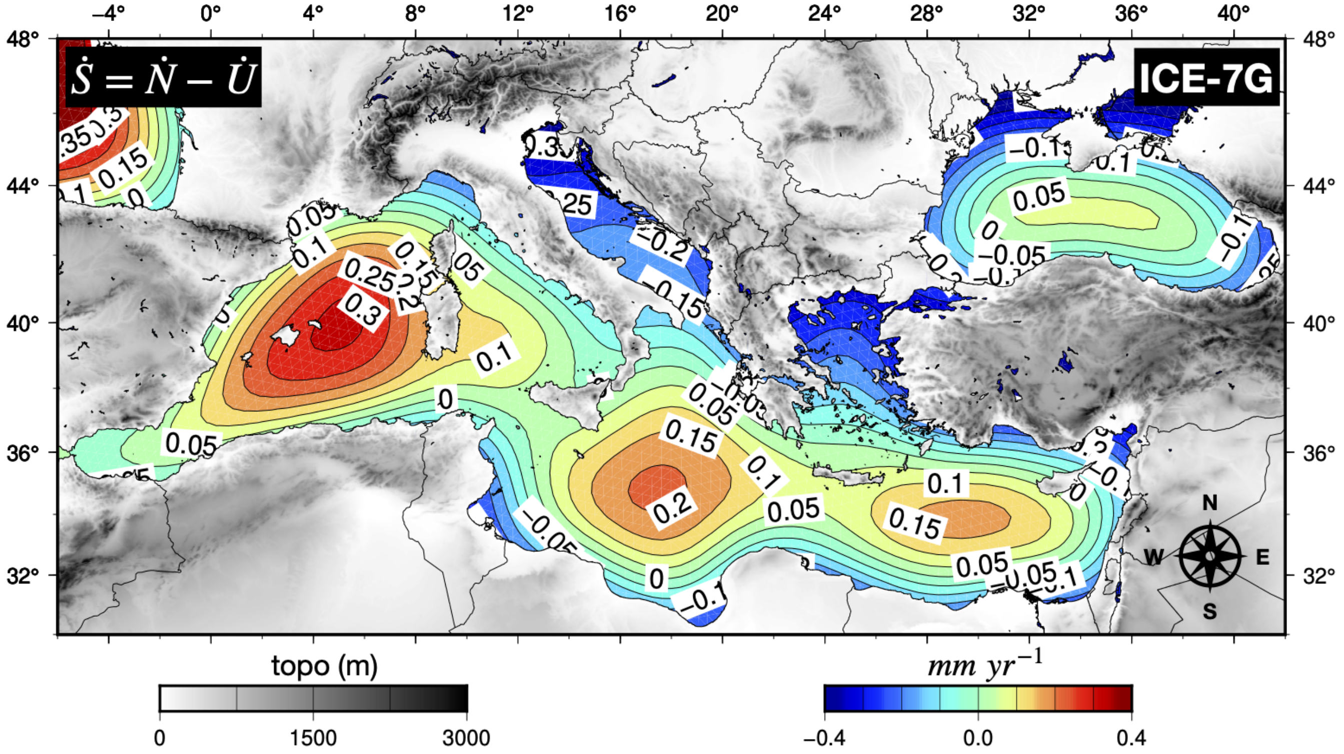

Figure 3.11. Predicted rate of present-day sea-level change $\dot{S}$ induced by GIA across the Mediterranean region, according to model ICE-7G_NA (VM7). Numerical results have been obtained using the SELEN^4 SLE solver.

3.4.1 Sea-level change

Figure 3.11 shows the present-day rate of sea-level change $\dot{S}$ across the Mediterranean basin according to the ICE-7G_NA (VM7) GIA model. If GIA from the melting of past ice sheets was the unique cause of contemporary sea-level change, those rates would directly manifest as long term sea-level trends at tide gauges. Since GIA evolves on the time scales of millennia, the trends are nearly constant on periods of decades or centuries (*e.g.,* [3, 38]).

The pattern in Figure 3.11, whose general features are well known from previous studies of GIA, has been recently reconsidered and discussed by [9]. The expected maximum rates occur at the center of the sub-basins, with values of $\dot{S}$ up to ~ 0.3 mm/yr in the Balearic Sea, up to ~ 0.2 mm/yr in the Ionian and in the Levantine Sea, and up to ~ 0.05 mm/yr in the Black Sea. As pointed out by [9], these rates constitute a significant fraction of the trends observed at tide gauges facing these sub-basins. The spatial variability of $\dot{S}$ across the Mediterranean is explained in terms of the ongoing flexure of the lithosphere induced by the melt-water loading, causing a sea-level rise relative to the seafloor. Predicted $\dot{S}$ values decrease and vanish along the southern coasts of the Mediterranean between Algeria, Tunisia, Libya and south Israel. Remarkably, in the Adriatic Sea $\dot{S}$ changes its sign and a sea-level fall ($\dot{S} < 0$) is expected due to GIA, with rates between -0.34 and -0.38 mm/yr in the Adriatic Sea facing the Venetian Lagoon. A similar pattern is observed in other narrow coastal inlets, as discussed by [9] and [3]. It should be noted that the rates in Figure 3.11 are significantly different from those obtained by [5], based upon the ICE-3G(VM1) GIA model [71]. This confirms that GIA predictions are not given once for all, but they evolve according to improvements in the knowledge about the chronology of the late-Pleistocene ice sheets and on the mantle viscosity profile, and steps forwards in the numerical techniques employed to solve the SLE (see, *e.g.*, [9, 38]).

Figure 3.12 shows the contributions of the ICE-7G_NA (VM7) and iALP models to $\dot{S}$ and $\dot{U}$ GIA fingerprints in the Venice Lagoon, as well as the cumulative effect of the two models. When only the melting of remote ice sheets is considered (Figure 3.12a), $\dot{S}$ varies, in the study area, between -0.38 mm/yr (Venezia and Trieste) to -0.29 mm/yr (Rimini) and goes further down to -0.22 mm/yr south of Ancona. These rates are different with respect to previous results by [58], who obtained positive $\dot{S}$ values across the Mediterranean region. This is to be attributed to the different GIA model assumed by [58], who employed ICE-5G(VM2) by [72], and to the higher spatial resolution of our numerical solution of the SLE adopted in the present study.

The melting of the Alpine glacier (Figure 3.12c) is also responsible for a sea-level fall across the northern Adriatic region, albeit of slightly smaller amplitude with respect to that due to global GIA. Modeled rates of sea-level change decrease from north to south, from about -0.30 mm/yr (Venezia and Trieste) to about -0.12 mm/yr (Rimini and Pula) and reach zero south of Ancona. Therefore, the melting of the Würm Alpine ice sheet further enhances

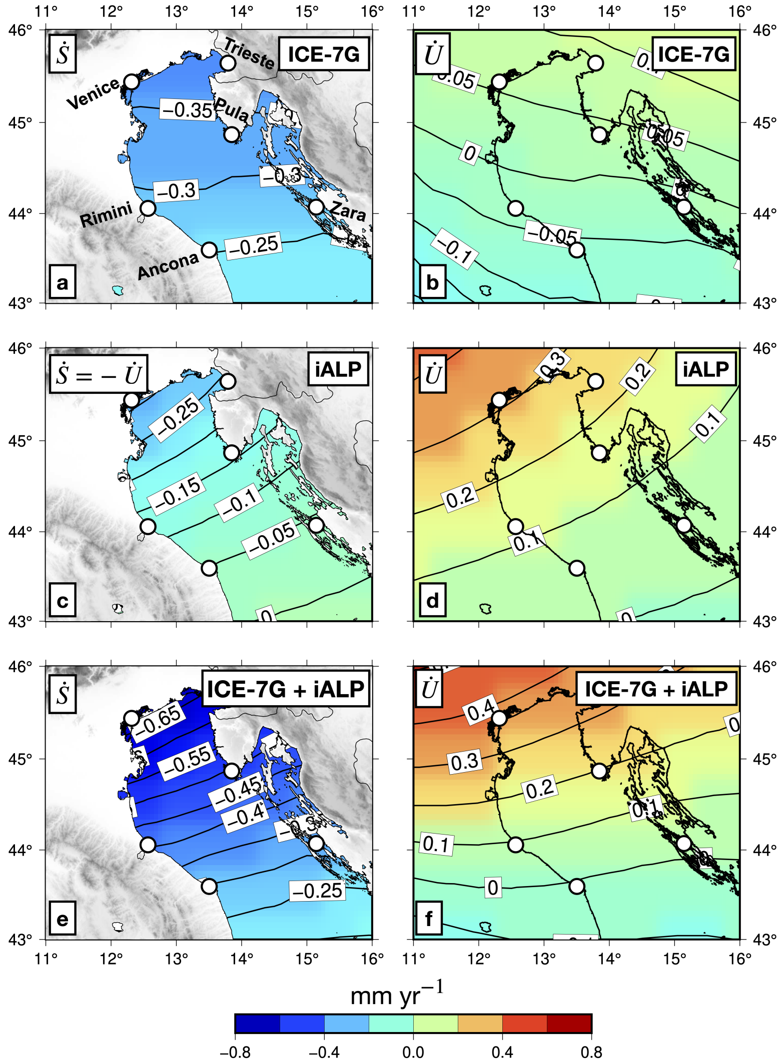

Figure 3.12. Modeled GIA fingerprints $\dot{S}$ (left frames) and $\dot{U}$ (right) in the Northern Adriatic. Top frames (a-b) show predictions according to the global GIA model ICE-7G_NA (VM7), middle frames (c-d) those obtained with the iALP regional GIA model, and bottom frames (e-f) the total effect due to the ICE-7G_NA (VM7) and iALP GIA models. Results shown in frames (a) and (b) have been obtained using the SELEN[4] SLE solver, while those in frames (c) and (d) have been computed with the TABOO code.

the sea-level fall associated to continental levering due to the melting of remote ice sheets. Indeed, the cumulated effect of the ICE-7G_NA (VM7) and iALP models, shown in Figure 3.12e, is a general sea-level fall in the study area, with $\dot{S}$ values ranging from about -0.7 mm/yr (Venezia and Trieste) to about -0.3 mm/yr (Rimini), and reach the -0.2 mm/yr level south of Ancona, where only the contribution due to global GIA is significant due to the large distance from the Alps. Therefore, it is clear that taking into account the iALP model is essential for a careful reconstruction of the GIA-driven sea-level change in the Venetian Lagoon region.

It is of particular importance here to compare modeled estimates for the GIA contribution to the rate of sea-level change with the observed rates that I discussed in Section 3.2.1. For Venezia Punta della Salute, the longest-spanning (1909-2000) tide gauge record among those available in the PSMSL database, the observed rate is (2.4 ± 0.2) mm/yr. Taking into account that the GIA-induced sea-level fall at this site is of about -0.7 mm/yr, resulting from the combined effect of near-field and remote ice sheets, we would obtain a GIA-corrected rate of sea-level rise of about 3.1 mm/yr. The contribution of GIA to sea-level change is even more important at Trieste, where a smaller rate of (1.2 ± 0.1) mm/yr is observed; taking GIA into account, we would obtain a corrected rate of about 1.9 mm/yr. Modeling the effect of GIA is therefore important for a correct interpretation of the various factors that are contributing to contemporary sea-level change in the Northern Adriatic and in the Venetian Lagoon.

3.4.2 Vertical land motion

In Figure 3.12b are shown the predicted vertical velocity $\dot{U}$ according to the GIA model ICE-7G_NA (VM7). The GIA fingerprint $\dot{U}$ represents the present-day rate of vertical land motion that would be observed, at a given location, by an earthbound GNSS receiver. In the Venetian Lagoon, predicted uplift rates for ICE-7G_NA (VM7) are in the range between 0.05 and 0.10 mm/yr, slightly different than those obtained by [5] and [58], based on models ICE-3G (VM1) and ICE-5G (VM2), respectively. Moving southward, vertical velocities predicted by ICE-7G_NA (VM7) decrease and turn into a subsidence with rates of -0.05 mm/yr between Rimini and Zara and -0.10 mm/yr south of Ancona. We point out that ICE-7G_NA (VM7) predicts a relative sea-level *fall* (Figure 3.12a) even in the subsiding region of the study area (Figure 3.12b). This apparent paradox is allowed by the SLE since the relationship $\dot{S} = \dot{N} - \dot{U}$ holds true (see [39]), and therefore the conditions $\dot{S} < 0$ and $\dot{U} < 0$ can be simultaneously verified for suitable values of the rate of absolute sea-level change $\dot{N}$.

Figure 3.12d shows the modeled vertical velocities due to the melting of the Würm Alpine glaciers. Over the northern Adriatic Sea these rates largely exceed those due to global GIA and therefore represent the dominant contribution to GIA-induced vertical land motion in the study area. Indeed, model iALP predicts uplift rates $\dot{U}$ around 0.3 mm/yr in the Venetian Lagoon and in the range between 0.2 and 0.1 mm/yr across the most part of the northern

Adriatic (Rimini and Pula). The uplift velocities rapidly decay when moving southward, as the distance from the former ice load increases, with rates reaching zero south of Ancona.

The total effect of ICE-7G_NA (VM7) and iALP on the predicted present-day vertical velocity $\dot{U}$ is shown in Figure 3.12f. The rate of vertical land motion varies between 0.4 mm/yr (Venezia and Trieste) to 0.2 and 0.1 mm/yr (Rimini and Pula) and reaches zero south of Ancona, turning to a subsidence in the southern part of Adriatic Sea. The pattern of vertical land motion in the study area is largely dominated by the contribution of iALP, confirming the importance of taking into account the melting of the Würm Alpine glaciers to model GIA effects on geodetic observables in the region [3].

Table 3.1 and Table 3.2 lists modeled vertical velocities at the 45 GNSS sites considered in this study due to the combined GIA effect of the ICE-7G_NA (VM7) and iALP models. Rates of vertical land motion due to GIA are generally smaller than the uncertainties associated to the MIDAS estimate of the observed velocity. However, the impact of GIA on observed velocities is generally not negligible; indeed, the average GIA-induced rate of vertical land motion over the 45 considered GNSS sites is +0.37 mm/yr, representing about 28% of the average vertical velocity (−1.35 mm/yr) of the GNSS sites listed in Table 3.1 and Table 3.2. Only at sites where the largest subsidence rates are recorded (*e.g.* MST1, TGPO and PTO1), GIA-induced rates represent a second-order contribution to present-day land movements.

3.4.3 Absolute sea-level

The last GIA fingerprint considered is $\dot{N}$, the present-day rate of change of the sea surface height (or absolute sea-level). If only GIA was contributing to contemporary sea-level change, $\dot{N}$ would be directly observed by satellite altimetry [33, 73]. As discussed in Section 3.3.1, the $\dot{N}$ fingerprint is related to $\dot{S}$ and $\dot{U}$ by $\dot{S} = \dot{N} - \dot{U}$. Figure 3.13 shows the rate of sea surface height $\dot{N}$ due to global GIA, according to the ICE-7G_NA (VM7) model. The spatial pattern of $\dot{N}$ is characterized by a much smoother variability when compared with $\dot{S}$ and $\dot{U}$ [58]. Its amplitude is close to -0.3 mm/yr, the global ocean average of $\dot{N}$ often adopted as a rule of thumb in satellite altimetry [38, 74]. It is not possible to estimate an $\dot{N}$ GIA fingerprint for model iALP since, as discussed in Section 3.3.2, I am neglecting the geoid term in our approach to regional GIA modeling. In the northern Adriatic and in the Venetian Lagoon, as discussed in Section 3.2.1, satellite altimetry hints to a sea surface rise between +4 and +6 mm/yr, a range that lies above the global mean of +3 mm/yr during the “altimetry era”. These rates are only marginally affected by GIA, which induces a sea surface fall of about -0.3 mm/yr, approximately uniform throughout the region.

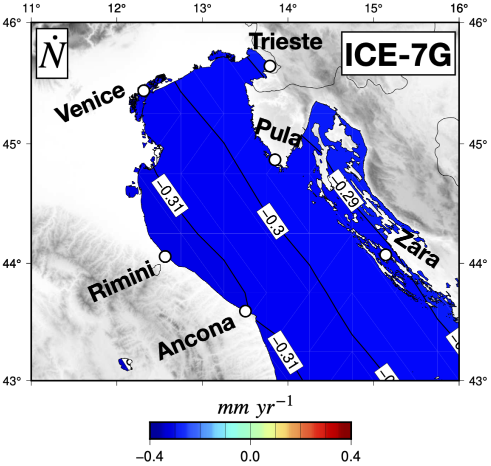

Figure 3.13. Predicted rate of present-day rate of change of the sea surface height $\dot{N}$ in the north Adriatic sea, according to model ICE-7G_NA (VM7). The computation have been performed using program SELEN[4].

3.5 Discussion

Studying sea-level change and vertical land motions in the northern Adriatic Sea, and in particular in the Venetian Lagoon, is of paramount importance in view of the highly vulnerable coastal environments. Accurate modeling of the impact of GIA on these observables is a key factor to allow the identification of the various geophysical contributions which are driving the measured rates.

In Section 3.4, it has been shown that the pattern of present-day GIA-induced rates of sea-level change in the Mediterranean is characterized by positive values in the bulk of the basin, with peak values of $\dot{S}$ of about 0.3 mm/yr, due to the sea floor subsidence associated to the melt-water load [6, 70]. On the contrary, in the northern Adriatic Sea, our global GIA model predicts a sea-level fall with rates between −0.38 mm/yr (Venice and Trieste) and −0.26 mm/yr (Ancona). As discussed in detail by [9], negative values of $\dot{S}$ are common in narrow sub-basins, where the coastal profiles are characterized by a short radius of curvature, and can be explained in terms of continental levering (see, *e.g.*, [70]).

The vertical velocity field induced by the ongoing effects of global GIA is characterized by a tilting pattern, with the northern coast of the Adriatic (between Venezia and Trieste) uplifting with rates between 0.05 and 0.10 mm/yr, while the southern part of the study area (south of Ancona) is subsiding at a rate of about −0.1 mm/yr. If we take into account the contributions from both global and regional GIA, our model predicts a widespread sea-level fall in the northern Adriatic, with rates decreasing southward from −0.7 mm/yr between Venezia and Trieste to −0.2 mm/yr south of Ancona, and an uplift field with vertical velocities of about 0.4 mm/yr on the northern margin of the basin, which decrease southward reaching the zero level at Ancona.

Sea-level rise and vertical land motion in the northern Adriatic is the result of a wide range of geophysical, geological and anthropogenic effects. As shown, modeling GIA effects in the region is of key importance to correctly identify the drivers of observed sea-level rise and to interpret measured velocities at GNSS stations. For an accurate GIA modeling, the isostatic response to the melting of the Alpine Würm ice sheet needs to be taken into account. Of course, GIA models are not given once and for all and further elements need to be included in the future. For instance, due to lateral variations in the rheological properties of the Earth, GIA is a fully 3-D global problem; this is especially true in regions like the Mediterranean basin, characterized by structural heterogeneities due to its complex geodynamical setting [75]. Furthermore, as pointed out in the seminal work by [76], the Alps structure at depth shows significant differences between the western and eastern sections of the arc, possibly reflecting a difference in past subduction of the Tethyan lithosphere and subsequent continental collision. In this respect, a fully 3-D regional GIA model may possibly explain, at least in part, the horizontal gradients in vertical geodetic velocities and sea-level rates in the Northern Adriatic. However, the computational complexity of a 3-D numerical approach to the GIA problem is such that only few attempts to 3-D GIA models have been discussed in literature (see, *e.g.* [77]). Moreover, uncertainties on the details of the ice load evolution also affect GIA predictions [78]. In this respect, uplift estimates from GIA models in the Alpine region in the presence of lateral rheological variations are still a matter of discussion.

3.6 Conclusions

In this work, it was obtained an up-to-date, high-resolution estimate of sea-level change and vertical deformation at the Mediterranean scale, based upon the ICE-7G_NA (VM7) GIA model of [14] and a reconstruction of the time evolution of the Alpine ice sheet during the last glacial phase obtained by [17]. To estimate present-day geodetic fingerprints, it was combined an high resolution, global solution of the SLE describing the topographically and gravitationally self-consistent response to the melting of late-Pleistocene ice complexes with an approximated approach suitable for modeling the regional-scale effects associated with the Alpine ice sheet. Indeed, due to its proximity to the Alpine arc, the northern Adriatic region is expected to be significantly affected by near-field isostatic effects associated with the melting of the Alpine Würm ice sheet. These results suggest that regional GIA in response to the melting of near-field ice sheets further enhances the sea-level fall associated with global GIA, and represents the dominant GIA contribution to vertical land motion in the northern Adriatic with uplift rates up to 0.3 mm/yr on the coast between Venezia and Trieste.

By comparing vertical velocities provided by our GIA model with observed rates at GNSS sites, it was found that GIA effects are a marginal contribution to geodetic velocity only at sites where the largest subsidence is recorded. Conversely, at the majority of GNSS sites, GIA may represent a significant contribution to observed rates and shall be taken into account for a correct interpretation of the velocity field. Similarly, GIA-driven sea-level change represents a fraction of the observed rates of sea-level ranging from 30% in the Venetian Lagoon to over 50% at Trieste, and it significantly mitigates sea-level rise due to present-day climate change, to the natural compaction of recent fine-grained alluvial deposits and to anthropic activities like the extraction of underground fluids.

GIA models are constantly evolving as knowledge about the spatio-temporal evolution of late-Pleistocene ice sheets and on the mantle viscosity improves, and as new numerical techniques are developed. The Mediterranean region is characterized by a complex geodynamical setting, and structural heterogeneities beneath the Alpine arc are well known from tomographic evidences. A next generation of GIA models, based on a fully 3-D numerical approach to the GIA problem, will allow a more accurate modeling of GIA fingerprints.

In the next chapter of this thesis I will present a work that was carried out during the third year of PhD and which was presented at various national and international conferences (see Appendix B). I will investigate on lateral strength variations of the lithosphere in the Graham Land (Antarctica Peninsula). This work could be fundamental for the next generation of GIA models since, as already mentioned above, it is the strength and rheology of the lithosphere that controls its deformation; hence, a proper understanding of these properties is essential if the consequences of any such deformation are to be predicted.

Bibliography

[1] Paolo Gatto and Laura Carbognin, "The Lagoon of Venice: natural environmental trend and man-induced modification/La Lagune de Venise: l'évolution naturelle et les modifications humaines", *Hydrological Sciences Journal*, vol. 26, no. 4, pp. 379–391, 1981.

[2] Antonio Brambati, Laura Carbognin, Tullio Quaia, Pietro Teatini, and Luigi Tosi, "The Lagoon of Venice: geological setting, evolution and land subsidence", *Episodes*, vol. 26, no. 3, pp. 264–268, 2003.

[3] Fernando Linsalata, Daniele Melini, and Giorgio Spada, "Glacial isostatic adjustment in the northern adriatic region: estimates of the contribution from the alpine ice sheet", *Geophysical Journal International*, vol. 233, no. 3, pp. 2039–2052, 2023.

[4] Davide Zanchettin, Sara Bruni, Fabio Raicich, Piero Lionello, Fanny Adloff, Alexey Androsov, Fabrizio Antonioli, Vincenzo Artale, Eugenio Carminati, Christian Ferrarin, et al., "Sea-level rise in Venice: historic and future trends", *Natural Hazards and Earth System Sciences*, vol. 21,

no. 8, pp. 2643–2678, 2021.

[5] Eugenio Carminati and Ginevra Di Donato, "Separating natural and anthropogenic vertical movements in fast subsiding areas: the Po plain (N. Italy) case", *Geophysical Research Letters*, vol. 26, no. 15, pp. 2291–2294, 1999.

[6] Paolo Stocchi and Giorgio Spada, "Post-glacial sea-level in the Mediterranean Sea: Clark's zones and role of remote ice sheets", *Ann. Geophys*, vol. 50, no. 6, pp. 741–761, 2007.

[7] A James Clark, William E Farrell, and W Richard Peltier, "Global changes in postglacial sea level: A numerical calculation1", *Quaternary Research*, vol. 9, no. 3, pp. 265–287, 1978.

[8] A James Clark and S Craig Lingle, "Predicted relative sea-level changes (18,000 years BP to present) caused by late-glacial retreat of the Antarctic ice sheet", *Quaternary research*, vol. 11, no. 3, pp. 279–298, 1979.

[9] Giorgio Spada and Daniele Melini, "New estimates of ongoing sea level change and land movements caused by glacial isostatic adjustment in the mediterranean region", *Geophysical Journal International*, vol. 229, no. 2, pp. 984–998, 2022.

[10] H Gudmundur Gudmundsson, "An order-of-magnitude estimate of the current uplift-rates in Switzerland caused by the Würm Alpine deglaciation", *Eclogae Geologicae Helvetiae*, vol. 87, no. 2, pp. 545–557, 1994.

[11] Giorgio Spada, Paolo Stocchi, and Florence Colleoni, “Glacio–isostatic adjustment in the Po plain and in the northern adriatic region”, *Pure and Applied Geophysics*, vol. 166, no. 8, pp. 1303–1318, 2009.

[12] Paolo Stocchi, Giorgio Spada, and Spina Cianetti, “Isostatic rebound following the Alpine deglaciation: impact on the sea level variations and vertical movements in the Mediterranean region”, *Geophysical Journal International*, vol. 162, no. 1, pp. 137–147, 2005.

[13] Kurt Lambeck, Fabrizio Antonioli, M Anzidei, L Ferranti, G Leoni, G Scicchitano, and S Silenzi, “Sea level change along the Italian coast during the Holocene and projections for the future”, *Quaternary International*, vol. 232, no. 1-2, pp. 250–257, 2011.

[14] Keven Roy and W Richard Peltier, “Relative sea level in the Western Mediterranean basin: A regional test of the ICE-7G_NA (VM7) model and a constraint on late Holocene Antarctic deglaciation”, *Quaternary Science Reviews*, vol. 183, pp. 76–87, 2018.

[15] Keven Roy and W Richard Peltier, “Glacial isostatic adjustment, relative sea level history and mantle viscosity: reconciling relative sea level model predictions for the us east coast with geological constraints”, *Geophysical Journal International*, vol. 201, no. 2, pp. 1156–1181, 2015.

[16] Keven Roy and W Richard Peltier, “Space-geodetic and water level gauge constraints on continental uplift and tilting over North America: regional convergence of the ICE-6G_C (VM5a/VM6) models”, *Geophysical Jour-*

nal International, vol. 210, no. 2, pp. 1115–1142, 2017.

[17] Julien Seguinot, Susan Ivy-Ochs, Guillaume Jouvet, Matthias Huss, Martin Funk, and Frank Preusser, "Modelling last glacial cycle ice dynamics in the Alps", *The Cryosphere*, vol. 12, no. 10, pp. 3265–3285, 2018.

[18] Giorgio Spada and Daniele Melini, "SELEN 4 (SELEN version 4.0): a Fortran program for solving the gravitationally and topographically self-consistent sea-level equation in glacial isostatic adjustment modeling", *Geoscientific Model Development*, vol. 12, no. 12, pp. 5055–5075, 2019.

[19] Piero Lionello, Robert J Nicholls, Georg Umgiesser, and Davide Zanchettin, "Venice flooding and sea level: past evolution, present issues, and future projections (introduction to the special issue)", *Natural Hazards and Earth System Science*, vol. 21, no. 8, pp. 2633–2641, 2021.

[20] Kenneth O Emery, DG Aubrey, and V Goldsmith, "Coastal neo-tectonics of the Mediterranean from tide-gauge records", *Marine Geology*, vol. 81, no. 1-4, pp. 41–52, 1988.

[21] Bruce C Douglas, "Global sea level rise", *Journal of Geophysical Research: Oceans*, vol. 96, no. C4, pp. 6981–6992, 1991.

[22] Bruce C Douglas, "Global sea rise: a redetermination", *Surveys in Geophysics*, vol. 18, no. 2, pp. 279–292, 1997.

[23] Michael N Tsimplis and NE Spencer, "Collection and analysis of monthly mean sea level data in the Mediterranean and the Black Sea", *Journal of*

Coastal Research, vol. 13, pp. 534–544, 1997.

[24] Marta Marcos and Michael N Tsimplis, "Coastal sea level trends in Southern Europe", *Geophysical Journal International*, vol. 175, no. 1, pp. 70–82, 2008.

[25] Goran Buble, RA Bennett, and S Hreinsdóttir, "Tide gauge and GPS measurements of crustal motion and sea level rise along the eastern margin of Adria", *Journal of Geophysical Research: Solid Earth*, vol. 115, no. B2, 2010.

[26] Michael N Tsimplis, Fabio Raicich, Luciana Fenoglio-Marc, Andrew GP Shaw, Marta Marcos, Samuel Somot, and Andrea Bergamasco, "Recent developments in understanding sea level rise at the adriatic coasts", *Physics and Chemistry of the Earth, Parts A/B/C*, vol. 40, pp. 59–71, 2012.

[27] Fabio Raicich, "The sea level time series of trieste, molo sartorio, italy (1869–2021)", *Earth System Science Data*, vol. 15, no. 4, pp. 1749–1763, 2023.

[28] Gaia Galassi and Giorgio Spada, "Linear and non-linear sea-level variations in the Adriatic Sea from tide gauge records (1872-2012)", *Annals of Geophysics*, vol. 57, no. 6, 2014.

[29] Marta Marcos and MN Tsimplis, "Variations of the seasonal sea level cycle in southern Europe", *Journal of Geophysical Research: Oceans*,

vol. 112, no. C12, 2007.

[30] Laura Carbognin, Pietro Teatini, Alberto Tomasin, and Luigi Tosi, “Global change and relative sea level rise at Venice: what impact in term of flooding”, *Climate Dynamics*, vol. 35, no. 6, pp. 1039–1047, 2010.

[31] Dario Camuffo and Giovanni Sturaro, “Sixty-cm submersion of Venice discovered thanks to Canaletto’s paintings”, *Climatic Change*, vol. 58, no. 3, pp. 333–343, 2003.

[32] Eric Fouache, Sanja Faivre, J-J Dufaure, V Kovacic, and Francis Tassaux, “New observations on the evolution of the Croatian shoreline between Poreç and Zadar over the past 2000 years”, *Zeitschrift für Geomorphologie. Supplementband*, vol. 122, pp. 33–46, 2000.

[33] Anny Cazenave and William Llovel, “Contemporary sea level rise”, *Annual review of marine science*, vol. 2, pp. 145–173, 2010.

[34] Anny Cazenave, Hindumathi Palanisamy, and Michael Ablain, “Contemporary sea level changes from satellite altimetry: What have we learned? What are the new challenges?”, *Advances in Space Research*, vol. 62, no. 7, pp. 1639–1653, 2018.

[35] Vincent F Rocco, *Sea level trends in the Mediterranean from tide gauges and satellite altimetry*, Ph.D. thesis, Alma Mater Studiorum, University of Bologna, Italy, 2015.

[36] Stefano Vignudelli, Florence Birol, Jérôme Benveniste, Lee-Lueng Fu,

Nicolas Picot, Matthias Raynal, and Hélène Roinard, "Satellite altimetry measurements of sea level in the coastal zone", *Surveys in Geophysics*, vol. 40, no. 6, pp. 1319–1349, 2019.

[37] Jean-François Legeais, Michaël Ablain, Lionel Zawadzki, Hao Zuo, Johnny A Johannessen, Martin G Scharffenberg, Luciana Fenoglio-Marc, M Joana Fernandes, Ole Baltazar Andersen, Sergei Rudenko, et al., "An improved and homogeneous altimeter sea level record from the ESA Climate Change Initiative", *Earth System Science Data*, vol. 10, no. 1, pp. 281–301, 2018.

[38] Giorgio Spada, "Glacial isostatic adjustment and contemporary sea level rise: An overview", *Surveys in Geophysics*, vol. 38, no. 1, pp. 153–185, 2017.

[39] Giorgio Spada and Daniele Melini, "On some properties of the glacial isostatic adjustment fingerprints", *Water*, vol. 11, no. 9, pp. 1844, 2019.

[40] Laura Carbognin, P Teatini, and L Tosi, "The impact of relative sea level rise on the Northern Adriatic Sea coast, Italy", *WIT Transactions on Ecology and the Environment*, vol. 127, pp. 137–148, 2009.

[41] L James Davis, RA Bennett, and BP Wernicke, "Assessment of GPS velocity accuracy for the Basin and Range Geodetic Network (BARGEN)", *Geophysical Research Letters*, vol. 30, no. 7, 2003.

[42] Corné Kreemer, William C Hammond, and Geoffrey Blewitt, "A robust

estimation of the 3-D intraplate deformation of the North American plate from GPS", *Journal of Geophysical Research: Solid Earth*, vol. 123, no. 5, pp. 4388–4412, 2018.

[43] Corné Kreemer and Geoffrey Blewitt, "Robust estimation of spatially varying common-mode components in GPS time-series", *Journal of Geodesy*, vol. 95, no. 1, pp. 1–19, 2021.

[44] Alexandre Michel, Alvaro Santamaría-Gómez, Jean-Paul Boy, Félix Perosanz, and Sylvain Loyer, "Analysis of GNSS displacements in Europe and their comparison with hydrological loading models", *Remote Sensing*, vol. 13, no. 22, pp. 4523, 2021.

[45] Geoffrey Blewitt and David Lavallée, "Effect of annual signals on geodetic velocity", *Journal of Geophysical Research: Solid Earth*, vol. 107, no. B7, pp. ETG–9, 2002.

[46] Geoffrey Blewitt, Corné Kreemer, William C Hammond, and Julien Gazeaux, "MIDAS robust trend estimator for accurate GPS station velocities without step detection", *Journal of Geophysical Research: Solid Earth*, vol. 121, no. 3, pp. 2054–2068, 2016.

[47] Henri Theil, "A rank-invariant method of linear and polynomial regression analysis", *Indagationes mathematicae*, vol. 12, no. 85, pp. 173, 1950.

[48] P Kumar Sen, "Estimates of the regression coefficient based on Kendall's tau", *Journal of the American statistical association*, vol. 63, no. 324, pp.

1379–1389, 1968.

[49] C William Hammond, Geoffrey Blewitt, and Corné Kreemer, “GPS imaging of vertical land motion in California and Nevada: Implications for Sierra Nevada uplift”, *Journal of Geophysical Research: Solid Earth*, vol. 121, no. 10, pp. 7681–7703, 2016.

[50] Corné Kreemer and Ilya Zaliapin, “Spatiotemporal correlation between seasonal variations in seismicity and horizontal dilatational strain in California”, *Geophysical Research Letters*, vol. 45, no. 18, pp. 9559–9568, 2018.

[51] Lambert Caron, ER Ivins, E Larour, S Adhikari, J Nilsson, and G Blewitt, “GIA model statistics for GRACE hydrology, cryosphere, and ocean science”, *Geophysical Research Letters*, vol. 45, no. 5, pp. 2203–2212, 2018.

[52] Chen Yu, Zhenhong Li, Nigel T Penna, and Paola Crippa, “Generic atmospheric correction model for interferometric synthetic aperture radar observations”, *Journal of Geophysical Research: Solid Earth*, vol. 123, no. 10, pp. 9202–9222, 2018.

[53] A Oluwaseun Ojo, Honn Kao, Yan Jiang, Michael Craymer, and Joseph Henton, “Strain accumulation and release rate in Canada: implications for long-term crustal deformation and earthquake hazards”, *Journal of Geophysical Research: Solid Earth*, vol. 126, no. 4, pp. e2020JB020529, 2021.

[54] K Dennis Murray, MH Murray, and AF Sheehan, “Active deformation near the Rio Grande Rift and Colorado Plateau as inferred from continuous Global Positioning System measurements”, *Journal of Geophysical Research: Solid Earth*, vol. 124, no. 2, pp. 2166–2183, 2019.

[55] Paul Wessel and Walter HF Smith, “New, improved version of generic mapping tools released”, *Eos, Transactions American Geophysical Union*, vol. 79, no. 47, pp. 579–579, 1998.

[56] E William Farrell and A James Clark, “On postglacial sea level”, *Geophysical Journal International*, vol. 46, no. 3, pp. 647–667, 1976.

[57] Pippa Whitehouse, “Glacial isostatic adjustment modelling: historical perspectives, recent advances, and future directions”, *Earth surface dynamics*, vol. 6, no. 2, pp. 401–429, 2018.

[58] Paolo Stocchi and Giorgio Spada, “Influence of glacial isostatic adjustment upon current sea level variations in the Mediterranean”, *Tectonophysics*, vol. 474, no. 1-2, pp. 56–68, 2009.

[59] Giorgio Spada and Paolo Stocchi, “SELEN: A Fortran 90 program for solving the “sea-level equation””, *Computers & Geosciences*, vol. 33, no. 4, pp. 538–562, 2007.

[60] Max Tegmark, “An icosahedron-based method for pixelizing the celestial sphere”, *The Astrophysical Journal*, vol. 470, no. 2, pp. L81, 1996.

[61] Cabwe Amante and W Barry Eakins, “ETOPO1 1 arc-minute global re-

lief model: procedures, data sources and analysis. NOAA technical memorandum NESDIS NGDC-24", *National Geophysical Data Center, NOAA*, vol. 10, no. 2009, pp. V5C8276M, 2009.

[62] X Jerry Mitrovica, John Wahr, Isamu Matsuyama, and Archie Paulson, "The rotational stability of an ice-age earth", *Geophysical Journal International*, vol. 161, no. 2, pp. 491–506, 2005.

[63] X Jerry Mitrovica and John Wahr, "Ice age earth rotation", *Annual Review of Earth and Planetary Sciences*, vol. 39, pp. 577–616, 2011.

[64] R Valentina Barletta, C Ferrari, G Diolaiuti, T Carnielli, R Sabadini, and C Smiraglia, "Glacier shrinkage and modeled uplift of the alps", *Geophysical research letters*, vol. 33, no. 14, 2006.

[65] Duri Florineth and Christian Schlüchter, "Alpine evidence for atmospheric circulation patterns in Europe during the Last Glacial Maximum", *Quaternary Research*, vol. 54, no. 3, pp. 295–308, 2000.

[66] Willi Dansgaard, Sigfús J Johnsen, Henrik B Clausen, Dorte Dahl-Jensen, Nils S Gundestrup, Claus U Hammer, Christine S Hvidberg, Jørgen P Steffensen, AE Sveinbjörnsdottir, Jean Jouzel, et al., "Evidence for general instability of past climate from a 250-kyr ice-core record", *Nature*, vol. 364, no. 6434, pp. 218–220, 1993.

[67] Giorgio Spada, R Valentina Barletta, Volker Klemann, REM Riva, Zdenek Martinec, Paolo Gasperini, Björn Lund, Detlef Wolf, LLA Ver-

meersen, and MA King, "A benchmark study for glacial isostatic adjustment codes", *Geophysical Journal International*, vol. 185, no. 1, pp. 106–132, 2011.

[68] Giorgio Spada and Paolo Stocchi, *The sea level equation, theory and numerical examples*, Aracne Editrice, Roma, 2006.

[69] H Peter Plag, Hans-Ulrich Juettner, et al., "Inversion of global tide gauge data for present-day ice load changes", *Proceedings of the Second International Symposium on Environmental Research in the Arctic and Fifth Ny-Ålesund Scientific Seminar: Memoirs of the National Institute of Polar Research, Special Issue 54*, pp. 301–318, 2001.

[70] X Jerry Mitrovica and Glenn A Milne, "On the origin of late holocene sea-level highstands within equatorial ocean basins", *Quaternary Science Reviews*, vol. 21, no. 20-22, pp. 2179–2190, 2002.

[71] A Mark Tushingham and W Richard Peltier, "ICE-3G: A new global model of late Pleistocene deglaciation based upon geophysical predictions of post-glacial relative sea level change", *Journal of Geophysical Research: Solid Earth*, vol. 96, no. B3, pp. 4497–4523, 1991.

[72] Richard W Peltier, "Global glacial isostasy and the surface of the ice-age Earth: The ICE-5G (VM2) Model and GRACE", *Annual Review of Earth and Planetary Sciences*, vol. 32, no. 1, pp. 111–149, 2004.

[73] Jonathan Bamber and R Riva, "The sea level fingerprint of recent ice

mass fluxes", *The Cryosphere*, vol. 4, no. 4, pp. 621–627, 2010.

[74] Mark M Tamisiea, "Ongoing glacial isostatic contributions to observations of sea level change", *Geophysical Journal International*, vol. 186, no. 3, pp. 1036–1044, 09 2011.

[75] Pietro Sternai, Christian Sue, Laurent Husson, Enrico Serpelloni, Thorsten W Becker, Sean D Willett, Claudio Faccenna, Andrea Di Giulio, Giorgio Spada, Laurent Jolivet, et al., "Present-day uplift of the european alps: Evaluating mechanisms and models of their relative contributions", *Earth-Science Reviews*, vol. 190, pp. 589–604, 2019.

[76] Claudia Piromallo and Andrea Morelli, "Imaging the mediterranean upper mantle by p-wave travel time tomography", *Annals of Geophysics*, vol. 40, no. 4, 1997.

[77] Tanghua Li, Patrick Wu, Hansheng Wang, Holger Steffen, Nicole Khan, Simon Engelhart, Matteo Vacchi, Timothy Shaw, W. Peltier, and Benjamin Horton, "Uncertainties of glacial isostatic adjustment model predictions in North America associated with 3D structure", *Geophysical Research Letters*, vol. 47, pp. e2020GL087944, 05 2020.

[78] Daniele Melini and Giorgio Spada, "Some remarks on glacial isostatic adjustment modelling uncertainties", *Geophysical Journal International*, vol. 218, no. 1, pp. 401–413, 2019.

Chapter 4

STRENGTH OF THE LITHOSPHERE DERIVED BY GEOLOGICAL AND GEOPHYSICS DATA: THE GRAHAM LAND (ANTARCTIC PENINSULA) CASE STUDY

This chapter presents a method that allows studying of the strength of the lithosphere even when information at depth is scarce but sufficient surface data are available. It is widely known that the strength of the lithosphere and rheology control deformations and hence, a proper understanding of these properties, is essential if we want to best constrain future GIA models. Utilizing numerical modeling, are simulated lithospheric deformation as a function of geothermal heat flow and rheological parameters combined with the surface deformation model obtained from GNSS signals processing, as discussed in detail in Section 4.3. The Yield-Strength Envelope (YSE hereinafter) essentially represents a vertical profile which predicts the maximum differential stress supported by rock as a function of depth. In YSE rheology models, the depth dependence of rock strength integrates multiple factors such as the increase of both brittle and ductile strength with pressure, the decrease of ductile strength with depth-increasing temperature, lithological structure and fluid content. YSEs are used both to validate rock mechanics data and to explain the mechanical behavior of lithospheric plates.

To do this I wrote a MATLAB [1, 2] code that allows you to calculate the YSE as a function of the geological and geophysical parameters available in the literature as explained in more detail in Sec. 4.4.2. Below is a flowchart of the testing procedure that illustrates how the code works while a portion of the code is shown in the Appendix as an example.

This chapter follows closely a publication in preparation.

4.1 Introduction

The Antarctic continent is surrounded by the southern parts of Atlantic, Indian and Pacific Oceans (Figure 4.1) and is almost completely covered with ice that reaches an averages thickness of ~ 1.9 km average thickness [3]. Antarctic Peninsula (AP hereinafter) constitutes an 1300 km northward extension and was initially interpreted as a continental arc of the Gondwanan supercontinent margin, which developed during Mesozoic subduction [4]. The AP itself can be divided into Graham Land and Palmer Land, corresponding to the northern and southern portions of the peninsula, respectively. The AP is characterized by highly complex geotectonic surroundings, with two major tectonic plates converging in the area, the South American and the Antarctic Plates, and several minor tectonic plates interacting each other (*e.g.,* [5–7]). According to [8], the geology of the AP can be divided into six broad units; however, due to the complex tectonic setting, sparse rock exposure and lack of detailed exploration, the fundamental structures and evolution of West Antarctica are actively debated [9].

The study of geodynamics relies on an understanding of the strength of the lithosphere, but our knowledge has generally been obtained from centimeter-sized laboratory samples or from microstructural studies of naturally deformed rocks [10]. Rheology studies the laws that govern the deformation of rocks under the high temperature and pressure conditions of the mantle and require input from many disciplines in the geological and geophysical sciences (*e.g.,*

[11]). As a consequence, the strength of the Earth's lithosphere has been debated since the beginning of the last century [12], when the concept of a strong lithosphere overlying a viscous asthenosphere was first introduced [13]. The concept played a major role in the development of plate tectonics [14], and the question of how the strength of the plates varies spatially and temporally is a fundamental one of geology and geodynamics [15, 16].

One-dimensional lithospheric strength is usually represented by a diagram of shear-stress versus depth [17], known as the Brace-Goetze strength profile, or informally as the "Christmas tree", and strongly depends on the composition of the constituent rocks. This constitutive property is usually extrapolated from centimeter-sized laboratory samples [18, 19], from structural studies of naturally deformed rocks [20–22], or from a larger-scale perspective [23–26]. Many approaches are used to characterize the behavior of the lithosphere, and in particular its deformation. For several years, this has mainly been described by a model consisting of a weak lower crust, a relatively strong upper crust and uppermost mantle [17, 27]. Jackson (2002) [15] proposed a model with a weak mantle and a relatively strong lower crust in which the strength of the lithosphere is carried mainly by the brittle crust, renamed by Burov et al. (2006) [16] "crème brûlée" model. Subsequently, Bürgmann and Dresen (2008) [28] proposed a model, named "banana split" for high-deformation zones where processes such as grain-size reduction, chemical alteration, and phase changes weaken the major lithospheric faults.

Goetze and Evans (1979) [29] were the first to combine the data of experimental rock mechanics and extrapolate them to geological time and spatial scales. They introduced the YSE for the oceanic lithosphere, that is, a vertical profile which predicts the maximum differential stress supported by rock as a function of depth. In YSE rheology models, the depth dependence of rock strength integrates multiple factors such as the increase of both brittle and ductile strength with pressure, the decrease of ductile strength with depth-increasing temperature, lithological structure and fluid content. YSEs are used both to validate rock mechanics data and to explain the mechanical behavior of lithospheric plates [30].

In this work, following Bird (1989, 1999) [31, 32] and more recently Carafa and Barba (2011) [10], I determine YSE under Graham Land. Through numerical modeling, I simulate lithospheric strength under the study region as a function of Geothermal Heat Flow (GHF) and rheological parameters previously published in the literature and I combined them with the surface deformation model obtained from GNSS observations.

4.2 Beckground

4.2.1 Strain rate

Estimation of a strain rate field from spatially discrete velocity data is a long-standing issue to quantify crustal deformation [34] and different approaches

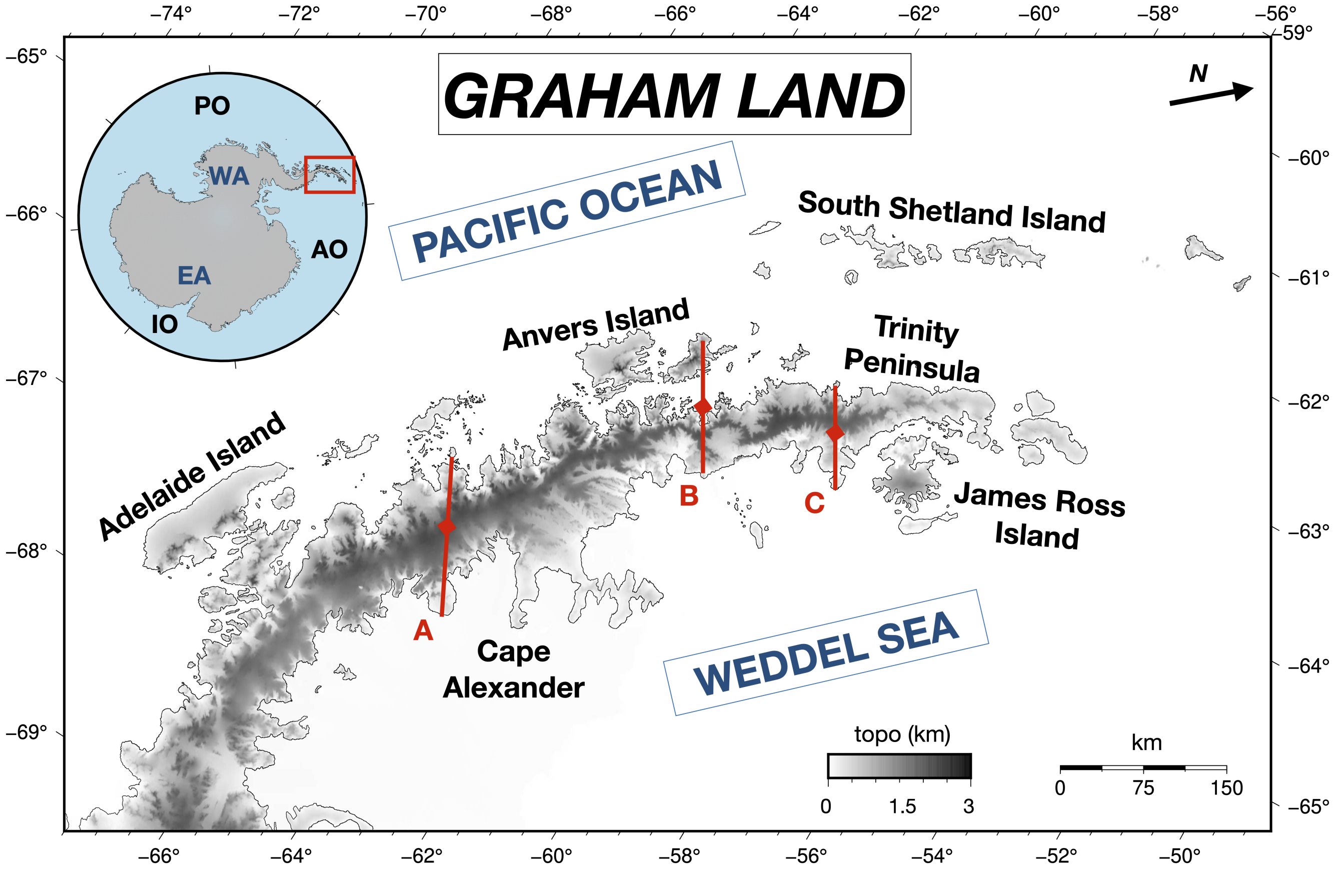

Figure 4.1. Detail of the study region, the Graham Land (AP) with major islands. The red lines indicate the location of three profiles (A, B and C) considered in this study. The grey scale represents topography according to the SRTM15+ global relief model [33]. In the upper left frame, overview of the Antarctic continent with the study area highlighted by the red box. WA: West Antarctica, EA: East Antarctica, PO: Pacific Ocean, AO: Atlantic Ocean and IO: Indian Ocean.

are used to derive strain information from instantaneous velocity data defined by global positioning (*e.g.,* [35–41]). Some authors divide a region into a triangulated network to estimate a mean strain rate within each cell using triangulation survey data [42–44]. However, in this approach, the estimated strains are discontinuous and depend on the partitioning scheme. More recently, continuous interpolation methods were developed. Haines and Holt (1993) [45] developed a method for calculating the continuous velocity gradient tensor in plate boundary zones using a bicubic spline function to interpolate scattered geodetic data, and this method has been adopted in many subsequent studies of crustal deformation (*e.g.,* [46]. This method prescribes a certain degree of smoothness on strain rate fields to stabilize the estimation from discrete velocity data without knowledge on major faults or block motions [34]. Sandwell and Wessel (2016) [47] did not introduce a *priori* assumptions about the fault structure and used an interpolation method of discrete 2-D vector data on the basis of Green's functions of an elastic body subject to forces in the plane. Teza et al. (2023) [48] developed a MATLAB toolbox for the computation of the strain rate field from the GNSS time series where the strain rate field is computed at the nodes of a chosen regular grid.

In the present study, I used *VISR*, a code developed by Shen et al (1996, 2015) [49, 50] that models strain rates as continuous functions and provides an interpolated velocity gradient field, using a modified least-squares method. This method is easy to understand and implement, and has been widely applied to investigate characteristics of crustal deformation fields (*e.g.,* [51–54].

4.3 Theory behind the strength of the lithosphere

4.3.1 Physical formulation of the strain rate

Under the assumption that the crust deforms as a continuum medium [55] I computed the 2-D strain rate tensor accounting for both ongoing geodynamic processes and feedback mechanisms of internal crustal deformation [56, 57]. The strain rate field is not affected by the choice of reference frame and can reflect the crustal deformation characteristics on different spatial scales [58–60]; therefore, in geodynamic studies, geodetic observations are a valuable source of data that can be used to detect, quantify, and model deformation in the Earth's crust [61].

If $\dot{u}_\theta$ and $\dot{u}_\lambda$ are velocities on the Earth's surface along the co-latitude (θ) and longitude (λ) directions, the components of strain rate can be expressed as [62]:

$$\dot{\varepsilon}_{\theta\theta} = \frac{1}{R}\frac{\partial \dot{u}_\theta}{\partial \theta} \tag{4.1}$$

$$\dot{\varepsilon}_{\lambda\lambda} = \frac{1}{R\sin\theta}\frac{\partial \dot{u}_\lambda}{\partial \lambda} + \frac{\dot{u}_\theta}{R}\cot\theta \tag{4.2}$$

$$\dot{\varepsilon}_{\theta\lambda} = \frac{1}{2}\left[\frac{1}{R}\left(\frac{\partial \dot{u}_{\lambda}}{\partial \theta} - \dot{u}\cot\theta\right) + \frac{1}{R\sin\theta}\frac{\partial \dot{u}_{\theta}}{\partial \lambda}\right] \tag{4.3}$$

where R denotes the Earth's radius, $\dot{\varepsilon}_{\theta\theta}$, $\dot{\varepsilon}_{\lambda\lambda}$ and $\dot{\varepsilon}_{\theta\lambda}$ represent the three independent components of the strain rate tensor and $\dot{u} = \sqrt{\dot{u}_{\theta}^2 + \dot{u}_{\lambda}^2}$ is the total horizontal velocity. Similarly, the vertical strain rate is given by:

$$\dot{\varepsilon}_{z} = -\dot{\varepsilon}_{\theta\theta} - \dot{\varepsilon}_{\lambda\lambda}. \tag{4.4}$$

From Eqs. (4.1 - 4.2) we can calculate the maximum ($\dot{\varepsilon}_{\mathrm{max}}$) and minimum ($\dot{\varepsilon}_{\mathrm{min}}$) principal strains as (*e.g.*, [63, 64]):

$$\dot{\varepsilon}_{\mathrm{max}} = \frac{1}{2}\left(\dot{\varepsilon}_{\theta\theta} + \dot{\varepsilon}_{\lambda\lambda}\right) + \sqrt{\frac{(\dot{\varepsilon}_{\theta\theta} - \dot{\varepsilon}_{\lambda\lambda})^2}{4} + \dot{\varepsilon}_{\theta\lambda}{}^2} \tag{4.5}$$

$$\dot{\varepsilon}_{\mathrm{min}} = \frac{1}{2}\left(\dot{\varepsilon}_{\theta\theta} + \dot{\varepsilon}_{\lambda\lambda}\right) - \sqrt{\frac{(\dot{\varepsilon}_{\theta\theta} - \dot{\varepsilon}_{\lambda\lambda})^2}{4} + \dot{\varepsilon}_{\theta\lambda}{}^2} \tag{4.6}$$

and the second invariant ($\dot{\varepsilon}_{\mathrm{2inv}}$), which reflects the magnitude of total strain rates, is estimated as:

$$\dot{\varepsilon}_{2\mathrm{inv}} = \sqrt{\dot{\varepsilon}^2_{\theta\theta} + \dot{\varepsilon}^2_{\lambda\lambda} + 2\dot{\varepsilon}^2_{\theta\lambda}}. \tag{4.7}$$

The maximum shear strain $\dot{\chi}$ rate is defined as

$$\dot{\chi} = \frac{1}{2}\left(\dot{\varepsilon}_{\mathrm{max}} - \dot{\varepsilon}_{\mathrm{min}}\right) \tag{4.8}$$

and, as discussed by [65], is related to regional tectonic shear deformation. By these strain rate components, we can fully characterize the horizontal surface deformation.

4.3.2 Numerical model of the strength of the lithosphere

Like described first by Bird (1989, 1999) [31, 32] and then by Carafa and Barba (2011) [10], the critical value of the shear stress $\tau_s(z)$, above which failure of the lithosphere occurs, is defined by the three quantities:

$$\tau_s^{\mathrm{fric}}(\mathrm{z}) = \rho_{\mathrm{litho}}\ \mathrm{g}\ \mathrm{z}\ (1 - \lambda^{'}) \tag{4.9}$$

$$\tau_s^{\text{creep}}(\text{z}) = \dot{\varepsilon}_{\text{2inv}} \ \exp\left(\frac{\beta + \xi_z}{T}\right) \ \dot{\chi} \tag{4.10}$$

$$\tau_s^{\text{plast}}(\text{z}) = 500 \text{ MPa}, \tag{4.11}$$

where ρ_{litho} is the density of the crust or mantle, g is gravity acceleration, z is depth, λ' is the pore fluid factor, $\dot{\varepsilon}_{\text{2inv}}$ is the second invariant of the strain rate, $\dot{\chi}$ is the maximum shear strain rate (both defined in Sec. 4.3.1) above, β and ξ_z are material constants listed in Table 4.3 and T is the temperature. τ_s^{fric}, τ_s^{creep} and τ_s^{plast} are brittle frictional sliding, dislocation creep and plastic deformation, respectively. For plastic deformation, the value of 500 MPa is based on the plasticity limit of olivine [66, 67]. The critical shear stress value is given by the minimum of those three upper bounds:

$$\tau_s(\text{z}) = \min(\tau_s^{\text{fric}}, \tau_s^{\text{creep}}, \tau_s^{\text{plast}}). \tag{4.12}$$

Assuming that no heat is produced inside the lithospheric mantle, the temperature increases linearly with depth [31]. The temperature gradient inside the lithospheric mantle is determined by the temperature and GHF at the

Moho boundary, since crust and mantle are assumed to be in thermal equilibrium [68]. In Eq. (4.10), the temperature T can be written as function of depth z as:

$$T(\mathrm{z}) = \left\{ \begin{array}{ll} T_{\mathrm{s}} + \frac{\mathrm{q\ z}}{k_{\mathrm{c}}} - \frac{H\ z^2}{2k_{\mathrm{c}}} & ,\text{if } z \leq z_{\mathrm{c}} \\ \\ T_{\mathrm{c}} + \frac{(\mathrm{q}-Hz_{\mathrm{c}})\ (z-z_c)}{k_m} & ,\text{if } z_{\mathrm{c}} > z \end{array} \right\} \tag{4.13}$$

where q is the surface GHF, k_{c} and k_{m} are the conductivities of the crust and mantle, respectively, z_c is the thickness of the crust, T_{s} and T_{c} are the temperatures at the surface and at the base of the crust, respectively, and H is the radiogenic heat production rate within the crust, assumed to be zero in the mantle.

Finally, the strength of the lithosphere, which describes the maximum rock strength as a function of depth [29], is given by:

$$\Sigma = \int\limits_{0}^{\mathrm{z}} \tau_s(\mathrm{z})\mathrm{dz}. \tag{4.14}$$

4.4 Materials and methods

In this section I describe the processing scheme used for the analysis of GNSS time series and discuss the model parameters necessary for setting up of the rheological model for the Graham Land.

4.4.1 GPS data and processing

We processed data recorded at 21 continuous and "not-continuous" GNSS time series for Graham Land (see Figure 4.2 and Tables 4.1 - 4.2) covering a time period from 1997 to 2022, using the database from the Nevada Geodetic Laboratory (NGL) at the University of Nevada, Reno (details on the data set are available on the NGL webpage `http://geodesy.unr.edu/index.php`). All considered stations have time-series that are at least 2.5 years long between January 1997 and December 2022; that represents the minimum acceptable length to ensure that estimated trends are not significantly affected by biases due to seasonal components [69–72].

GPS data were processed by using the MIDAS software (Median Interannual Difference Adjusted for Skewness) median-trend algorithm introduced by Blewitt and Wesssel (2016) [73] that represents a variant of the Theil-Sen non-parametric median trend estimator [74, 75]. We also take into account the equipment changes tabulated by NGL from station "site logs" (i.e., antenna/radome changes and changes in receiver). The MIDAS-estimated velocity is essentially the median of the distribution of 1 year slopes, making it insensitive to the effects of steps in the time series if they are sufficiently infrequent. The uncertainties obtained with MIDAS have a realistic meaning and usually do not require further scaling (*e.g.,* [76–80]). Estimated 3D velocities and their associated uncertainties are listed in Tables (4.1 - 4.2).

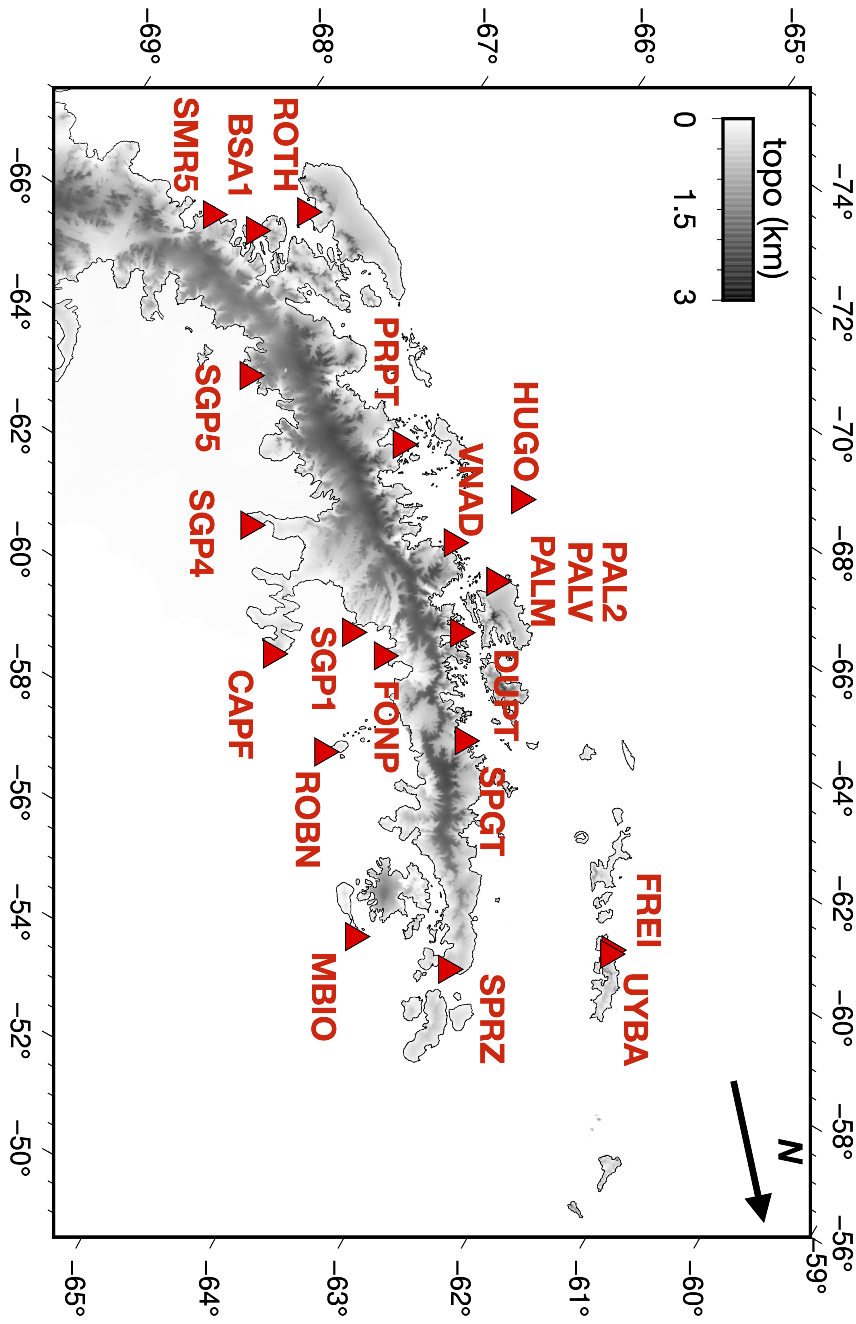

Figure 4.2. Location of the 21 GNSS stations used in this study.

Table 4.1. GNSS velocities estimated with the MIDAS algorithm at the 21 sites considered in this study and associated uncertainties. Velocities are in the Antarctic Plate reference frame.

ID	LON	LAT	EAST	NORTH	UP	σ_{east}	σ_{north}	σ_{up}
	(deg)	(deg)	(mm yr^{-1})	(mm yr^{-1})	(mm yr^{-1})	(mm yr^{-1})	(mm yr^{-1})	(mm yr^{-1})
BSA1	-67.29	-67.81	1.47	-1.01	1.50	0.18	0.26	0.87
CAPF	-60.56	-66.01	1.25	-2.58	2.62	0.16	0.19	0.54
DUPT	-62.82	-64.80	-1.35	-0.94	8.82	0.17	0.22	0.70
FONP	-61.65	-65.24	0.79	-5.07	15.62	0.36	0.48	1.07
FREI	-58.98	-62.19	-4.70	5.90	-4.40	0.52	0.55	1.09
HUGO	-65.67	-64.96	0.52	-0.44	-0.70	0.15	0.22	0.67
MBIO	-56.62	-64.24	4.11	-2.41	3.86	0.29	0.36	0.87
PAL2	-64.05	-64.77	-0.85	-0.83	4.94	0.15	0.21	0.61
PALM	-64.05	-64.77	-1.02	-0.68	4.75	0.13	0.18	0.48
PALV	-64.05	-64.77	-1.20	-0.95	5.05	0.22	0.29	0.80
PRPT	-65.34	-66.01	1.00	-1.04	-0.10	0.22	0.27	0.98

Table 4.2. GNSS velocities estimated with the MIDAS algorithm at the 21 sites considered in this study and associated uncertainties. Velocities are in the Antarctic Plate reference frame.

ID	LON (deg)	LAT (deg)	EAST (mm yr^{-1})	NORTH (mm yr^{-1})	UP (mm yr^{-1})	σ_{east} (mm yr^{-1})	σ_{north} (mm yr^{-1})	σ_{up} (mm yr^{-1})
ROBN	-59.44	-65.25	2.86	-3.53	6.63	0.28	0.30	0.58
ROTH	-68.12	-67.57	0.96	-1.20	3.42	0.18	0.25	0.71
SGP1	-61.72	-65.56	0.29	-3.34	6.74	0.35	0.47	1.26
SGP4	-62.46	-66.68	0.00	-1.57	1.46	0.38	0.44	1.42
SGP5	-64.89	-67.28	0.73	-0.40	-0.70	0.41	0.42	2.24
SMR5	-67.10	-68.13	0.65	-0.15	2.61	0.32	0.44	1.44
SPGT	-61.05	-64.29	1.37	0.75	8.88	0.19	0.27	0.79
SPRZ	-56.99	-63.39	2.63	-1.77	1.87	0.32	0.39	1.18
UYBA	-58.90	-62.18	-3.99	5.92	-2.24	0.51	0.75	2.16
VNAD	-64.25	-65.24	-0.75	-1.23	4.21	0.23	0.30	0.84

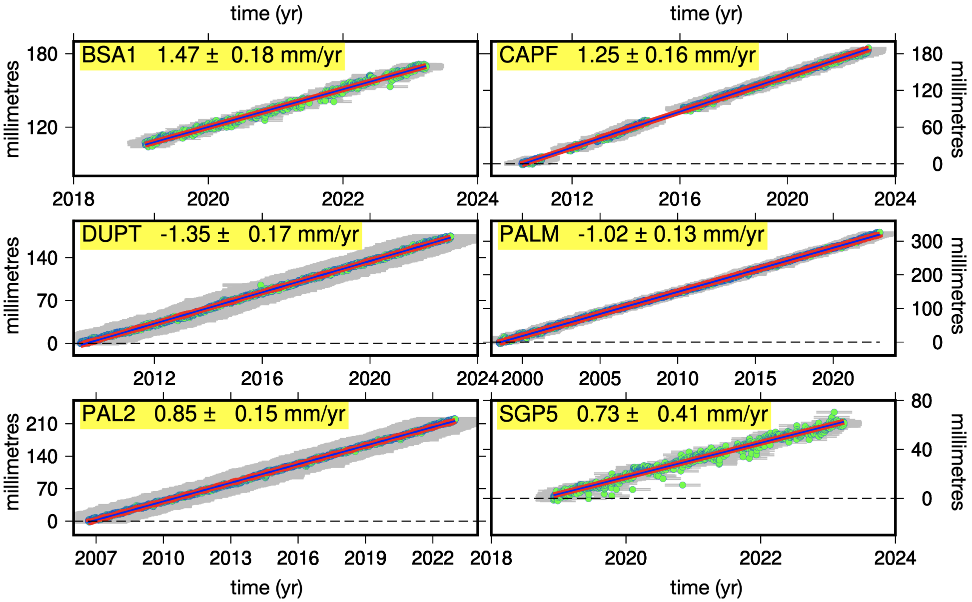

Figure 4.3. GNSS daily time series (east-component). The red line represents the GPS velocity computed by MIDAS [73], and the green solid circles represent the offset daily coordinate time series. Please note that both horizontal and vertical axes vary.

4.4.2 Model parameters

YSE have been calculated over the last few years for a number of locations in Europe [10, 81, 82], America [83] and Asia [67], but are not available on a regional scale for Antarctica. Based on previously published data, we constructed a 1-dimensional strength map for the Graham Land lithosphere. Since large parts of Antarctica are not yet covered by seismic surveys, the gravity and crustal structure models are used to interpolate the Moho information where

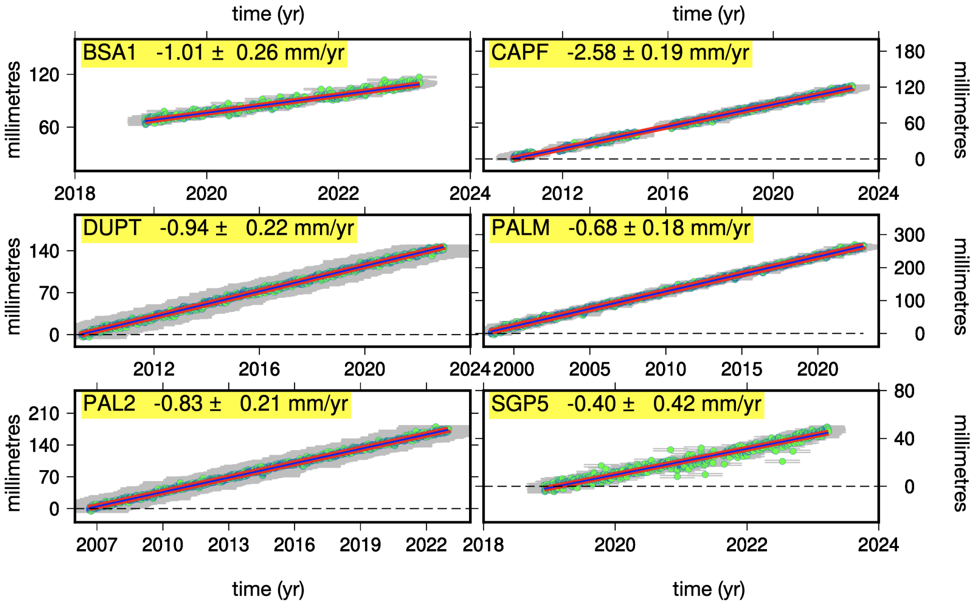

Figure 4.4. GNSS daily time series (north-component). The red line represents the GPS velocity computed by MIDAS [73], and the green solid circles represent the offset daily coordinate time series. Please note that both horizontal and vertical axes vary.

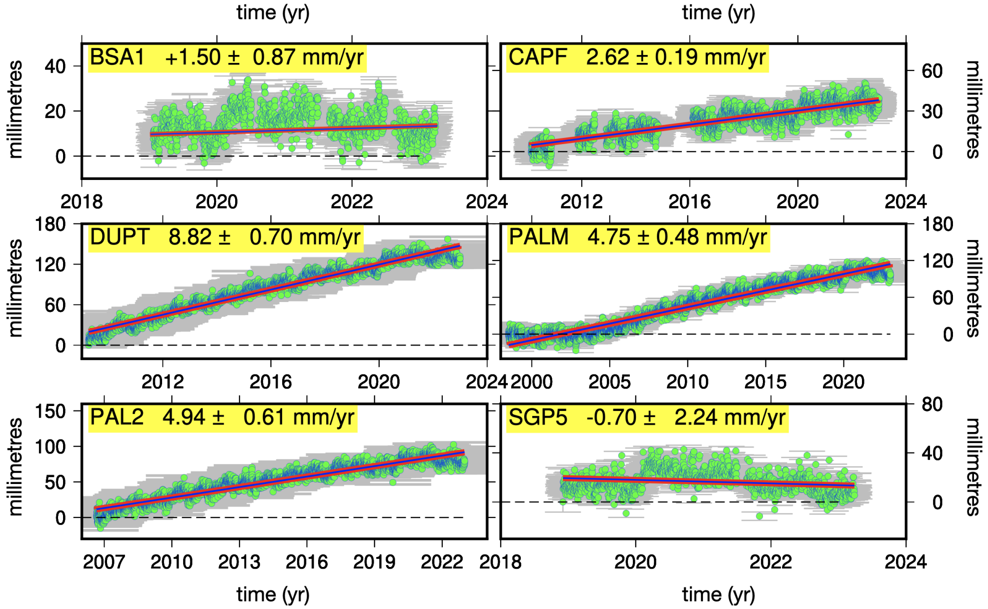

Figure 4.5. GNSS daily time series (up-component). The red line represents the GPS velocity computed by MIDAS [73], and the green solid circles represent the offset daily coordinate time series. Please note that both horizontal and vertical axes vary.

seismic data are missing. Following Baranov et al. (2018) [84], I adopted an average Moho depth value of 38 km for profile A, 34 km for profile B and 36 km for profile C (the three profiles are traced in Figure 4.11) while in Figure 4.6 is shown the Moho depth derived by [84].

Thermal rocks properties and rheological parameters (listed in Table 4.3) were taken from various sources in the literature. An et al. (2015) [85] extracted petrologic and geodynamical information, like temperature and lithospheric thickness, from seismic velocity data. Burton et al. (2017) [86] presented a new methodology that allows calculating and combining crustal heat production with geophysical models, producing a new map of GHF on the AP. Godge (2018) [87] reports that estimates of GHF in Antarctica can be extrapolated from heat production determined by the geochemical composition of glacial rock clasts eroded from the continental interior. Results indicate a higher GHF on the east and south of the Peninsula (mean 81 mW m^{-2}), where silicic rocks predominate, than on the west and north (mean 67 mW m^{-2}) where volcanic arc and quartzose sediments are dominant.

In order to explore the range of GHF values for each of the three studied areas (A, B and C), we adopted a GHF uniform value of 55 (A), 60 (B) and 65 (C) mW m^{-2} to represent the average heat flow within each area. That is largely consistent with inferences based on satellite magnetic data [88], on seismology [85], on geodynamic modeling [89] and on in situ measurements [90, 91]. I assume a value of radioactive heat production in the crust of 0.4 μW m^{-3} [92]

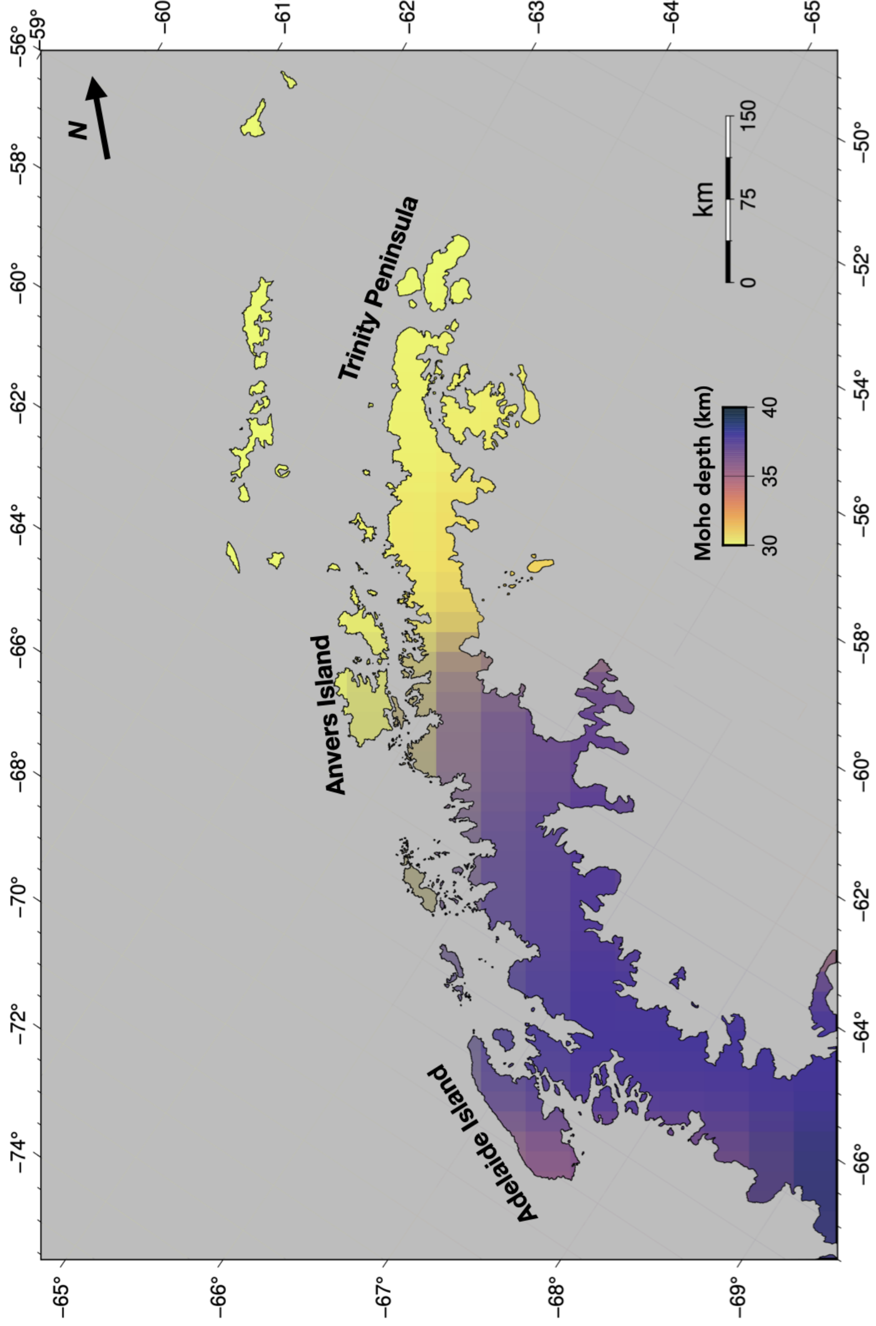

Figure 4.6. Moho depth beneath the Antarctic Peninsula. Data from Baranov et al. (2018) [84].

and fixed heat production rate of 0.02 μW m^{-3} in the mantle [91, 93]. I use a value of thermal conductivity of 2.5 Wm^{-1}K^{-1} for the crust and 3.5 Wm^{-1}K^{-1} for the mantle [30, 68, 85, 94]. I adopted a pre-exponential constant in creep rheology equal to 2.3 MPa in the crust (1.95$\times$10^{-2} MPa for the mantle), which depends both on grain size and volatile impurities [11], a depth coefficient in creep rheology of zero in the crust (1.71$\times$10^{-2} K m^{-2} for the mantle and a stress exponent in creep rheology equal to 0.33 [31]. For the temperature coefficient I defined four different sets of parameters that represent distinct and possible behaviors of the lithosphere within the study region (coefficients β_1 to β_4 in Table 4.3) and include granite wet and anorthosite for the crust and plagioclase and olivine for the mantle [28, 95], and I use the median value of those parameters. The friction coefficient used is equal to 0.85 [96, 97]. The assumed pore fluid factor is equal to 0.36, which is a typical hydrostatic value.

I performed several numerical experiments in which the GHF and the rheological parameters were varied to compute predictions of the YSE. I performed this modeling in two steps. I first estimated geodetic velocities and strain rade field from GNSS data over the whole (see Sec. 4.5.1, 4.5.2 and 4.5.3). Second, I considered the GHF and the rheological parameters as free parameters. Then, we explored the range of uncertainty in each parameter by a trial-and-error procedure with discrete sampling steps. Each combination of GHF, temperature coefficient for creep rheology and set of rheological parameters (β_1 to β_4) constitutes an independent simulation. For each combination, the model predictions were computed with a MATLAB code. A flowchart illustrating out modelling workflow is shown in the Figure. 4.7, while some of the code is shown in the Appendix A as an example.

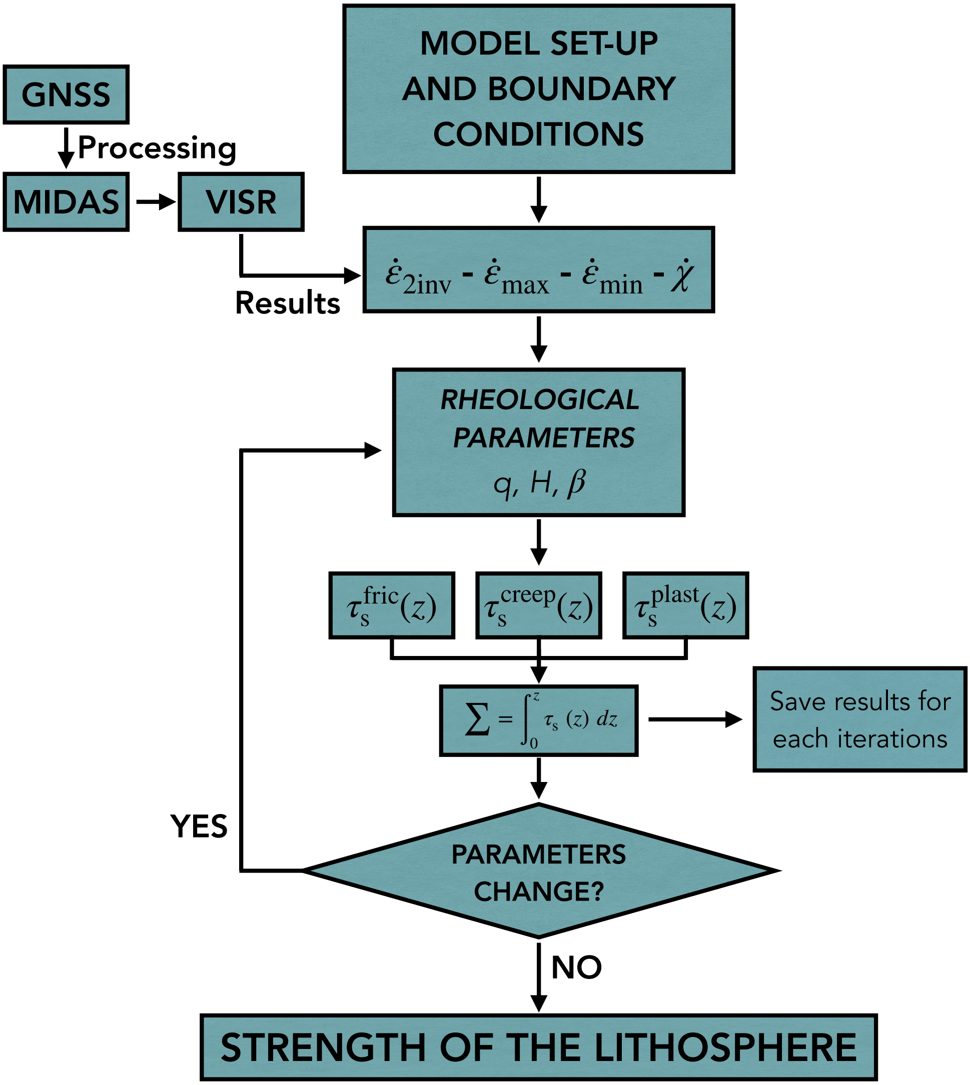

Figure 4.7. Modeling workflow adopted in my MATLAB code.

Table 4.3. Rheological model parameters used in our simulations. Mantle values are given in parentheses. For parameters that have been set differently in the three considered profiles, the symbols (A), (B) and (C) correspond to the values assumed in each region.

Description	Parameter	Units	Value
Geothermal heat flow (GHF)	q	$\mathrm{mW\ m^{-2}}$	55 – 60 – 65
Radioactive heat production	H	$\mu\ \mathrm{W\ m^{-3}}$	0.40 (0.02)
Thermal conductivity	k_t	$\mathrm{W \cdot m^{-1}K^{-1}}$	2.5 (3.5)
Pre-exponential constant in creep rheology	α	MPa	2.3 (0.0195)
Depth coefficient in creep rheology	ξ	$\mathrm{K\ m^{-2}}$	0 (0.0171)
Stress exponent in creep rheology	n		0.3333
Temperature coefficient in creep rheology	β_1	$\mathrm{K^{-1}}$	8600 (18000)
	β_2	$\mathrm{K^{-1}}$	9600 (18500)
	β_3	$\mathrm{K^{-1}}$	10650 (19000)
	β_4	$\mathrm{K^{-1}}$	11650 (19500)
Mean crust density	ρ_litho	$\mathrm{kg\ m^{-3}}$	2899 (3332)
Mean water density	ρ_water	$\mathrm{kg\ m^{-3}}$	1032
Surface temperature	T	K	273
Standard coefficient of friction	μ		0.85
Pore fluid factor	λ'		0.36
Moho depth		km	38 (A) - 34 (B) - 36 (C)

4.5 Results

Here, I present an up-to-date crustal velocity field of the Graham Land, based on an combination of permanent and non-permanent GPS observations. Afterwards, I present my estimate of the rheological profile beneath the study area derived from combinations of geological and geophysical data.

4.5.1 Vertical velocity

The present day vertical land movement (VLM) results from the combination of different components due to tectonics, sediment loading and compaction and GIA processes [98, 99]; however, all these components induce non-negligible displacements although their magnitude and relative importance have changed over time.

Figure 4.2 shows the vertical velocity field over Graham Land and its associated uncertainty, as obtained by interpolating the estimates at each GNSS site listed in Table 4.3. The interpolated field has been obtained through adjustable tension continuous curvature splines method employing a tension factor of 0.5 [100]. The map shows widespread uplift, with subsidence occurring only at 5 stations out of 21, FREI (-4.40 ± 1.09 mm yr^{-1}), HUGO (-0.70 ± 0.67 mm yr^{-1}), PRPT (-0.10 ± 0.98 mm yr^{-1}), SGP5 (-0.70 ± 2.24 mm yr^{-1}) and UYBA (-2.24 ± 2.16 mm yr^{-1}). Our interpolated uplift model indicates vertical movements in the range from -4.40 to $+15.62$ mm yr^{-1} in the study area, with uplift rates reaching the maximum value at FONP (15.62 ± 1.07) mm yr^{-1}, SPGT (8.88 ± 0.79 mm yr^{-1}), DUPT (8.82 ± 0.70 mm yr^{-1}) and SGP1 (6.74 ± 1.26 mm yr^{-1}). Uncertainties on vertical velocities (Figure 4.8b) are in the range from ± 0.4 mm yr^{-1} to ± 2.2 mm yr^{-1}. The map in Figure 4.8a clearly highlights the diffuse state of uplift in the Graham Land. Overall, the region between Anvers Island and Cape Alexander is the one with the highest uplift rates, while the South Shetland Island region has low rates of subsidence. The weighted average of vertical velocities over all the considered stations is (+3.56 ± 1.00) mm yr^{-1}.

4.5.2 Horizontal velocity

Previous studies have attributed the horizontal displacement field of the Antarctica Continent to a rigid plate rotation and deformation related to the change in ice mass [101–106]. The melting of the ice began at the end of the last glaciation and produced a slow crustal deformation that still today is affected by the alteration of glacial flows [107]. However, even the breakup of ice shelves produces regional variations in the displacement pattern: this happened in the Northern AP following the 2002 breakup of the Larsen ice shelf, as a consequence of the combined effects of solid Earth's elastic response and the viscoelastic processes in response to recent ice unloading [105, 108].

Figure 4.9 shows horizontal velocities at the 21 GNSS sites relative to the fixed terrestrial reference system of the Antarctic plate. Two distinct kinematic

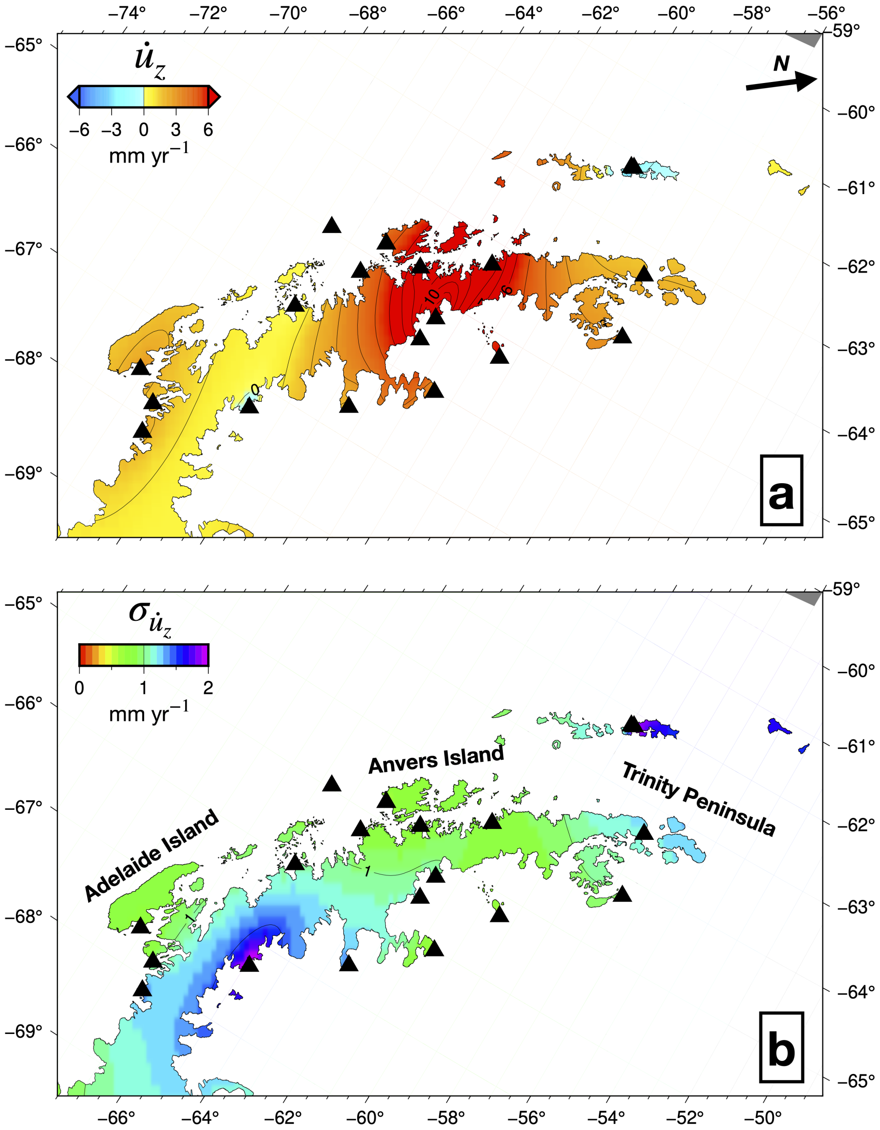

Figure 4.8. (a) Interpolated vertical velocity $\dot{u}_z$ and (b) associated uncertainty $\sigma_{\dot{u}_z}$ over the study area. Note that the color scale in frame (a) is saturated at ±6 mm/yr. The interpolation has been obtained with program `surface`, which is part of the GMT (Generic Mapping Tools) package by Wessel and Smith (1998) [100], employing a tension factor of 0.5.

patterns can be clearly seen. The area between Anvers Island and Trinity Peninsula, including South Shetland Islands (see labels in Figure 4.1), shows increasing W-E oriented deformation with maximum values recorded at FREY (5.90 ± 0.55 mm yr^{-1}) and FONP (-5.07 ± 0.48 mm yr^{-1}). Conversely, the southern part (between Anvers Island, Cape Alexander and Adelaide Island) exhibits a very small (insignificant) deformation, indicating that this region is relatively stable, with values ranging from (0.10 ± 0.1) mm yr^{-1} to (0.50 ± 0.02) mm yr^{-1}.

4.5.3 Strain rate field

The horizontal strain-rates have been estimated on a regular 0.5° × 0.5° grid over the investigated area by adopting the method reported in Shen et al. (20215) [50] and described in Section 4.2.1. This method allows introducing different spatial weighting functions of data, like uniform Gaussian or quadratic spatial weighting functions, enabling to obtain a finer resolution, especially on regions characterized by sparsely distributed data. Based on some preliminary tests, the horizontal strain-rate field has been estimated by adopting a weighting threshold of 2 and by using a Gaussian function for distance weighting and azimuth cell for areal weighting, respectively.

The estimated horizontal strain rates ($\dot{\varepsilon}_{\mathrm{min}}$ and $\dot{\varepsilon}_{\mathrm{max}}$) and the second invariant of the strain rates ($\dot{\varepsilon}_{2\mathrm{inv}}$) are shown in Figure 4.10. Principal strain rates across Graham Land are very small, and the larger values are mostly concentrated

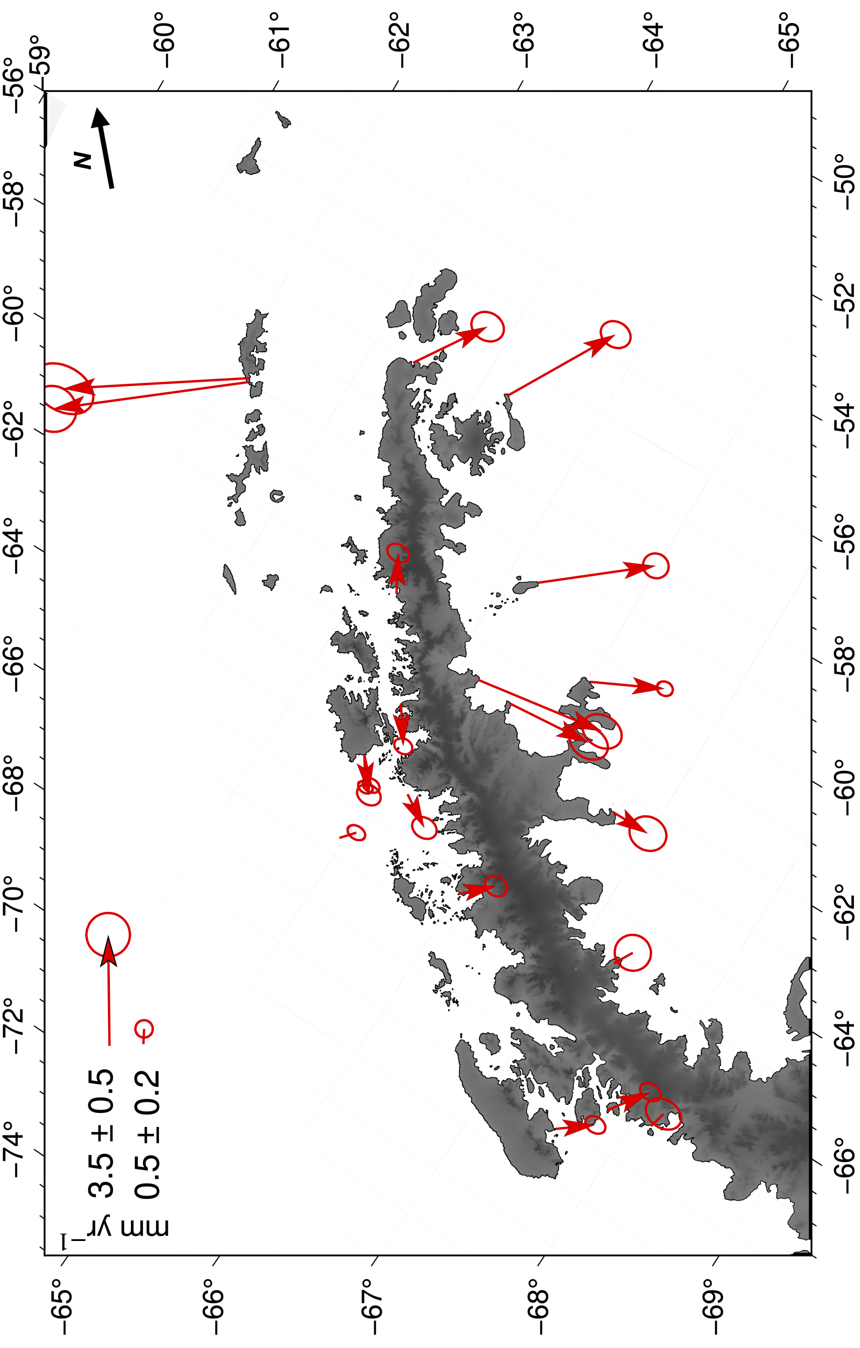

Figure 4.9. Horizontal velocities at the 21 GNSS sites in a fixed Antarctic Plate terrestrial reference frame. Error ellipses are at the 95% confidence level.

on the northern part of the study area, between Anvers Island and Trinity Peninsula. On the whole, the principal strain rates are extensive in the NW-SE direction in Graham Land although their orientations change direction slightly as we move toward south, between Anvers Island, Cape Alexander and Adelaide Island. The highest values for principal extensive strain rates are found to be at the 90-100 μ-strain yr^{-1} level.

Figure 4.10 shows that, between Cape Alexander and Adelaide Island, the magnitudes of the maximum and minimum principal strain rates are almost the same. The spatial distribution of the second invariant of strain rate tensor, $\dot{\varepsilon}_{2\mathrm{inv}}$, that reflects the magnitude of the total strain rates, shows values generally smaller of 60 μ-strain yr^{-1}. The highest values are located in the northern part of the AP, between Anvers Island and Trinity Peninsula, with values between 95 and 101 μ-strain yr^{-1}. Indeed, large rates for the strain tensor are generally associated with areas where uniaxial compressive stresses of different magnitudes dominate [61]. In the southern part, between Anvers Island, Cape Alexander and Adelaide Island the strain rate tensor abruptly becomes smaller, with value between 5 and 15 μ-strain yr^{-1}.

We can conclude that the northern part of Graham Land, between Anvers Island and Trinity Peninsula, has a much more accentuated kinematics with the deformation vectors indicating a general extension of the area (oriented about the W-E direction). In contrast, the southern part, between Anvers Island, Cape Alexander and Adelaide Island, appears to exhibit widespread stability, with small strain values. This is consistent with vertical velocities, as shown in Figures 4.8 and 4.9, respectively.

4.5.4 The yield strength envelop

In any depth range, rocks tend to deform by the dominant mechanism that exhibits the lowest strength [67, 109, 110], and the rheological strength of the lithosphere at a specific depth is generally described by the YSE, defined in Eq. (4.14) above. In plots showing the strength as a function of depth, two types of profiles correspond to different regimes. Straight lines correspond to a brittle fracture and demonstrate an increase of strength with depth. Curved lines describe a viscous deformation according to the Power and Dorn law where strength decreases downwards exponentially due to the increase of temperature with a corresponding decrease of viscosity [111].

In order to analyze the lithospheric strength of the Graham Land, in Figure 4.11 I display the YSE under three areas (profiles A, B and C respectivley, chosen arbitrarily). The crustal integrated strength varies in the range from 0 to 500 MPa and depends more on strain rate and thermal regime (GHF) than on crustal thickness. Profile A in Figure 4.11a exhibits the largest strength of the three areas with peak strength concentrated within the upper crust. In the crust, the peak value of the shear stress is 500 MPa and is reached at depth of 16-18 km for a GHF of 55 mW m^{-2} (green line), of 16 km for a GHF of 60 mW m^{-2} (blue line) and of 15 km for a GHF of 65 mW m^{-2} (purple

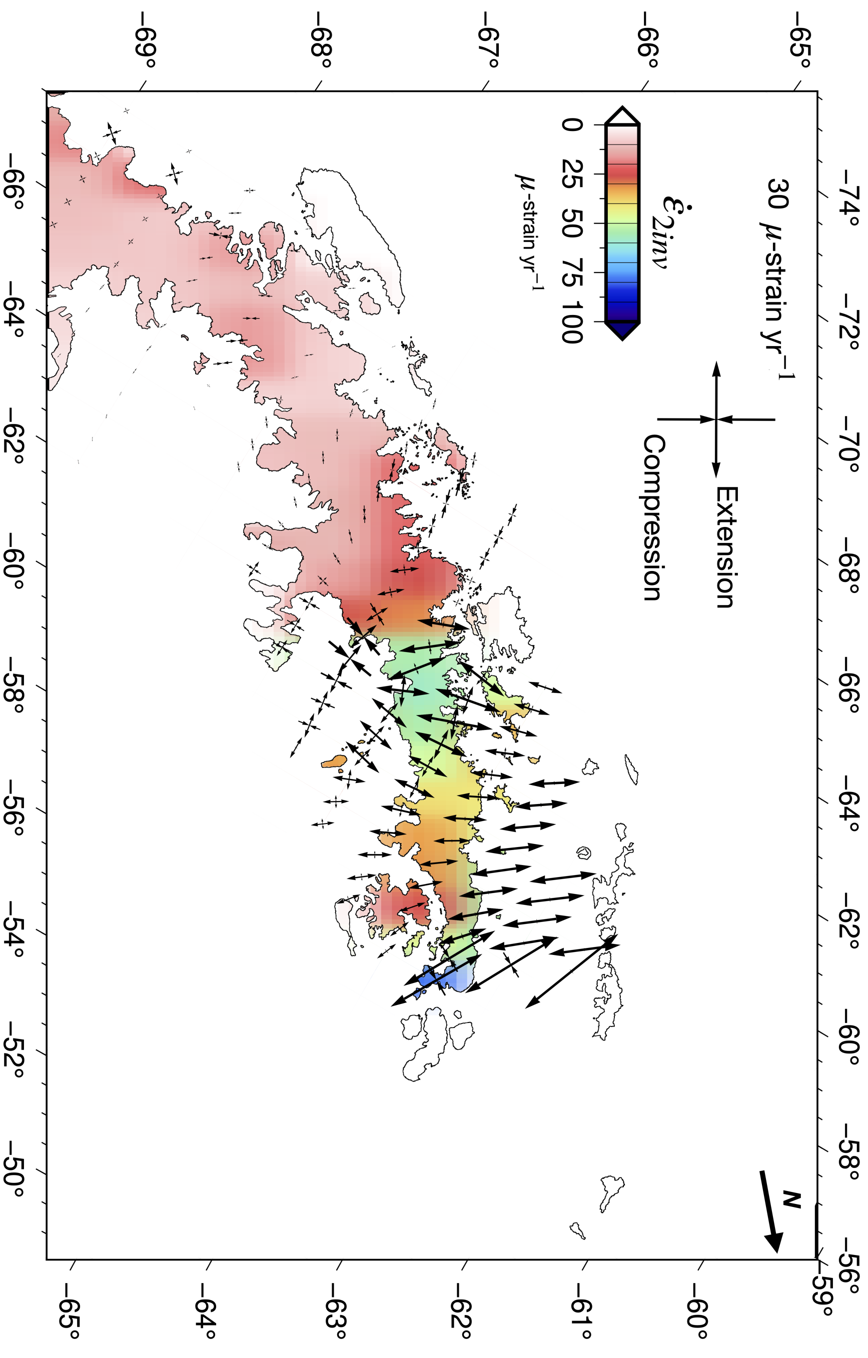

Figure 4.10. Horizontal strain-rates field corresponding to extension ($\dot{\varepsilon}_{max}$) and compression ($\dot{\varepsilon}_{min}$). The colors in the background correspond to the value of the second invariant of the strain rate.

line). The mantle below profile A appears to be ductile, with a maximum shear stress value of 180 MPa at a depth of 39-40 km (GHF = 55 mW m^{-2}) and drops below 50 MPa as we increase the value of GHF (45 MPa for GHF of 60 mW m^{-2} and 14 MPa for GHF of 65 mW m^{-2}). The profiles B and C (Figure 4.11b-c) show a rather similar pattern with a weak upper crust overlying a relatively stronger mantle. For profile B the peak values of the shear stess are 162 MPa at a depth of 23 km (for a GHF of 55 mW m^{-2}), 148 MPa at 21 km (for a GHF of 60 mW m^{-2}) and 134 MPa at 19 km (for a GHF of 66 mW m^{-2}). The mantle below profile B (Figure 4.11b) has the highest strength. Here, the shear stress profile for the upper mantle indicates that plastic behavior occurred within a thickness of 9 km, with a maximum shear stress value of 297 MPa at depth of 41 km (GHF of 55 mW m^{-2}). Depth of plastic behavior is reduced to 4 km, with a maximum of 246 MPa, if we consider a GHF equal to 60 mW m^{-2}. Profile C in Figure 4.11c is essentially identical to profile B for the crustal part while some differences can be observed in the mantle. For a GHF of 60 mW m^{-2}, the magnitude of the strength in the depth range of 38-40 km for the profile C is nearly half that for profile B, with the magnitude of the strength for profile C approximately 130 MPa at 37 km. Here, the shear stress profile for the upper mantle indicates that plastic behavior occurs within a thickness of 4 km, with a maximum shear stress value of 279 MPa at depth of 40 km (GHF of 55 mW m^{-2}).

In general, the lithospheric strength is primarily concentrated in the upper and middle crust for the profile A (Figure 4.11a), indicating that this part of the study area deforms according to the “crème brûlée” model [15]. However for profiles B anc C (Figure 4.11b-c) the lithospheric strength is primarily concentrated in the upper mantle and the strength of the crust is relatively low, indicating that this part of the study area deforms according to the “jelly sandwich model” [112].

4.6 Conclusion

The strength of the lithosphere can vary drastically within a few kilometers, changing from a strong crust and a weak mantle to a weak crust and a relatively strong mantle as discussed in Section 4.5.4 above. The approach used in this Chapter has allowed us to analyze the strength of the lithosphere beneath the Graham Land region. The main results of this work are summarized as follows.

(i) We defined a 3D velocity field for Graham Land from available deformation time-series recorded by GNSS networks. Vertical velocities show an uplift over almost all the study area, with peak rates of about 15 mm yr^{-1} occurring in the central region, between Cape Alexander and Avers Island. Horizontal velocities, conversely, show two distinct kinematic regimes, with a W-E oriented expansion of the area between Anvers Island and Trinity Peninsula at a rate of over 5 mm yr^{-1} and a very small deformation in the southern part of Graham Land.

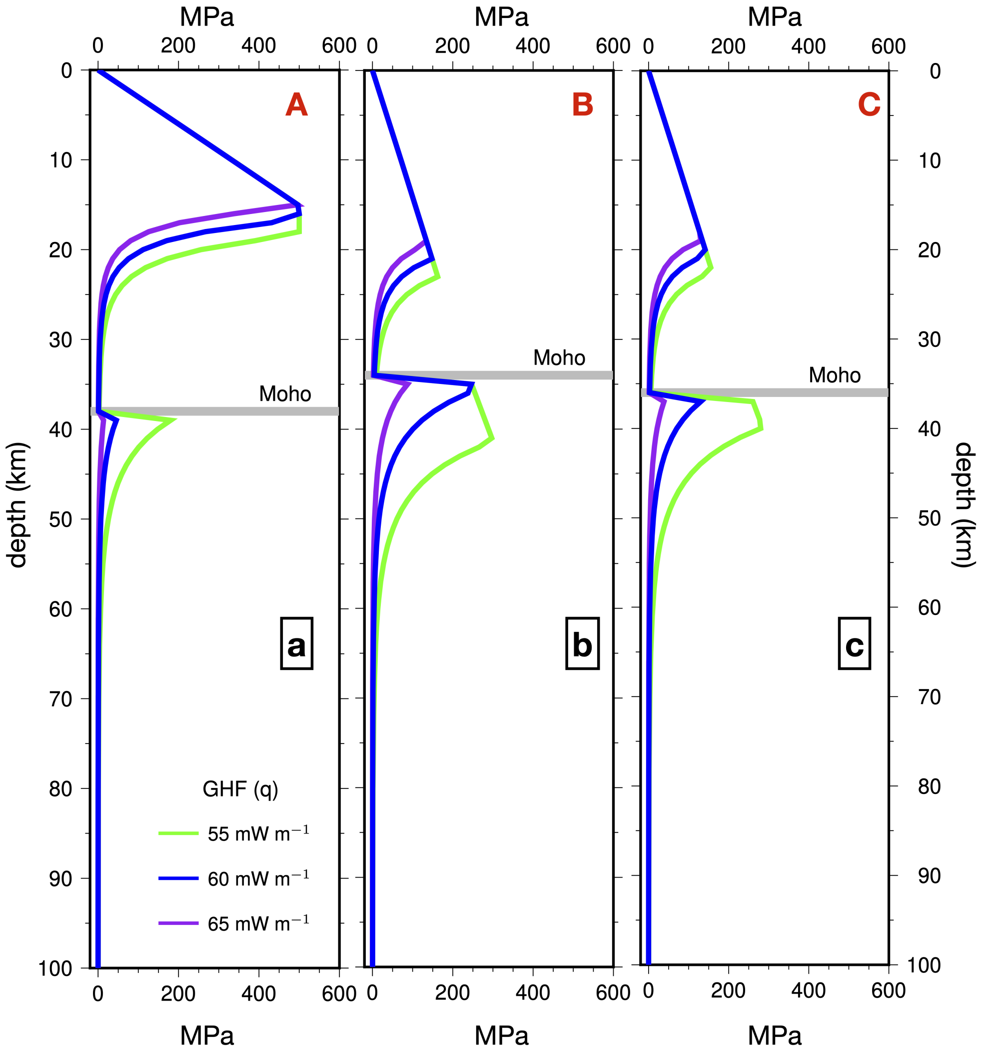

Figure 4.11. Computed Yield Strength Envelope (YSE) as a function of depth for profiles A, B and C. Green, blue and purple lines represent a YSE for a GHF of 55, 60 and 65 mW m^{-2}. The grey line in the three profiles represents Moho depth derived by Baranov et al. (2018) [84].

(ii) The estimated horizontal strain rates ($\dot{\chi}$) and the second invariant of the strain rates ($\dot{\varepsilon}_{2\mathrm{inv}}$) have been determined on the basis of the GNSS velocity field. In the area between Anvers Island and Trinity Peninsula, the main strain rates are found with vectors oriented approximately W-E. In contrast, the area between Anvers Island, Adelaide Island and Cape Alexander appears to exhibit widespread stability, with small strain values.

(iii) The lithosphere beneath the Graham Land is characterized by integrated crustal strength in a range from 0 to 500 MPa, depending more on strain rate and thermal regime (GHF) than on crustal thickness. The lithospheric strength is primarily concentrated in the crust in the southern part of the region (profile A) while is primarily concentrated in the mantle in the northern part (profiles B and C). The results of our study demonstrate that both “jelly sandwich“ and “crème brûlée” models are valid for the Graham Land region depending on specific thermal and rheological conditions of the area considered. However, it should be noted that as GHF increases, the integrated strength of the lithosphere decreases while an increase in the strain rate may increase the integrated strength of the lithosphere.

GIA studies of the early 20th century have contributed to the definition of the mechanical lithosphere as the uppermost layer of the solid Earth characterized by slow visco-elastic relaxation, in contrast to the underlying, relatively low viscosity asthenosphere. Therefore, knowledge of the crustal and upper mantle rheological structure of Graham Land, or more generally of the Antarctic continent, is important for understanding the geological processes but also to better constrain geophysical processes such as that of the GIA where rheology plays an important role.

Bibliography

[1] The MathWorks Inc., "Matlab version: 9.13.0 (r2022b)", 2022.

[2] The MathWorks Inc., "Optimization toolbox version: 9.4 (r2022b)", 2022.

[3] GE Grikurov and GL Leitchenkov, "Tectonics of the Antarctic", *La cartographie de la terre et ses océans*, vol. 201, 2019.

[4] Manuel Suárez, "Plate-tectonic model for southern Antarctic Peninsula and its relation to southern Andes", *Geology*, vol. 4, no. 4, pp. 211–214, 1976.

[5] Jesús Galindo-Zaldıvar, Luiz Gamboa, Andrés Maldonado, Seizo Nakao, and Yao Bochu, "Tectonic development of the Bransfield Basin and its prolongation to the South Scotia Ridge, northern Antarctic Peninsula", *Marine Geology*, vol. 206, no. 1-4, pp. 267–282, 2004.

[6] Adolfo Maestro, Luis Somoza, Jorge Rey, J Martínez-Frías, and Jerónimo López-Martínez, "Active tectonics, fault patterns, and stress

field of Deception Island: a response to oblique convergence between the Pacific and Antarctic plates", *Journal of South American Earth Sciences*, vol. 23, no. 2-3, pp. 256–268, 2007.

[7] Manuel Berrocoso, A Fernández-Ros, Gonçalo Prates, A García, and S Kraus, "Geodetic implications on block formation and geodynamic domains in the South Shetland Islands, Antarctic Peninsula", *Tectonophysics*, vol. 666, pp. 211–219, 2016.

[8] Autochthonous v Burton-Johnson and TR Riley, "Autochthonous v. accreted terrane development of continental margins: a revised in situ tectonic history of the Antarctic Peninsula", *Journal of the Geological Society*, vol. 172, no. 6, pp. 822–835, 2015.

[9] Tom A Jordan, Teal R Riley, and Christine S Siddoway, "The geological history and evolution of West Antarctica", *Nature Reviews Earth & Environment*, vol. 1, no. 2, pp. 117–133, 2020.

[10] Michele MC Carafa and Salvatore Barba, "Determining rheology from deformation data: The case of central Italy", *Tectonics*, vol. 30, no. 2, 2011.

[11] ER Ivins, W van der Wal, DA Wiens, AJ Lloyd, and L Caron, "Antarctic upper mantle rheology", *Geological Society, London, Memoirs*, vol. 56, no. 1, pp. M56–2020, 2022.

[12] Magdala Tesauro, Mikhail K Kaban, and Sierd APL Cloetingh, "A new

thermal and rheological model of the European lithosphere”, *Tectonophysics*, vol. 476, no. 3-4, pp. 478–495, 2009.

[13] Joseph Barrell, “The strength of the Earth’s crust part I. Geologic tests of the limits of strength”, *The Journal of Geology*, vol. 22, no. 1, pp. 28–48, 1914.

[14] Xavier Le Pichon, Jean Francheteau, and Jean Bonnin, *Plate tectonics*, vol. 6, Elsevier, 2013.

[15] JA Jackson, “Strength of the continental lithosphere: time to abandon the jelly sandwich?”, *GSA today*, vol. 12, pp. 4–10, 2002.

[16] EB Burov, AB Watts, et al., “The long-term strength of continental lithosphere:” jelly sandwich” or” crème brûlée”?”, *GSA today*, vol. 16, no. 1, pp. 4, 2006.

[17] WF Brace and DL Kohlstedt, “Limits on lithospheric stress imposed by laboratory experiments”, *Journal of Geophysical Research: Solid Earth*, vol. 85, no. B11, pp. 6248–6252, 1980.

[18] S Zhang and SI Karato, “Lattice preferred orientation of olivine in simple shear deformation and the flow geometry of the upper mantle of the Earth”, *Nature*, vol. 375, pp. 774–777, 1995.

[19] Greg Hirth and D Kohlstedf, “Rheology of the upper mantle and the mantle wedge: A view from the experimentalists”, *Geophysical monograph-American Geophysical Union*, vol. 138, pp. 83–106, 2003.

[20] Robert J Twiss, “Theory and applicability of a recrystallized grain size paleopiezometer”, in *Stress in the Earth*, pp. 227–244. Springer, 1977.

[21] Jan Tullis, “Deformation of granitic rocks: experimental studies and natural examples”, *Reviews in Mineralogy and Geochemistry*, vol. 51, no. 1, pp. 51–95, 2002.

[22] Brian Evans, “Creep constitutive laws for rocks with evolving structure”, *Geological Society, London, Special Publications*, vol. 245, no. 1, pp. 329–346, 2005.

[23] Wayne Thatcher, “Nonlinear strain buildup and the earthquake cycle on the San Andreas fault”, *Journal of Geophysical Research: Solid Earth*, vol. 88, no. B7, pp. 5893–5902, 1983.

[24] Peter Bird and Xianghong Kong, “Computer simulations of California tectonics confirm very low strength of major faults”, *Geological Society of America Bulletin*, vol. 106, no. 2, pp. 159–174, 1994.

[25] MR Handy and J-P Brun, “Seismicity, structure and strength of the continental lithosphere”, *Earth and Planetary Science Letters*, vol. 223, no. 3-4, pp. 427–441, 2004.

[26] Wayne Thatcher, “How the continents deform: The evidence from tectonic geodesy”, *Annual Review of Earth and Planetary Sciences*, vol. 37, pp. 237–262, 2009.

[27] Mark D Zoback and John Townend, “Implications of hydrostatic pore

pressures and high crustal strength for the deformation of intraplate lithosphere", *Tectonophysics*, vol. 336, no. 1-4, pp. 19–30, 2001.

[28] Roland Bürgmann and Georg Dresen, "Rheology of the lower crust and upper mantle: Evidence from rock mechanics, geodesy, and field observations", *Annu. Rev. Earth Planet. Sci.*, vol. 36, pp. 531–567, 2008.

[29] Christopher Goetze and Brian Evans, "Stress and temperature in the bending lithosphere as constrained by experimental rock mechanics", *Geophysical Journal International*, vol. 59, no. 3, pp. 463–478, 1979.

[30] Evgene B Burov, "Rheology and strength of the lithosphere", *Marine and petroleum Geology*, vol. 28, no. 8, pp. 1402–1443, 2011.

[31] Peter Bird, "New finite element techniques for modeling deformation histories of continents with stratified temperature-dependent rheology", *Journal of Geophysical Research: Solid Earth*, vol. 94, no. B4, pp. 3967–3990, 1989.

[32] Peter Bird, "Thin-plate and thin-shell finite-element programs for forward dynamic modeling of plate deformation and faulting", *Computers & Geosciences*, vol. 25, no. 4, pp. 383–394, 1999.

[33] Brook Tozer, David T Sandwell, Walter HF Smith, C Olson, JR Beale, and P Wessel, "Global bathymetry and topography at 15 arc sec: SRTM15+", *Earth and Space Science*, vol. 6, no. 10, pp. 1847–1864,

2019.

[34] Tomohisa Okazaki, Yukitoshi Fukahata, and Takuya Nishimura, "Consistent estimation of strain-rate fields from GNSS velocity data using basis function expansion with ABIC", *Earth, Planets and Space*, vol. 73, no. 1, pp. 1–22, 2021.

[35] Corné Kreemer, John Haines, William E Holt, Geoffrey Blewitt, and David Lavallee, "On the determination of a global strain rate model", *Earth, Planets and Space*, vol. 52, no. 10, pp. 765–770, 2000.

[36] E Calais, J-M Nocquet, F Jouanne, and M Tardy, "Current strain regime in the Western Alps from continuous Global Positioning System measurements, 1996–2001", *Geology*, vol. 30, no. 7, pp. 651–654, 2002.

[37] W Spakman and MCJ Nyst, "Inversion of relative motion data for fault slip and continuous deformation in crustal blocks", *Earth Planet. Sci. Lett*, vol. 203, pp. 577–591, 2002.

[38] Ivone Jiménez-Munt, R Sabadini, A Gardi, and G Bianco, "Active deformation in the Mediterranean from Gibraltar to Anatolia inferred from numerical modeling and geodetic and seismological data", *Journal of Geophysical Research: Solid Earth*, vol. 108, no. B1, pp. ETG–2, 2003.

[39] G Pietrantonio and F Riguzzi, "Three-dimensional strain tensor estimation by GPS observations: methodological aspects and geophysical applications", *Journal of Geodynamics*, vol. 38, no. 1, pp. 1–18, 2004.

[40] Richard W Allmendinger, Robert Reilinger, and Jack Loveless, “Strain and rotation rate from GPS in Tibet, Anatolia, and the Altiplano”, *Tectonics*, vol. 26, no. 3, 2007.

[41] Matthias Hackl, Rocco Malservisi, and Shimon Wdowinski, “Strain rate patterns from dense GPS networks”, *Natural Hazards and Earth System Sciences*, vol. 9, no. 4, pp. 1177–1187, 2009.

[42] FC Frank, “Deduction of earth strains from survey data”, *Bulletin of the Seismological Society of America*, vol. 56, no. 1, pp. 35–42, 1966.

[43] WH Prescott and James C Savage, “Strain accumulation on the San Andreas fault near Palmdale, California”, *Journal of Geophysical Research*, vol. 81, no. 26, pp. 4901–4908, 1976.

[44] Kurt L Feigl, Robert W King, and Thomas H Jordan, “Geodetic measurement of tectonic deformation in the Santa Maria fold and thrust belt, California”, *Journal of Geophysical Research: Solid Earth*, vol. 95, no. B3, pp. 2679–2699, 1990.

[45] AJ Haines and WE Holt, “A procedure for obtaining the complete horizontal motions within zones of distributed deformation from the inversion of strain rate data”, *Journal of Geophysical Research: Solid Earth*, vol. 98, no. B7, pp. 12057–12082, 1993.

[46] Corné Kreemer, Geoffrey Blewitt, and Elliot C Klein, “A geodetic plate motion and Global Strain Rate Model”, *Geochemistry, Geophysics,*

Geosystems, vol. 15, no. 10, pp. 3849–3889, 2014.

[47] David T Sandwell and Paul Wessel, “Interpolation of 2-D vector data using constraints from elasticity”, *Geophysical Research Letters*, vol. 43, no. 20, pp. 10–703, 2016.

[48] Giordano Teza, Arianna Pesci, and Marco Meschis, “A MATLAB toolbox for computation of velocity and strain rate field from GNSS coordinate time series”, *Annals of Geophysics*, 2023.

[49] Zheng-Kang Shen, David D Jackson, and Bob X Ge, “Crustal deformation across and beyond the Los Angeles basin from geodetic measurements”, *Journal of Geophysical Research: Solid Earth*, vol. 101, no. B12, pp. 27957–27980, 1996.

[50] Zheng-Kang Shen, Min Wang, Yuehua Zeng, and Fan Wang, “Optimal interpolation of spatially discretized geodetic data”, *Bulletin of the Seismological Society of America*, vol. 105, no. 4, pp. 2117–2127, 2015.

[51] Takeshi Sagiya, Shin’ichi Miyazaki, and Takashi Tada, “Continuous GPS array and present-day crustal deformation of Japan”, *Pure and applied Geophysics*, vol. 157, no. 11, pp. 2303–2322, 2000.

[52] Daniel Stich, Enrico Serpelloni, Flor de Lis Mancilla, and Jose Morales, “Kinematics of the Iberia–Maghreb plate contact from seismic moment tensors and GPS observations”, *Tectonophysics*, vol. 426, no. 3-4, pp. 295–317, 2006.

[53] Roberto Devoti, Alessandra Esposito, Grazia Pietrantonio, Anna Rita Pisani, and Federica Riguzzi, “Evidence of large scale deformation patterns from GPS data in the Italian subduction boundary”, *Earth and Planetary Science Letters*, vol. 311, no. 3-4, pp. 230–241, 2011.

[54] Konstantinos Chousianitis, Athanassios Ganas, and Christos P Evangelidis, “Strain and rotation rate patterns of mainland Greece from continuous GPS data and comparison between seismic and geodetic moment release”, *Journal of Geophysical Research: Solid Earth*, vol. 120, no. 5, pp. 3909–3931, 2015.

[55] Philip England and Peter Molnar, “Active deformation of Asia: From kinematics to dynamics”, *Science*, vol. 278, no. 5338, pp. 647–650, 1997.

[56] Federica Riguzzi, Mattia Crespi, Roberto Devoti, Carlo Doglioni, Grazia Pietrantonio, and Anna Rita Pisani, “Geodetic strain rate and earthquake size: New clues for seismic hazard studies”, *Physics of the Earth and Planetary Interiors*, vol. 206, pp. 67–75, 2012.

[57] Mimmo Palano, “On the present-day crustal stress, strain-rate fields and mantle anisotropy pattern of Italy”, *Geophysical Journal International*, vol. 200, no. 2, pp. 969–985, 2015.

[58] Steven N Ward, “A multidisciplinary approach to seismic hazard in southern California”, *Bulletin of the Seismological Society of America*, vol. 84, no. 5, pp. 1293–1309, 1994.

[59] CD Reddy, Gamal El-Fiky, Teruyuki Kato, Seiichi Shimada, and K Vijay Kumar, “Crustal strain field in the Deccan trap region, western India, derived from GPS measurements”, *Earth, planets and space*, vol. 52, no. 11, pp. 965–969, 2000.

[60] Layue Li, Yanqiang Wu, Yujiang Li, Wei Zhan, and Xinzhong Liu, “Dynamic deformation and fault locking of the Xianshuihe Fault Zone, Southeastern Tibetan Plateau: implications for seismic hazards”, *Earth, Planets and Space*, vol. 74, no. 1, pp. 1–16, 2022.

[61] MM Arcila and Alfonso Muñoz Martín, “Integrated perspective of the present–day stress and strain regime in Colombia from analysis of earthquake focal mechanisms and geodetic data”, *The Geology of Colombia*, vol. 4, 2020.

[62] Augustus Edward Hough Love, *A treatise on the mathematical theory of elasticity*, Cambridge university press, 2013.

[63] SV Ashurkov, VA San’Kov, MA Serov, P Yu Luk’yanov, NN Grib, GS Bordonskii, and MG Dembelov, “Evaluation of present-day deformations in the Amurian Plate and its surroundings, based on GPS data”, *Russian Geology and Geophysics*, vol. 57, no. 11, pp. 1626–1634, 2016.

[64] J Alejandro González-Ortega, J Javier González-García, and David T Sandwell, “Interseismic velocity field and seismic moment release in northern Baja California, Mexico”, *Seismological Research Letters*, vol. 89, no. 2A, pp. 526–533, 2018.

[65] Xiaoning Su, Lianbi Yao, Weiwei Wu, Guojie Meng, Lina Su, Renwei Xiong, and Shunying Hong, "Crustal deformation on the northeastern margin of the Tibetan plateau from continuous GPS observations", *Remote sensing*, vol. 11, no. 1, pp. 34, 2018.

[66] DT Griggs, FJ Turner, and HC Heard, "Deformation of Rocks at 500 to 800· c., in Rock Deformation", *Geol Soc. Am. Mem*, vol. 79, pp. 39–104, 1960.

[67] Shao Xian Zang, Rong Qiang Wei, and Jie Yuan Ning, "Effect of brittle fracture on the rheological structure of the lithosphere and its application in the Ordos", *Tectonophysics*, vol. 429, no. 3-4, pp. 267–285, 2007.

[68] Mareen Lösing, Jörg Ebbing, and Wolfgang Szwillus, "Geothermal heat flux in Antarctica: Assessing models and observations by Bayesian inversion", *Frontiers in Earth Science*, vol. 8, pp. 105, 2020.

[69] Geoffrey Blewitt and David Lavallée, "Effect of annual signals on geodetic velocity", *Journal of Geophysical Research: Solid Earth*, vol. 107, no. B7, pp. ETG–9, 2002.

[70] Corné Kreemer, William C Hammond, and Geoffrey Blewitt, "A robust estimation of the 3-D intraplate deformation of the North American plate from GPS", *Journal of Geophysical Research: Solid Earth*, vol. 123, no. 5, pp. 4388–4412, 2018.

[71] Corné Kreemer and Geoffrey Blewitt, "Robust estimation of spatially

varying common-mode components in GPS time-series", *Journal of geodesy*, vol. 95, no. 1, pp. 1–19, 2021.

[72] Alexandre Michel, Alvaro Santamaría-Gómez, Jean-Paul Boy, Félix Perosanz, and Sylvain Loyer, "Analysis of GNSS Displacements in Europe and Their Comparison with Hydrological Loading Models", *Remote Sensing*, vol. 13, no. 22, pp. 4523, 2021.

[73] Geoffrey Blewitt, Corné Kreemer, William C Hammond, and Julien Gazeaux, "MIDAS robust trend estimator for accurate GPS station velocities without step detection", *Journal of Geophysical Research: Solid Earth*, vol. 121, no. 3, pp. 2054–2068, 2016.

[74] Henri Theil, "A rank-invariant method of linear and polynomial regression analysis", *Indagationes mathematicae*, vol. 12, no. 85, pp. 173, 1950.

[75] Pranab Kumar Sen, "Estimates of the regression coefficient based on Kendall's tau", *Journal of the American statistical association*, vol. 63, no. 324, pp. 1379–1389, 1968.

[76] William C Hammond, Geoffrey Blewitt, and Corné Kreemer, "GPS imaging of vertical land motion in California and Nevada: Implications for Sierra Nevada uplift", *Journal of Geophysical Research: Solid Earth*, vol. 121, no. 10, pp. 7681–7703, 2016.

[77] Corné Kreemer and Ilya Zaliapin, "Spatiotemporal correlation between

seasonal variations in seismicity and horizontal dilatational strain in California", *Geophysical Research Letters*, vol. 45, no. 18, pp. 9559–9568, 2018.

[78] L Caron, ER Ivins, E Larour, S Adhikari, J Nilsson, and G Blewitt, "GIA model statistics for GRACE hydrology, cryosphere, and ocean science", *Geophysical Research Letters*, vol. 45, no. 5, pp. 2203–2212, 2018.

[79] Chen Yu, Zhenhong Li, Nigel T Penna, and Paola Crippa, "Generic atmospheric correction model for interferometric synthetic aperture radar observations", *Journal of Geophysical Research: Solid Earth*, vol. 123, no. 10, pp. 9202–9222, 2018.

[80] Adebayo Oluwaseun Ojo, Honn Kao, Yan Jiang, Michael Craymer, and Joseph Henton, "Strain Accumulation and Release Rate in Canada: Implications for Long-Term Crustal Deformation and Earthquake Hazards", *Journal of Geophysical Research: Solid Earth*, vol. 126, no. 4, pp. e2020JB020529, 2021.

[81] Sierd Cloetingh and Evgene B Burov, "Thermomechanical structure of European continental lithosphere: constraints from rheological profiles and EET estimates", *Geophysical Journal International*, vol. 124, no. 3, pp. 695–723, 1996.

[82] SAPL Cloetingh, PA Ziegler, F Beekman, PAM Andriessen, N Hardebol, and P Dezes, "Intraplate deformation and 3D rheological structure of the Rhine Rift System and adjacent areas of the northern Alpine foreland",

International Journal of Earth Sciences, vol. 94, no. 4, pp. 758–778, 2005.

[83] Lanbo Liu and Mark D Zoback, “Lithospheric strength and intraplate seismicity in the New Madrid seismic zone”, *Tectonics*, vol. 16, no. 4, pp. 585–595, 1997.

[84] Alexey Baranov, Robert Tenzer, and Mohammad Bagherbandi, “Combined gravimetric–seismic crustal model for Antarctica”, *Surveys in geophysics*, vol. 39, no. 1, pp. 23–56, 2018.

[85] Meijian An, Douglas A Wiens, Yue Zhao, Mei Feng, Andrew Nyblade, Masaki Kanao, Yuansheng Li, Alessia Maggi, and Jean-Jacques Lévêque, “Temperature, lithosphere-asthenosphere boundary, and heat flux beneath the Antarctic Plate inferred from seismic velocities”, *Journal of Geophysical Research: Solid Earth*, vol. 120, no. 12, pp. 8720–8742, 2015.

[86] Alex Burton-Johnson, JA Halpin, Joanne M Whittaker, Felicity S Graham, and Sally Joan Watson, “A new heat flux model for the Antarctic Peninsula incorporating spatially variable upper crustal radiogenic heat production”, *Geophysical Research Letters*, vol. 44, no. 11, pp. 5436–5446, 2017.

[87] John W Goodge, “Crustal heat production and estimate of terrestrial heat flow in central East Antarctica, with implications for thermal input to the East Antarctic ice sheet”, *The Cryosphere*, vol. 12, no. 2, pp. 491–504, 2018.

[88] Cathrine Fox Maule, Michael E Purucker, Nils Olsen, and Klaus Mosegaard, "Heat flux anomalies in Antarctica revealed by satellite magnetic data", *Science*, vol. 309, no. 5733, pp. 464–467, 2005.

[89] JW Van Wijk, JF Lawrence, and NW Driscoll, "Formation of the Transantarctic Mountains related to extension of the West Antarctic Rift system", *Tectonophysics*, vol. 458, no. 1-4, pp. 117–126, 2008.

[90] Ricarda Dziadek, Karsten Gohl, Norbert Kaul, et al., "Elevated geothermal surface heat flow in the Amundsen Sea Embayment, West Antarctica", *Earth and Planetary Science Letters*, vol. 506, pp. 530–539, 2019.

[91] JP O'Donnell, GW Stuart, AM Brisbourne, K Selway, Y Yang, GA Nield, PL Whitehouse, AA Nyblade, DA Wiens, RC Aster, et al., "The uppermost mantle seismic velocity structure of West Antarctica from Rayleigh wave tomography: Insights into tectonic structure and geothermal heat flow", *Earth and Planetary Science Letters*, vol. 522, pp. 219–233, 2019.

[92] D Hasterok and DS Chapman, "Heat production and geotherms for the continental lithosphere", *Earth and Planetary Science Letters*, vol. 307, no. 1-2, pp. 59–70, 2011.

[93] Kevin P Furlong and David S Chapman, "Heat flow, heat generation, and the thermal state of the lithosphere", *Annual Review of Earth and Planetary Sciences*, vol. 41, pp. 385–410, 2013.

[94] Susan Ellis and Kelin Wang, “Lithospheric strength and stress revisited: Pruning the Christmas tree”, *Earth and Planetary Science Letters*, vol. 595, pp. 117771, 2022.

[95] Anthony Brian Watts, *Isostasy and Flexure of the Lithosphere*, Cambridge University Press, 2001.

[96] Giorgio Ranalli, “Rheology of the crust and its role in tectonic reactivation”, *Journal of geodynamics*, vol. 30, no. 1-2, pp. 3–15, 2000.

[97] Juan Carlos Afonso and Giorgio Ranalli, “Crustal and mantle strengths in continental lithosphere: is the jelly sandwich model obsolete?”, *Tectonophysics*, vol. 394, no. 3-4, pp. 221–232, 2004.

[98] JL Davis, RA Bennett, and BP Wernicke, “Assessment of GPS velocity accuracy for the Basin and Range Geodetic Network (BARGEN)”, *Geophysical Research Letters*, vol. 30, no. 7, 2003.

[99] G Buble, RA Bennett, and S Hreinsdóttir, “Tide gauge and GPS measurements of crustal motion and sea level rise along the eastern margin of Adria”, *Journal of Geophysical Research: Solid Earth*, vol. 115, no. B2, 2010.

[100] Paul Wessel and Walter HF Smith, “New, improved version of Generic Mapping Tools released”, *Eos, Transactions American Geophysical Union*, vol. 79, no. 47, pp. 579–579, 1998.

[101] Marie-Noëlle Bouin and Christophe Vigny, “New constraints on Antarc-

tic plate motion and deformation from GPS data", *Journal of Geophysical Research: Solid Earth*, vol. 105, no. B12, pp. 28279–28293, 2000.

[102] Trond H Torsvik, R Dietmar Müller, Rob Van der Voo, Bernhard Steinberger, and Carmen Gaina, "Global plate motion frames: toward a unified model", *Reviews of geophysics*, vol. 46, no. 3, 2008.

[103] Martine Amalvict, Pascal Willis, Guy Wöppelmann, Erik R Ivins, Marie-Noëlle Bouin, Laurent Testut, and Jacques Hinderer, "Isostatic stability of the East Antarctic station Dumont d'Urville from long-term geodetic observations and geophysical models", *Polar Research*, vol. 28, no. 2, pp. 193–202, 2009.

[104] Michael Bevis, Eric Kendrick, Robert Smalley Jr, Ian Dalziel, Dana Caccamise, Ingo Sasgen, Michiel Helsen, FW Taylor, Hao Zhou, Abel Brown, et al., "Geodetic measurements of vertical crustal velocity in West Antarctica and the implications for ice mass balance", *Geochemistry, Geophysics, Geosystems*, vol. 10, no. 10, 2009.

[105] Ian D Thomas, Matt A King, Michael J Bentley, Pippa L Whitehouse, Nigel T Penna, Simon DP Williams, Riccardo EM Riva, David A Lavallee, Peter J Clarke, Edward C King, et al., "Widespread low rates of Antarctic glacial isostatic adjustment revealed by GPS observations", *Geophysical Research Letters*, vol. 38, no. 22, 2011.

[106] Donald F Argus, WR Peltier, R Drummond, and Angelyn W Moore, "The Antarctica component of postglacial rebound model ICE-6G_C

(VM5a) based on GPS positioning, exposure age dating of ice thicknesses, and relative sea level histories", *Geophysical Journal International*, vol. 198, no. 1, pp. 537–563, 2014.

[107] ANTONIO Zanutta, MONIA Negusini, LUCA Vittuari, P Cianfarra, F Salvini, F Mancini, P Sterzai, M Dubbini, A Galeandro, and A Capra, "Monitoring geodynamic activity in the Victoria Land, East Antarctica: Evidence from GNSS measurements", *Journal of Geodynamics*, vol. 110, pp. 31–42, 2017.

[108] Grace A Nield, Valentina R Barletta, Andrea Bordoni, Matt A King, Pippa L Whitehouse, Peter J Clarke, Eugene Domack, Ted A Scambos, and Etienne Berthier, "Rapid bedrock uplift in the Antarctic Peninsula explained by viscoelastic response to recent ice unloading", *Earth and Planetary Science Letters*, vol. 397, pp. 32–41, 2014.

[109] Stephen H Kirby, William B Durham, and Laura A Stern, "Mantle phase changes and deep-earthquake faulting in subducting lithosphere", *Science*, vol. 252, no. 5003, pp. 216–225, 1991.

[110] SH Kirby, S Stein, EA Okal, and D Rubie, "Deep earthquakes and metastable mantle phase transformations in subducting oceanic lithosphere", *Rev. Geophys. Space Phys*, vol. 34, pp. 261–306, 1996.

[111] Evgene B Burov and Michel Diament, "The effective elastic thickness (T_e) of continental lithosphere: What does it really mean?", *Journal of Geophysical Research: Solid Earth*, vol. 100, no. B3, pp. 3905–3927,

1995.

[112] Giorgio Ranalli and Donald C Murphy, “Rheological stratification of the lithosphere”, *Tectonophysics*, vol. 132, no. 4, pp. 281–295, 1987.

Chapter 5

FINAL REMARKS AND FUTURE PERSPECTIVES

GIA modelling is an evolving subject and represent a tool for gaining insight into the properties of the Earth's interior. In this thesis I addressed a previously suggested modeling approach to properly handle the sea level problem due to GIA in the Mediterranea area. The information provided here is not exclusive, and the reader is referred to the extensive reference list if further insight is require. From the work presented in Chapter 3 it was find that, by comparing vertical velocities provided by our GIA model with observed rates at GNSS sites, GIA effects are a marginal contribution to geodetic velocity only at sites where the largest subsidence is recorded, while at the majority of GNSS sites, GIA may represent a significant contribution to observed rates and shall be taken into account for a correct interpretation of the velocity field. Therefore, for an accurate GIA modeling, the isostatic response to the melting of the Alpine Würm ice sheet essential to take into account. In fact, If we take into account the contributions from both global and regional GIA, our model predicts a widespread sea-level fall in the northern Adriatic, with rates decreasing southward. At the same time, an uplift field with vertical velocities on the northern margin of the basin, which decrease southward reaching the zero level at Ancona.

Chapter 4 demonstrates that the strength of the lithosphere can vary drastically within a few kilometers, changing from a strong crust and a weak mantle to weak crust and a relatively strong mantle (as discuss in Section 4.5.4). The approach used in this work has allowed us to analyze the strength of the lithosphere beneath the Graham Land region (Antarctic Peninsula). Data indicates clearly highlights a diffuse state of uplift (positive vertical velocity) throughout the study area. At the ame time, the deformation model highlight the surface geodynamics of the Graham Land where two distinct kinematic patterns can be clearly seen, going from being relatively stable with very small (insignificant) deformation to an increasing W-E oriented deformation.

Several avenues could be explored to further exploit and enhance the advances described in this thesis work. In particular, new knowledge of the post-LGM evolution of the ice sheets has benefited from the rapid development of an extended GPS observation network and of an increase in suitable geological data of ice sheet retreat. Furthermore, increasingly advanced knowledge of the crustal and upper mantle rheological structure will lead to better understanding the geological processes but also to better constrain geophysical processes such as that of the GIA. Given the enormous amount of data available in the Alpine area, this study could be used in the future as a starting point to test different deglaciation histories and different basal conditions (YSE).

Finally, as sea level changes are one of the most striking manifestations of past and present climate change, it is crucial to develop our understanding of the processes that influence its characteristics. Their breadth is very extensive, and includes processes that control the growth and disappearance of large continental ice sheet cover and the feedbacks that relate these components but it also passes through knowledge of the Earth's interior, of its orbital properties and of the evolution of its gravitational field. In the context of understanding the present and future climate perturbations induced by anthropogenic emissions of greenhouse gases, it is important, more than ever, to understand correctly how the past climate responded to various forcings in order to correctly capture the potential physical and societal impacts brought by current climate change especially in those areas highly at risk such as the Venice lagoon

Appendix A

YSE - YIELD STRENGTH ENVELOPE code

```
%###############################################################
%###          YSE - YIELD STRENGTH ENVELOPE                  ###
%###                                                         ###
%###           Created by FERNANDO LINSALATA (2023)          ###
%###      Contact:                                           ###
%###           f.linsalata91@gmail.com                       ###
%###           fernando.linsalata2@unibo.it                  ###
%###                                                         ###
%### --------------------------------------------------------###
%###     First implemented by Peter Bird et al. (1989)       ###
%### --------------------------------------------------------###
%
clear all;
clc;
%
z = [0:1000:100000]';       % Depth                --> meters
z_inc = 1000;               % Increment in deth    --> meters
crust = 33000;              % Bottom of the crust  --> meters
trans = 34000;              % Transition zone      --> meters
```

```
mantle = 100000;            % Mantle               --> meters
H_c = 0.000000178;          % RHP  crust  [uW/m^3] --> W/m^3
H_m = 0;                    % RHP  mantle [uW/m^3] --> W/m^3
q = 0.055;                  % GHF         [mW/m^2] --> W/m^2
T = 273;                    % Temperature          --> K
k_c = 2.5;                  % Tconductivity crust  --> W/mK
k_m = 3.5;                  % Tconductivity mantle --> W/mK
rho_c = 2889;               % Density crust        --> kg/m^3
rho_m = 3332;               % Density mantle       --> kg/m^3
g = 9.81;                   % Gravit_accel         --> m/s^2
beta_c = 4000;              % Tcoeff creep rheology crust
beta_m = 18314;             % Tcoeff creep rheology mantle
Xi_c = 0;                   % Depth coeff in creep rheology
.
.
.
%
%-------------------------------------------
% Heat flow density as a function of depth
%-------------------------------------------
for i = 1:1:100
  if z(1+i,1) <= crust
         z(1+i,2) = z(i,2) - q_top;
  elseif z(1+i,1) == trans
         z(1+i,2) = z(i,2) - q_trans;
  elseif z(1+i,1) > trans
         z(1+i,2) = z(i,2) - q_bottn;
  end
```

```
end
.
.
.
%
%--------------------------------------------
% Surface Temperature as a function
% of depth and Heat flow density
%--------------------------------------------
for j = 1:1:100
  if z(1+j,1) <= crust
        z(1+j,3) = z(j,3)+0.5*(z(j,2)+z(j+1,2))*(z_inc/t_top);
  elseif z(1+j,1) == trans
        z(1+j,3) = z(j,3)+0.5*(z(j,2)+z(j+1,2))*(z_inc/t_trans);
  elseif z(1+j,1) > trans
        z(1+j,3) = z(j,3)+0.5*(z(j,2)+z(j+1,2))*(z_inc/t_bottn);
  end
end
%
z(:,4) = z(:,3) - T;   % new column for suface temperature in C
%
.
.
.
%-----------------------------------
% in plate??  0 = TRUE, 1 = FASLE
%-----------------------------------
for o = 0:1:100
```

```
    if z(1+o,1) <= (crust+mantle)
        z(1+o,11) = 0;
    else
        z(1+o,11) = 1;
    end
end
%
.
.
.
%
plot(z(:,12),z(:,1))
grid on
axis ij
%
%##################  END ########################
```

Listing A.1. Part of Matlab code.

Appendix B

Publications related to this thesis

B.1 Regular Papers

1. F. **LINSALATA**, D. MELINI and G. SPADA, "*Glacial Isostatic Adjustment in the Northern Adriatic region: estimates of the contribution from the Alpine ice sheet*", Geophysical Journal International, Volume 233, Issue 3, June 2023, Pages 2039–2052.

   DOI: `https://doi.org/10.1093/gji/ggad026`

2. F. **LINSALATA**, D. MELINI and G. SPADA, "*Strength of the lithosphere derived by geological and geophysics data: the Graham Land (Antarctic Peninsula) case study*", (2024) in prep.

B.2 Presentations in National/International Conferences

- **ORAL PRESENTATIONS**

1. F. **LINSALATA**, D. MELINI and G. SPADA, "*Ongoing sea-level rise and vertical land movements in the Venetian Lagoon: the contribution of Glacial Isostatic Adjustment*", **XCI Congresso della SGI** (Società Geologica Italiana), Sessione: S9 - Ground deformation measurements and Geosciences: applications and outlooks - Torino, ITALY, September 2022

2. F. **LINSALATA**, D. MELINI and G. SPADA, "*New estimates of the contribution of Glacial Isostatic Adjustment to sea-level variations and vertical land movements in the Northern Adriatic Sea and in the Venetian Lagoon*", **41° National Conference GNGTS** (Gruppo Nazionale di Geofisica della Terra solida), Session: S1.3 - Physical models for the Solid Earth and integration between modeling and data of different nature - Bologna, ITALY, February 2023.

3. F. **LINSALATA**, D. MELINI and G. SPADA, "*Strength of the lithosphere derived by geological and geophysics data: the Graham Land (Antarctic Peninsula) case study*", **42° National Conference GNGTS** (Gruppo Nazionale di Geofisica della Terra solida), Session: S1.3 - Physical models for the Solid Earth and integration between modeling and data of different nature - Ferrara, ITALY, February 2024.

- **POSTER PRESENTATIONS**

4. F. **LINSALATA** and G. SPADA, "*Strength of the lithosphere derived by geological and geophysics data: the Graham Land (Antarctic Peninsula) case study*", Session: T1.3 - The crustal stress state and strength: Conceptions, modelling, and uncertainties - **EGU23**, European Geosciences Union, General Assembly 2023, Vienna, AUSTRIA, April 2023.

List of Figures

1.1 Global ice and paleo-topography at LGM 5
1.2 PGR draft 7
1.3 GIA fingerprint 9
1.4 Effects near/far-field 14
1.5 Würm 16
1.6 Eustatic-Curves 18
1.7 Orbital parameter 21

2.1 Maxwell's time scale 44
2.2 Radial viscosity structure 46
2.3 Maxwell model 47
2.4 Sketches of the Earth's components 54
2.5 1D GIA model 63

3.1 Overview of the Venetian Lagoon 80
3.2 Location of PSMSL tide gauges in the Venetian Lagoon 81
3.3 Sea-level change trends 84

3.4 Vertical velocities in the Venetian Lagoon and associated uncertainties 88

3.5 Length of the time series 89

3.6 GNSS processing list 1 90

3.7 GNSS processing list 2 91

3.8 GNSS processing list 3 92

3.9 GNSS processing list 4 95

3.10 Alpine ice thickness and extents 100

3.11 Present-day sea-level change $\dot{S}$ 101

3.12 GIA fingerprints $\dot{S}$ and $\dot{U}$ in the Northern Adriatic 104

3.13 GIA fingerprints $\dot{N}$in the Northern Adriatic 109

4.1 Overview of the Graham Land, Antarctic Peninsula 135

4.2 Location of the 21 GNSS for Graham Land 144

4.3 GNSS daily time series in the Antarctic Peninsula (east-component) 147

4.4 GNSS daily time series in the Antarctic Peninsula (north-component) 148

4.5 GNSS daily time series in the Antarctic Peninsula (up-component) 149

4.6 Moho depth in the Antarctic Peninsula 151

4.7 MATLAB workflow 153

4.8 Vertical velocities and associated uncertainties of 21 GNSS in Antarctic Peninsula 157

4.9 Absolute horizontal velocity vectors in Antarctic Peninsula . . 159

4.10 Horizontal strain-rates and second invariant 162

4.11 Yield strength envelop (YSE) 165

List of Tables

3.1 Vertical velocities estimated with the MIDAS algorithm at the 45 GNSS sites considered in this study and corresponding modeled vertical velocities according to the combined effect of the ICE-7G_NA (VM7) and iALP models. 93

3.2 Vertical velocities estimated with the MIDAS algorithm at the 45 GNSS sites considered in this study and corresponding modeled vertical velocities according to the combined effect of the ICE-7G_NA (VM7) and iALP models. 94

4.1 GNSS velocities estimated with the MIDAS algorithm at the 21 sites considered in this study and associated uncertainties. Velocities are in the Antarctic Plate reference frame. 145

4.2 GNSS velocities estimated with the MIDAS algorithm at the 21 sites considered in this study and associated uncertainties. Velocities are in the Antarctic Plate reference frame. 146

4.3 Rheological model parameters used in our simulations. Mantle values are given in parentheses. For parameters that have been set differently in the three considered profiles, the symbols (A), (B) and (C) correspond to the values assumed in each region. 154